Matheus Lopes Peres

Integrating artificial neural networks and Green's function approach for geomechanics application

Tese de Doutorado

Thesis presented to the Programa de Pós-graduação em Engenharia Civil of PUC-Rio in partial fulfillment of the requirements for the degree of Doutor em Ciências – Engenharia Civil

Advisor: Prof. Elisa Dominguez Sotelino

Rio de Janeiro
April 2023

Matheus Lopes Peres

Integrating artificial neural networks and Green's function approach for geomechanics application

Thesis presented to the Programa de Pós-graduação em Engenharia Civil of PUC-Rio in partial fulfillment of the requirements for the degree of Doutor em Ciências – Engenharia Civil. Approved by the examination Committee.

Prof. Elisa Dominguez Sotelino
Advisor
Department of Civil and Environmental Engineering – PUC-Rio

Prof. Luiz Fernando Campos Ramos Martha
Department of Civil and Environmental Engineering – PUC-Rio

Prof. Eurípedes do Amaral Vargas Junior
Department of Civil and Environmental Engineering – PUC-Rio

Prof. Frederic Gerard Christian Valentin
LNCC

Prof. Maria Cascão Ferreira de Almeida
ESCOLA POLITÉCNICA

Rio de Janeiro, April   5th, 2023.

Matheus Lopes Peres

Undergraduate in Civil Engineering at Federal University of Sergipe (UFS) in 2017. M.Sc. Degree in Civil Engineering at Pontifical Catholic University of Rio de Janeiro (PUC-Rio) in 2019.

I dedicate this thesis to all who
believe in education and science as a
tool for social development.

Acknowledgments

Firstly, I would like to thank god for the health and the gift of life.

I also would like to thank my parents Aparecida and Péricles to always encourage and support, not only during this research work but during all life. My fiancée, Eryane, who was my main companion during covid-19 pandemic, you were fundamental for this achievement. I also can't forget the rest of my family, who, even from distance, always cheer for me.

This research work would not be possible without the guidance of Professor Elisa Sotelino, example of educator, researcher, and engineer, I will always be grateful. Leonardo Mesquita, my doctoral colleague, your partnership, and discussions about computational mechanics were fundamental to the results of this research work. I also would like to thank Yves Leroy for receiving me in Pau and introducing me to reservoir geomechanics, and my colleagues from PUC-Rio and Minhocão for fun time.

I also can't forget the Petrobras colleagues, Diogo Rossi, Vitor Mello, and Ricardo Amaral, and the professors Eurípedes Vargas, Luiz Fernando Martha, Frederic Valentin, and Maria Cascão for technical contribution to this research work.

Abstract

Peres, Matheus Lopes; Sotelino, Elisa Dominguez (Advisor). **Integrating artificial neural networks and Green's function approach for geomechanics application**. Rio de Janeiro, 2023. 135 p. Doctoral thesis - Department do Civil and Environmental Engineering, Pontifical Catholic University of Rio de Janeiro.

The analysis and simulation of problems associated with reservoir geomechanics are traditionally performed using the finite element method. However, to perform this analysis, it is necessary to consider a region much larger than the region in which the reservoir is inserted. This is done so that boundary conditions can be applied in an attempt to mimic the effect of the infinite media surrounding the reservoir. With the aim of reducing the need for discretization of large regions of the massif, a Green's functions approach was proposed for reservoir geomechanical analysis. This method is based on the use of classical analytical solutions (Kelvin's fundamental solution, Melan's fundamental solution, for example) as auxiliary solutions to solve elastically heterogeneous and nonlinear problems in fluid-saturated media. The non-linearity of the material can be due to irreversible deformations or non-linear elasticity response typical of 4D analysis. The general solution procedure relies on a discrete collocation method and an iterative fixed-point approach to build the displacement field. This method's convergence was verified through simplified models that have analytical solutions. As the reduction in processing time is crucial for decision-makers to act in field applications, two improvements were proposed using artificial intelligence (AI) to reduce processing time of the Green's function approach. The first improvement is based on the generalization ability of artificial neural networks (ANN). Due to this characteristic, it was proposed to discretize the model with a coarse mesh of intelligent elements instead of refined mesh of traditional elements based on polynomials. The behavior of the strain field within these new elements is predicted using an ANN. To make these predictions, the neural network uses displacement boundary conditions, material properties and the geometric shape of the element as input data. The examples comparing the intelligent element approach and the traditional method were performed on a computer with 12 threads of 2,6GHz and

32GB RAM. This comparison showed reductions between five and ten times in CPU time, while maintaining the accuracy of the results. The second improvement consists in the use of auxiliary solutions that consider the heterogeneity of stratified massifs. These solutions are obtained through the training of artificial neural networks that have as output the displacement in a certain point of the stratified massif due to the application of a point load inside the massif. This ANN uses as input data elastic properties and the thickness of each layer of the massif, and of the semi-infinite media, as well as the coordinates of the point load and of the point where the displacement is to be evaluated. The use of the developed ANN-based Green's function approach only demands the discretization of the reservoir itself, thus avoiding the discretization of other regions of the massif. Furthermore, it is possible to obtain the displacement at any point of the massif due to a pore pressure variation within the reservoir without having to solve for the other points in the massif. These two characteristics increase the efficient of the method in relation to traditional methods, such as the finite element method. A numerical example was performed on a computer with 12 threads of 2,6GHz and 32GB RAM to compare the ANN-based Green's function approach with the traditional approach. The CPU time to obtain the solution using the ANN-based Green's function approach was five times smaller than the that required by the traditional approach.

Keywords

Geomechanics; Computational mechanics; Green's function; artificial intelligence; neural network.

Resumo

Peres, Matheus Lopes; Sotelino, Elisa Dominguez (Orientador). **Integração de redes neurais artificiais a métodos numéricos baseados em funções de Green para aplicações em geomecânica**. Rio de Janeiro, 2023. 135 p. Tese de Doutorado – Departamento de Engenharia Civil e Ambiental, Pontifícia Universidade Católica do Rio de Janeiro.

A modelagem de problemas relacionados a geomecânica do reservatório é tradicionalmente realizada por elementos finitos. Para utilizar esse método é preciso que o modelo englobe uma região consideravelmente superior a região em que o reservatório está inserido, além de necessitar imposição condições de contorno. Pensando em reduzir a necessidade de discretização de grandes regiões do maciço rochoso é proposto o método das funções de Green para análise geomecânica. Este método é baseado no uso de soluções analíticas clássicas (solução fundamental de Kelvin, solução fundamental de Melan, por exemplo) como soluções auxiliares para resolver problemas elasticamente heterogêneo e não lineares em meios saturados de fluidos. A não linearidade do material pode ser devido a deformações irreversíveis ou resposta de elasticidade não linear típica da análise 4D. O procedimento de solução geral depende de um método de colocação discreta e uma abordagem iterativa de ponto fixo para construir o campo de deslocamento. Esse método teve sua convergência verificada através de modelos simplificados que possuem solução analítica. Visando o avanço do desempenho computacional do método das funções de Green, foram feitas duas modificações independentes utilizando inteligência artificial. A primeira modificação é baseada na integração de dois conceitos principais: o teorema da reciprocidade e a capacidade de generalização das redes neurais artificiais. O teorema da reciprocidade é usado para formular a expressão matemática que rege o problema geomecânico, que é então discretizado no espaço em elementos inteligentes. O comportamento do campo de deformação dentro desses novos elementos é previsto usando uma rede neural artificial. Para fazer essas previsões, a rede neural usa condições de contorno de deslocamento, propriedades do material e a forma geométrica do elemento como dados de entrada. A segunda modificação consiste na utilização de soluções auxiliares que considerem a heterogeneidade de maciços estratificados. Essas

soluções são obtidas através do treinamento de redes neurais artificiais que tem como dado de saída o deslocamento em um determinado ponto do maciço estratificado devido a aplicação de uma força pontual em um ponto no interior desse maciço. Para isso, as redes neurais de deslocamentos necessitam das propriedades elásticas e da espessura de cada camada do maciço bem como das coordenadas de aplicação da força pontual e do ponto onde será avaliado o deslocamento. Ao se utilizar essas soluções fundamentais baseadas em inteligência artificial é possível se obter todo o campo de deslocamentos de um problema heterogêneo e elástico de geomecânica do reservatório bastando apenas discretizar o reservatório. Cada uma das modificações do método da função de Green foi avaliada individualmente e observou-se um ganho de pelo menos 5 vezes no tempo de processo, utilizando o mesmo recurso computacional, quando se compara ao método clássico da função de Green.

Palavras-chave

Geomecânica; Mecânica computacional; Funções de Green; Inteligência artificial; Rede neural.

Summary

List of figures

List of tables

List of abbreviations and symbols

ANN	artificial neural network
FEM	finite element model
Ω_R	reservoir subdomain
Ω_t	problem domain
$\Delta\sigma_{ij}$	variation of the stress state
Δp	change in pore pressure
f_i	external field generated by body or surface forces
ε_{ij}	second-order strain tensor
u_i	displacement vector
$\mathbb{C}^e_{ijkl}$	fourth-order stiffness tensor
A_{ij}	second-order Biot tensor
$\Delta\bar\sigma_{ij}$	additional second-order stress tensor
$\hat u_i$	virtual displacement vector
$\hat\varepsilon_{ij}$	virtual strain tensor
ΔT_i	variation of surfaces forces
$u_k(X_i)$	horizontal or vertical displacement in the position X_i
α	Biot coefficient
δ_{ij}	Kronecker delta
ε^*_{mnk}	strains in the x_i position obtained from the fundamental solution
N_{Ω_R}	number of triangular regions in Ω_R subdomain
N_{Ω_t}	number of triangular regions in Ω_t domain
Θ_β	volumetric strain variation
R	internal radius (reservoir)
K_R	reservoir bulk modulus (core)
G_R	reservoir shear modulus (core)
C	external radius (cap rock)
K_C	cap rock bulk modulus
G_C	cap rock shear modulus
K_∞	bulk modulus of the infinite space
G_∞	shear modulus of the infinite space
E	Young's modulus
ν	Poisson's ratio
V_{LC}	volume of the layered cylinder

"Enquanto há vida, há esperança."

Eclesiastes 9:4

1
Introduction

1.1.
Motivation

Artificial intelligence algorithms have affected society's system of production due to their ability to process a large volume of data (ZHANG; LU, 2021). Its influence has covered the most diverse industries and sectors such as automotive (XING; XU, 2001), health (HAMET; TREMBLAY, 2017), financial (YANG et al., 2001), food production (KAKANI et al., 2020), among other sectors.

The influence of these algorithms in structural engineering has been observed from activities on a macro scale, such as monitoring and inspection of infrastructure (SPENCER; HOSKERE; NARAZAKI, 2019), as well as activities related to micro scales, such as the correlation between concrete strength and mechanical properties (LEE; LEE, 2014). In the oil and gas industry, and more precisely in geomechanics, artificial intelligence has also been used in activities of different scales, ranging from the characterization of exploration fields (NOURAFKAN; KADKHODAIE-ILKHCHI, 2015) to the prediction of the uniaxial strength of different types of rocks (TARIQ et al., 2017).

Although the concept of artificial intelligence was formulated at the beginning of the 20th century, when some classic algorithms were also proposed, it was only with the advent of computers that applications using AI received more attention. A similar phenomenon occurred with computational mechanics, whose numerical methods, such as the finite element method (FEM), had already been formulated at the beginning of the 20th century.

Analyzing the developments in computational mechanics and AI, it can be observed that there is an intrinsic relationship with intensive numerical calculations in both cases. Considering this relationship and through a structured review of the literature, this research work analyzed how artificial intelligence algorithms can

contribute to the development of numerical methods for analyzing the reservoir's geomechanics. It is important to emphasize that the methods developed in this work can be adapted to applications in other types of mechanical problems.

The oil and gas industry has huge impact in the Brazilian economy. For example, according to ANP its participation in Brazilian´s GDP was 13% in 2020. Geomechanics is the basis for the analysis of several important applications in this area. In particular, reservoir geomechanics has the challenge of analyzing and enabling the extraction of oil and gas from Brazilian pre-salt reservoirs. Due to the dimensions of the problem, pre-salt geomechanical models presents many degrees of freedom, which impacts the processing time of numerical analyses.

In this context, this work presents three developments based on the Green's functions approach applied to reservoir geomechanics. The first approach uses concepts from classical mechanics, such as the static equilibrium and the reciprocity theorem. This approach depends on iterative calculations which can be time consuming as the number of degrees of freedom increases. The other two methods apply artificial neural networks (ANN) to the first approach. The aim of the two ANN-based methods was to reduce the number of degrees of freedom necessary to solve the geomechanical problem and, thus, reduce the processing time, which is crucial for decision-makers to quickly act in field applications.

1.2.
Objectives

The main objective of this research is to develop reliable and efficient numerical methods for applications in reservoir geomechanics. Efficiency is achieved by means of the application of artificial intelligence methods, which aim to reduce the model's number of degrees of freedom, and consequently, reduce CPU time requirements when compared to traditional numerical methods such as the finite element method.

To achieve the main objective, the following specific objectives of the work are:

- Conduct a literature review to verify the state-of-art on the application of artificial intelligence to numerical methods applied to geomechanics/mechanics.

- Develop a Green's functions approach applied to reservoir geomechanics using concepts from classical mechanics.

- Propose a super element using artificial neural networks, which is capable of reducing the number of elements used in the discretization of the geomechanical problem.

- Develop an ANN-based Green´s function approach to analyze stratified domains.

1.3.
Organization

This thesis is structured in a manuscript format, in which some chapters consist of papers published or submitted for publication in peer-reviewed international journals. The main authorship of these papers belongs to the author of the present thesis, while co-authors contributed with discussions and text revision. Together with the author of this thesis they form a research group created to carry out the following project: "A study on salt rocks creep and the 4D effects in pre-salt fields in Brazil".

Chapter 2 presents the main concepts of artificial neural network as well as concepts of classical mechanics, such as Gauss-Green theorem and the integration of singular functions. Chapter 3 describes the structured literature review that was carried out to understand the state-of-art on how AI and numerical methods can be coupled, especially for geomechanics. Chapter 4 presents the manuscript titled "Stress evolution in elastically heterogeneous and non-linear fluid saturated media with a Green's function approach", which was published in International Journal for Numerical and Analytical Methods in Geomechanics. This chapter deals with the formulation and validation of the Green's function approach. Chapter 5 consists of the manuscript titled "Intelligent element: Coupling Green Function approach and artificial intelligence to reduce discretization effort" which was published in International Journal for Numerical and Analytical Methods in Geomechanics. This chapter presents an intelligent element based on Artificial Neural Networks, which is capable of predict the strain field inside the element considering its geometry, and nodal displacements. With this super element, the mesh can have fewer

elements than the ones used in the original method described in Chapter 4. Chapter 6 consists of the manuscript "ANN-based Green's function approach for reservoir geomechanics", which has been submitted to a peer-reviewed Journal. This chapter describes an ANN-Green´s function approach, in which artificial neural networks are trained to be used as Green's function for stratified media. Finally, Chapter 7 summarizes the conclusions of this research and provides directions for future work. A list of references is provided after Chapter 7.

2 Theoretical background

This chapter presents a review on artificial neural network and on concepts of classical mechanics such as the Gauss-Green theorem and the integration of singular functions, which are used on this research work.

2.1.1.
Artificial neural network

Artificial intelligence (AI) is a field of computer science whose purpose is to reproduce behaviors observed in nature through algorithms. Among the types of AI algorithms, those that seek to simulate the human ability to make predictions or recognize patterns based on experiences are classified as machine learning algorithms. Artificial neural networks (ANN) belong to this class, which can be of various types, such as multilayer perceptron, LSTM (Long Short Term Memory), and convolutional.

Multilayer Perceptron neural networks are the most widely used due their generalization capability for classification and prediction problems. Furthermore, it is simpler when compared to other types. This type of ANN can be used to predict the failure of a structural element and to rate the credit risk for bank customers, for example.

LSTM neural networks are usually used for problems with temporal characteristics. Application examples vary from predicting the value of companies traded on the stock market to creating texts.

Convolutional neural networks are those that make use of image data, either as input or output data. One example convolutional ANN that use images as input data is the one capable of modelling different structural elements based on point clouds. An example of a neural network whose output data is an image is the GAN (Generative Adversarial Networks), which can be used to create fictitious faces.

2.1.2.
Processing unit

The concept of an artificial neural network is based on the information processing done by the human nervous system. Similarly, the basic processing unit, or artificial neuron, that composes an ANN is based on the biological neuron.

The artificial neuron, as a biological neuron, has elements capable of capturing and transmitting impulses (information), and an element for processing the received information. These two regions are indicated in Figure 2.1 by the colors blue and red, respectively.
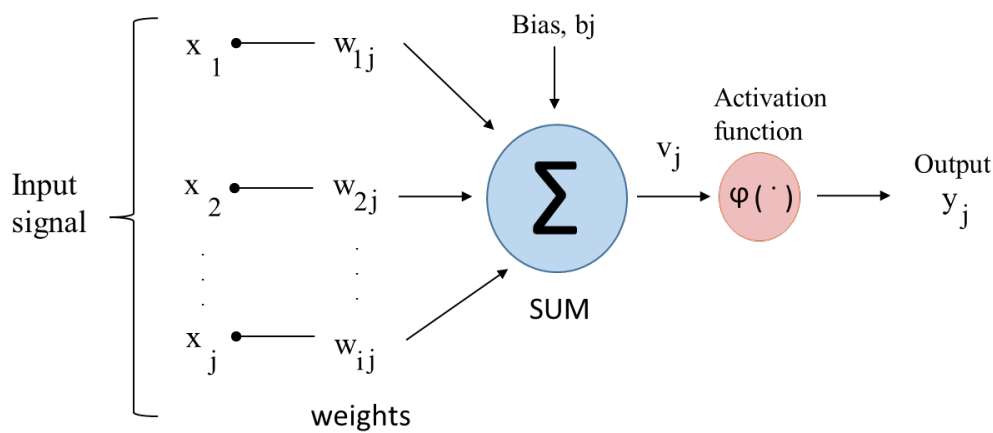
Figure 2.1 – Artificial neuron (HAYKIN, 2009).

Mathematically, an artificial neuron can be understood as a composite function, given by equation (2.1):

$$y_j = \varphi\left(v_j(x_i)\right), \tag{2.1}$$

in which x_i are the neuron input data, y_j is the output of the neuron j, $\varphi(v_j)$ represents the activation function and $v_j(x_i)$ is a summation show in equation (2.2):
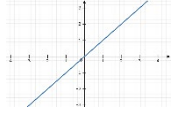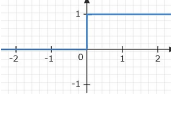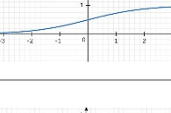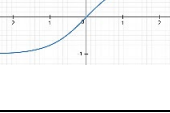
$$v_j = \sum_{j=0}^{n} w_{ij}x_i + b_j, \tag{2.2}$$

in which n is the number of information received, w_{ij} is a weight which multiplies the information x_i received by neuron j e b_j is the bias of the neuron j.

Activation functions are responsible for determining the amplitude of the output value and can be of various types, depending on the problem to which the network will be applied (HAYKIN, 2009). In addition, the choice of activation function impacts the computational effort for training and applying the neural

network model. Table 2.1 shows some types of activation functions commonly used.

Table 2.1 – Activation function

Name	Mathematical expression	Range	Graph
linear	$\varphi(v_j) = v_j$	$(-\infty, +\infty)$	
step	$\varphi(v_j) = \begin{cases} 0 \; para \; v_j < 0 \\ 1 \; para \; v_j \geq 0 \end{cases}$	$(0,1)$	
sigmoid	$\varphi(v_j) = \dfrac{1}{1 + e^{-v_j}}$	$(0,1)$	
hyperbolic tangent	$\varphi(v_j) = \tanh(v_j)$ $\varphi(v_j) = \dfrac{e^{(v_j)} - e^{-(v_j)}}{e^{(v_j)} + e^{-(v_j)}}$	$(-1,1)$	

2.1.3.
Topology

Individually, neurons have limited generalization capability, but when grouped in layers and sequenced as a network they are capable of modeling complex phenomena. The number of layers, the number of neurons in each layer, and the connection between layers is the topology of the neural network.

Networks can be classified according to the direction of the information flow into recurrent or sequential. An example of recurrent networks is the LSTM type, and an example of sequential networks is the multilayer Perceptron type, represented in Figure 2.2.
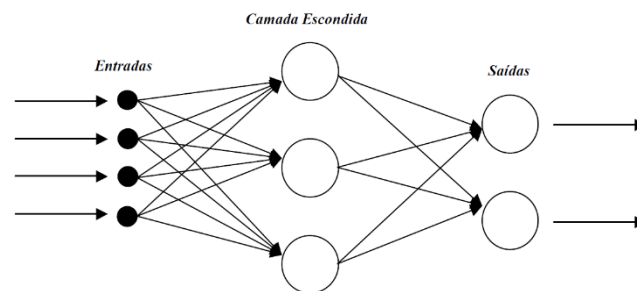
Figure 2.2 – MLP structure.

Figure 2.2 shows the three regions of the network, the input layer, the hidden layers, and the output layer. When using Perceptron networks, the number of hidden layers and the number of neurons in each hidden layer are important parameters for the performance of the network (MÜLLER; GUIDO, 2017). According to the universal approximation theorem, a Perceptron network of a single hidden layer is sufficient to uniformly approximate any continuous function, if representative data set is provided (CYBENKO, 1989). However, this does not mean that the single-layer network is the most easily constructed or has the best generalization capability for any data set (HAYKIN, 2009).

2.1.4.
Training process

In this work, neural networks are used for predictions. To make consistent predictions it is necessary that the weights and biases be calibrated to the desired phenomenon. The procedure for calibrating these parameters is called neural network training. Among the existing training algorithms, Backpropagation is the most widespread and used in the literature, being particularly suitable for sequential networks that have differentiable activation functions (HAYKIN, 2009). The training process demands a dataset of inputs and their respective outputs. The samples must be representative of the possible situations so that the trained network can predict the desired phenomenon.

The Backpropagation algorithm can be divided into two phases: propagation and backpropagation. In the first phase, the functional signal is propagated through the network from the input layer to the output layer, while the weights and biases are fixed. This propagation is basically an attempt to make predictions from the input data. The results of these predictions are compared with samples of the output data, producing an error signal. In the second phase, the result of this error is propagated again, layer by layer, from the output to the input. In this phase the weights and biases of the neurons are successively adjusted by an optimization algorithm (Figure 2.3), aiming to reduce the error measurement. This error can be evaluated in different ways, some of them are exemplified in Table 2.2.
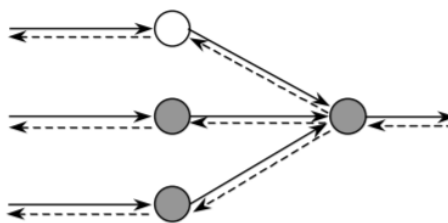
Figure 2.3 – Propagation of the functional signal in solid line and back-propagation of the error signal in dashed line (adapted from Haykin, 2009).

Table 2.2 – Error measurements

Name	Mathematical expression*
MAE (mean absolute error)	$MAE = \dfrac{1}{n}\sum_{i=1}^{n}\dfrac{|Y_i - \hat{Y}_i|}{Y_i}$
MSE (mean squared error)	$MSE = \dfrac{1}{n}\sum_{i=1}^{n}(Y_i - \hat{Y}_i)^2$
MAPE (mean absolute percentual error)	$MAPE = \dfrac{100\%}{n}\sum_{i=1}^{n}\dfrac{|Y_i - \hat{Y}_i|}{Y_i}$

* In the mathematical expressions presented n indicates the number of samples, Y_i is the reference value e $\hat{Y}_i$, is the predicted value.

The optimization algorithm used during the back-propagation step can be gradient-based such as gradient descent and ADAM (Adaptive Moment Estimation) (KINGMA; BA, 2015) or heuristically-based such as particle swarm, genetic algorithm, and ant colony. In general, gradient-based algorithms are more efficient for training (HAYKIN, 2009). These algorithms have in their formulation a learning rate related to the algorithm's ability to "escape" from local minima. This process of propagation and backpropagation is repeated iteratively, and each iteration of all training samples is called epoch. The training process continues until the stipulated number of epochs is reached, or the value of the error function reaches the desired value.

Another way to determine the number of epochs for training is using a validation group, which should be different from the training group. At the end of each epoch the error value measured on the validation set should be checked. When it is observed that this error is no longer reducing, it is recommended that training be stopped, even if the training error is reducing. Otherwise, the ANN will tend to

over-fit the training data, and this reduces the generalization capability of the network.

Another factor that affects the number of epochs and its convergence, is the initialization of weights and biases (GLOROT; BENGIO, 2010). This initialization can be done using random values or it can be probability-based, as presented by Glorot and Bengio (2010).

After training, the trained neural network is tested, using a third database different from the other two already discussed, which is called test group. If the error function for the test group reaches values similar to those obtained for training and validation groups, the trained neural network is considered capable of generalizing and representing the phenomenon characterized by the database.

Since the training algorithm is valid for a variety of network topologies, which can be applied to any phenomenon, it is important to use normalized input and output data. Furthermore, the same neural network may have input and output data of different magnitudes. Therefore, normalization is also recommended to prevent the values of some variables from becoming more significant than others during training. Normalization is usually done in the range (0,1) or (-1,1).

2.2.
Gauss-Green theorem

Gauss' theorem states that the flow over a closed surface $\partial\Omega$ of a vector field F_i that has the partial derivatives of its continuous components in the region Ω (Figure 2.4) is equal to the integral of the divergent of F_i in region Ω. Mathematically Gauss' theorem is expressed by equation (2.3).
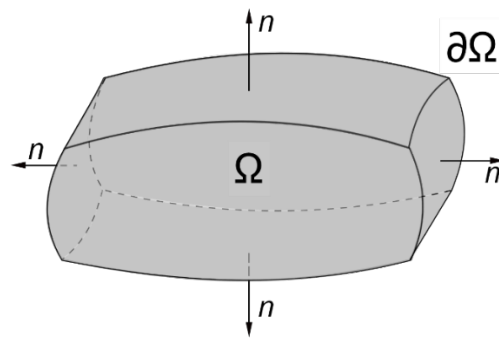
Figure 2.4 – Region Ω defined by surface $\partial\Omega$.

$$\int_{\Omega} \nabla F_i \ dV = \int_{\partial\Omega} F_i \, n_i dS \qquad (2.3)$$

in which n_i is the normal vector to the surface $\partial\Omega$.

The Gauss' theorem for the bidimensional case is known as Green's theorem and can be write as shown in equation (2.4)

$$\int_{\Omega} \frac{\partial Q}{\partial x} - \frac{\partial P}{\partial y} \ dA = \int_{\partial\Omega.} P dx + Q dy \qquad (2.4)$$

in which P and Q are components of the vectorial function F_i.

2.3.
Singular Integration

The solution of singular integrals is a challenge that needs to be faced to obtain the solution of boundary value problems from methods that use a fundamental solution. The way to handle the singularity is dependent on its type. For example, singularities due to the presence of terms $\ln\left(\frac{1}{x}\right)$ can be solved using weighted Gauss quadrature, when it is possible to isolate the singular term from the expression.

In the case of area integration over flat or three-dimensional domains, which have singularities of the type $\frac{1}{x}$, it is possible to perform the Duffy transformation. This strategy can be applied to triangular domains (for the two-dimensional case) and pyramidal domains (for the three-dimensional case).

2.3.1.
Weighted Gaussian integration

The Gaussian quadrature using $\ln\left(\frac{1}{x}\right)$ weight function can be expressed by equation (2.5):

$$\int_0^1 f(x) \ln\left(\frac{1}{x}\right) \ dx = \sum_{s=1}^{S} w_s f(x_s) \qquad (2.5)$$

in which w_s and x_s are weights and abscissas, given in Stroud and Secrest (1966), and also listed in Table 2.3.

Table 2.3 – Abscissas and weights for Gauss quadrature with $\ln\left(\frac{1}{x}\right)$ weighting factor

	x_s	w_s
2	0.112008806166976	0.718539319030384
	0.602276908118738	0.281460680969615
4	0.041448480199383	0.383464068145135
	0.245474914320602	0.386875317774762
	0.556165453560278	0.190435126950142
	0.848982394532985	0.039225487129960
6	0.021634005844117	0.238763662578547
	0.129583391154950	0.308286573273946
	0.314020449914765	0.245317426563210
	0.538657217351802	0.142008756566476
	0.756915337377402	0.055454622324886
	0.922668851372120	0.010168958692932
8	0.013320244160892	0.164416604728002
	0.079750429013895	0.237525610023306
	0.197871029326188	0.226841984431919
	0.354153994351909	0.175754079006070
	0.529458575234917	0.112924030246759
	0.701814529939099	0.057872210717782
	0.849379320441106	0.020979073742133
	0.953326450056359	0.003686407104028

2.3.2.
Duffy's transformation

The generalized Duffy's transformation maps the physical domain to a parent domain in order to vanish singularities of the type $\frac{1}{x}$ through the consideration of the Jacobian. In a tridimensional space the mapping is set as show in equation (2.6):

$$(u,v,w) \rightarrow (u,v,w): x = u^\beta, y = xv^\gamma, z = xw^\alpha \qquad (2.6)$$

in which β, γ and α are selected to smooth the integrand. This transformation maps the standard pyramid with vertices at (0, 0, 0), (1, 0, 0), (1, 1, 0), (1, 0, 1), and (1,

1, 1) to a unit cube (MOUSAVI; SUKUMAR, 2010). For the bidimensional case this transformation maps the triangle shown in Figure 2.5(a) to the square shown in Figure 2.5(b).

(a) $0 \leq x \leq 1$, $0 \leq y \leq x$ **(b)** $0 \leq u, v \leq 1$
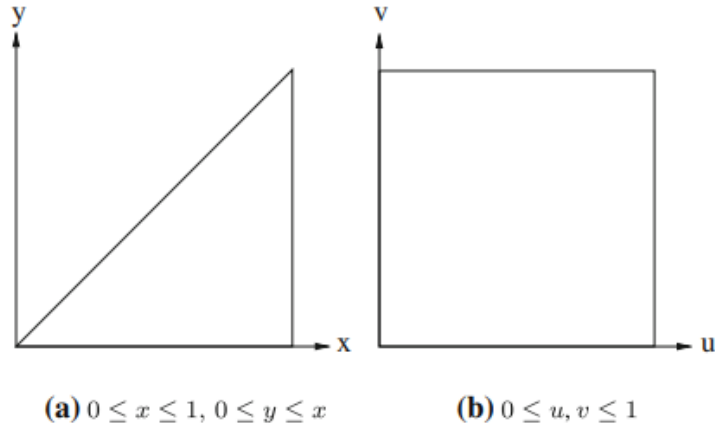
Figure 2.5 – Bidimensional Duffy's Transformation. (MOUSAVI; SUKUMAR, 2010)

3
Literature review on the state-of-art in artificial intelligence applied to geomechanics and mechanics

This chapter presents a structured literature review to understand the state-of-art on how AI and numerical methods can be coupled, especially for geomechanics and mechanics.

3.1.
Methodology

The literature review was performed in order to identify scientific papers that addressed the application of artificial neural networks in numerical methods. According to Webster and Watson (2002), a structured literature review (SLR) facilitates the development of theories, avoiding focusing on intensively studied areas and finding gaps in knowledge. This is possible due to the clarity and reproducibility of the procedures and criteria adopted that this method presents.

The SLR was carried out in three stages: formulation of the question to be answered, location of the articles, and analysis of the results. Thus, it was defined the question which the literature review would seek to answer was: "How machine learning and numerical methods are integrated in geomechanical simulations?". Through the selection of articles that tried to answer this question it is expected to determine the state-of-the-art in this area, and thus assisting the definition of the path the research should follow.

The paper search was conducted in the *Periódicos Capes* database (which encompasses Scopus, Web of Science and Engineering Village), without limitations regarding the year of publication and using the following combination of key words:

- "geomechanical" or "geomechanics" and

- "numerical methods" or "finite element" or "FEM" or "boundary element" or "BEM" or "discrete element" or "DEM" and

- "machine learning" or "artificial neural network" or "ANN" or "deep learning"

When using this combination, eleven scientific papers were found, five of which were published in conferences and six in peer-reviewed journals. Among these papers, three distinct types of applications of machine learning integrated with numerical methods in geomechanics were observed:

- Inverse analysis (SOUZA; ROEHL, 2019; ZHANG et al., 2020a, 2020b),

- Meta models for massif based on in situ measurements (ALBAHRANI; PAPAMICHOS; MORITA, 2021; BOBET, 2010; DEO, 2010; TANDON, 2019; VASILYEVA et al., 2021; ZHANG et al., 2014, 2016),

- Modeling of rock mechanical properties (ALERIGI; BATARSEH; ASSIRI, 2020; HEIDER; SUH; SUN, 2021).

Only two research works were found that propose a numerical method based on machine learning. Zhao (2021) proposed a model reduction to predict displacements and stresses combining "proper orthogonal decomposition" (POD) and "multi-output support vector machine" (MSVM). To achieve this, it is necessary to generate finite element models with different properties (elasticity modulus, Poison's ratio and initial stresses) and their respective orthogonal decomposition. Then the MSVM algorithm generates a relationship between the coefficients of the POD vectors and the properties of the model under study. Thus, this method requires that for each new model of different geometry the entire procedure be performed again. Abreu et al. (2022) propose an artificial intelligence-based methodology to identify geomechanical parameters from borehole injection pressure curves obtained during hydraulic fracturing tests. This methodology adopts a multilayer Perceptron ANN as a proxy model that substitutes hydraulic fracturing numerical simulations, thus, substantially reducing computational time.

Based on the small number of papers found during the SLR, it became clear that there is a gap in knowledge concerning the integration between machine learning and numerical methods applied to geomechanics. Thus, in order to verify

whether this gap also exists for the simulation of other mechanical problems, the first group of keywords was generalized to become:

- "geomechanical" or "geomechanics" or "mechanical" or "mechanics" or "stress" or "strain" or "displacement"

This second search returned a total of 1827 papers, indicating that machine learning has been applied in some way to numerical methods to solve mechanical problems. To better filter the papers that actually studied the integration between the two areas and not just applied the two methods together, the following three-stage filtering process was performed:

1. Reading the titles and abstracts

2. Reading the conclusions

3. Reading the full article

During the filtering process it was observed three main areas where artificial intelligence and numerical methods appeared working together: biomechanics, modeling of constitutive properties, and structural safety monitoring of bridges and viaducts. However, after the filtering process only thirteen articles remained that somehow used artificial intelligence to modify or develop numerical methods.

3.2.
Literature review findings

The articles filtered in the second search can be classified into three groups. The first group is composed of papers that used results from numerical methods to train a neural network in order to obtain answers with a smaller processing time. Ghavamian and Simone (2019) proposed the use of recurrent neural networks to speed up simulations in which the problem was modeled at two different scales: one micro and one macro. The network was trained to resembles a nonlinear finite element analysis procedure to solve the micro scale equilibrium. Since the problem is multi-scale, it is solved by iterating between the micro and macro scales. The micro scale analysis is replaced by a neural network which reduced the processing time.

Mendizabal et al. (2020) calibrated a U-net architecture network to be able to relate surface forces, applied to a body of any geometry, to the respective displacement field they generate. The main goal of this development was to enable

biomechanical simulations to be performed in less time. They also noticed that the network achived more accurate results for stiffer materials, which may show that the training set had few data for softer materials.

Also in the field of biomechanics, Liang (2018) built and trained a deep learning network to calculate the von-Mises stresses in the aortic vein using as input medical examination images. This approach speeded up the medical decision-making process for two reasons. First, because it is no longer necessary to build a finite element model, and second, because the processing time of the network is much shorter than the processing time of the finite element method.

The second group observed among the filtered articles is composed of papers that used artificial neural networks to solve differential or integral equations. Most papers in this group do not discuss the processing effort demanded by the proposed approach.

Samaniego et al (2020) and Nguyen-thanh et al. (2020) used the concept of minimum potential energy as an objective function for training a neural network capable of predicting the displacement of a given body under effect of external forces. The results were obtained with good precision when compared with the results obtained by the FEM. However, the authors do not clarify the computational effort demanded by this method. It is assumed that this effort is high, as the network training requires a lot of computational effort and needs to be performed again for each new model.

Lin et al. (2020) proposed the training of a neural network using the partial differential equation for heat transfer in a porous medium as an objective function. According to the authors, this network can predict the temperature at any point inside the studied body.

Nabian and Meidani (2019) suggested the use of ANNs to solve partial differential equations (PDE). For this, they used the PDE that governs the problem to be solved as an objective function. The develop method was applied to heat transfer problems and its accuracy was verified.

Huang et al. (2020) proposed to solve low-order nonlinear partial differential equations in two phases. In the first phase a neural network was trained, using the PDE that describes the problem as the objective function in order to obtain an initial result. In the second phase an iterative process was initiated considering the result obtained in the first phase as the initial solution. This iterative process could apply

the Newton's method, for example. The network used in the first phase provides a good initial estimate of the response, thus, decreasing the iterative effort to obtain the solution of the PDE.

Brevis et al (2020) coupled an artificial neural network model with the weighted residuals method for solving PDEs. It was found that the use of the proposed approach provided an accurate solution using a less refined discretization than a FEM mesh.

The third set of papers found after the filtering process gathers articles that worked on the development of elements based on neural networks. Capuano and Rimoli (2019) developed a method that couples any machine learning algorithm and the finite element method for solving nonlinear mechanical problems. By using the proposed method, the internal forces in the element, which are necessary for iterative calculation of the equilibrium in nonlinear problems, are calculated in a direct way. This means that there is no need to calculate the nodal displacements to then obtain the internal forces. In this method the stiffness matrix is obtained by numerical derivation of the nodal forces provided by the AI.

Koeppe et al. (2020) also proposed a method in which the stiffness matrix is calculated from the nodal forces. This calculation is done through a recurrent convolutional neural network whose input data were the nodal displacements. This network was developed for elements whose material is Prandt-Reuss elastoplastic with a Levy-Saint-Venant flow law.

Jung et al. (2020) suggested the use of a neural network to relate the nodal displacements and internal strains of a linear elastic quadrilateral element. The authors developed two networks, one for bilinear quadrilateral elements and one for quadratic quadrilateral elements. The Convergence was also verified and the developed elements presented more accurate results when compared to traditional finite elements.

Liu (2020) proposed the use of artificial neural networks as the shape function of any finite element. Comparisons were also made with analytical simulations in order to verify the accuracy of the element. However, an evaluation of the computational effort of this type of element was not done.

In summary, the articles that compose group one present solutions with a computational performance gain higher than the solutions presented by other works, but the situations in which these solutions can be applied are more specific. The

solutions presented in set two are applicable to any differential or integral equation, but their computational cost is high. The works in the third set, on the other hand, show a balance between generalization capability and computational performance. For this reason, it can be implied that the use of artificial intelligence to modify numerical methods is the most promising way to integrate these two areas.

Therefore, the present work follows the tendency identified in group three by improving the originally proposed Green's functions approach using artificial intelligence. The first improvement consists of using an intelligent super element capable of providing less discretized meshes than traditional elements. The second improvement consists of creating ANN-based Green's functions for stratified media, which demand only the reservoir discretization to solve reservoir geomechanics problems. It should be noted that both approaches can be expanded to other mechanical problems beyond the reservoir geomechanical application.

4
"Stress evolution in elastically heterogeneous and non-linear fluid-saturated media with a Green's function approach"

Abstract

Classical analytical solutions of linear elasticity are used as auxiliary solutions to solve non-linear, and elastically heterogeneous problems on fluid-saturated media. The 2D Kelvin's solution for a homogeneous space is considered here for simplicity sake. The material non-linearity could be due to irreversible deformations or non-linear elasticity response typical of 4D analysis as it is done here. The general procedure relies on a discrete collocation method and a fixed-point iterative approach to construct the displacement field. The method is validated by comparing the numerical results with the analytical solution for a layered cylinder embedded in an infinite space. The h-convergence is checked numerically illustrating the strong influence of the number of facets used to discretize the boundaries. The convergence of the iterative process based on the displacement norm is of a quasi-quadratic rate for near homogeneous materials and declines to sub-linear rates as the contrast in elasticity modulus exceeds 15% of the values considered for the Green's function. The method is then applied to a 2D tilted block region where the depleting reservoir has elasticity parameters function of the volumetric strain, to shed some light on the 4D effects. It is shown that the velocity changes are sensitive to the volumetric strain as well as to the strain in the wave propagating direction. Differences, including the anisotropy due to the structural response at the field scale, between the predictions based on this non-linear isotropic elasticity and the classical R-factor approach are finally discussed.

4.1.
Introduction

The results of a feasibility study on the use of Green's functions for solving problems with two technical difficulties are presented. The first difficulty is the introduction of elasticity heterogeneities and the second, the account of material nonlinearities.

The first objective of this contribution is, thus, to solve heterogeneous elasticity problems using Green's functions as auxiliary solutions. The application of Green's functions has been instrumental to forge our understanding of the response of reservoirs at the field scale, to relate for example compaction to subsidence (GEERTSMA, 1973a) and to estimate stress changes (SEGALL, 1985). Another approach often discussed in literature is the use of the Eshelby inclusion (ESHELBY, 1957) approach as discussed by Walsh (2002). These various approaches are equivalent as pointed out by Rudnicki (2011). A thorough literature review of this topic is found in Lehner and Knoglinger (2005). Such applications are still used nowadays for exploration purposes when data are scarce or for checking complex model development. The basic theorem which makes these Green's functions of interest is the theorem of reciprocity which applies to linear elastic material even if it is heterogeneous. Consider a domain with two independent modes of loadings, including the fluid pressure, and the two associated and independent solutions, which include the displacement and the linearized strain, and are referred to as the effects. The theorem states that the work of the first loading on the second effect, which is to be determined, is equal to the work of the second loading on the first effect. The auxiliary problem and its Green's function correspond to a point load, applied within or around the reservoir, which is composing here the first loading. The work of this point load on the unknown effect provides the displacement at its point of application. In the presence of fluid pressure changes, the solution technique to estimate this displacement amounts to the computation of an integral over the reservoir of the work done by the fluid pressure change on the volumetric part of the auxiliary volume change. This integral formulation is completely analogous to Maysel's integral solution developed in thermo-elasticity, as pointed out by Lehner and Knoglinger (2005). The key

question is then whereas the appropriate Green's function for the geological setting and the distribution of material properties of interest is available in the literature.

The application of the Green's functions as auxiliary solutions for solving realistic geoscience problems is indeed impeded by the simplicity of the material distribution classically considered which is either homogeneous (MINDLIN, 1936) or horizontally layered (see Pan (1997) for a discussion in the static case). The choice of a layered half-space is already sufficiently complex, often requiring a numerical scheme for inversion to the physical space, to hinder its every-day application. It is proposed in this contribution to keep on using the simple Green's function for the homogeneous space or half-space and to introduce the material heterogeneities during an iterative procedure in which a Maysel type of formula is solved at each step up to convergence. This idea is rather reminiscent of the approach considered in the field of micro-mechanics where the auxiliary solution for a homogeneous space is used to solve heterogeneous composite problems (see Moulinec and Suquet (1998) for further references). The main difference is that we consider infinite or semi-infinite spaces here and not periodic domains.

The use of simple Green's functions for homogenous infinite space or half-space remains attractive because of the lack of data away from the reservoir domains. It is indeed within the reservoirs that most of the data have been acquired. The cap rock bounding the reservoir is the key location for integrity analysis. Moreover, the accuracy and the amount of information on the geological conditions decreases as we move away from the reservoirs. A method which combines the complexity of the geometry of the reservoir and its close surrounding with a simplified description at the regional scale is, thus, well adapted for this class of engineering problems.

The second objective of this contribution is to account for material non-linearities extending again Maysel's formalism. The integral is then not only on the reservoir and the region where elasticity heterogeneities are, but also on the regions where non-linearities develop. The new integrand is the work done by the stress deviation from the one based on the homogeneous linear elasticity properties on the conjugate auxiliary strain. There is a strong analogy between the proposed method and the application of boundary integral approach to elasto-plasticity, the first contribution being due to Swedlow and Cruse (1971). The method has received subsequently some attention (e.g., (TELLES; BREBBIA, 1979)). The main

difference between the proposed approach and the classical boundary-integral approach (see Bonnet (2017) for a recent review) is that we do not solve a global system of equations for displacements on the boundary domain, but determine the displacement or the strain at a set of points within the region where the fluid pressure is modified or where the material properties, due either to elasticity heterogeneities or non-linear deformations, deviate from the one considered for the auxiliary problem. This approach is perfectly suited for parallel computation and especially for GPU computer architecture.

The main application presented in this contribution concerns the role of the stress change on 4D effects defined as the variation of the wave velocities within and around reservoirs. An extensive review and discussion on this topic is found in Herwanger (2014). It is proposed here to capture these 4D effects with a non-linear elasticity approach starting with an energy in which the incompressibility and the shear moduli are assumed function of the volumetric strain. This constitutive model belongs to the class of third-order elasticity which has been extensively studied in the mechanics literature for various applications such as plate buckling (MARKENSCOFF; TRIANTAFYLLIDIS, 1979) and more recently for 4D effects (HERWANGER; HORNE, 2009). The proposed version is certainly less general as in these two references but its simplicity is found appealing for comparison with laboratory experiments. Compared to Herwanger and Horne (2009), it also offers the possibility to link the static and wave analysis within the same framework. This phenomenological approach is certainly also an over-simplification compared to the microstructural approach of Sayers and Kachanov (1995), which has shown its strength at the laboratory scale (FORTIN; GUÉGUEN; SCHUBNEL, 2007). The proposed phenomenological approach is nevertheless found convenient for a first comparison with the classical R-factor approach of Hatchell and Bourne (2005) and a potential inversion approach (MASTIO et al., 2020).

The contents of this contribution are as follows. The next section contains the theoretical background introducing first the non-linear constitutive relations (non-linear poro-elasticity and visco-plasticity) including the introduction of a deviation in the elastic properties from the homogeneous auxiliary problem. This second section contains also a presentation of the reciprocity theorem ending up with the proposed Maysel's formula for heterogeneous and non-linear media. The numerical scheme is presented in subsection 3 and relies on an iterative discrete

collocation method (ATKINSON; FLORES, 1993). The numerical quadrature needs some care because of the Green's function singularities and is presented in Appendix B. The approach is validated in subsection 4 in which the numerical predictions for the problem of a layered cylinder embedded in an infinite space are compared with the analytical solutions presented in Appendix C. The spatial as well as the iterative convergences are presented considering elasticity modulus contrast from the value considered for the Green's function up to 90%. The convergence of the iterative algorithm in displacement norm is nearly quadratic for a few percent in relative elasticity modulus contrast. The convergence is linear for 15% contrast and degrades non-linearly for larger elasticity contrast. Subsection 5 is devoted to a field application for a reservoir in a tilted blocks system with a variation in elastic properties around the reservoir. The non-linear material response is introduced in the reservoir with elasticity moduli function of the volumetric strain as discussed above. The 4D effects are computed with the classical R-factor approach of Hatchell and Bourne (2005) as well from a direct construction based on the acoustic tensor presented in Appendix D. The main difference between the two approaches is that the former relies only on the vertical strain whereas the latter introduces a complementing dependence on the volumetric strain and is applicable to any propagation direction.

4.2.
Theorical Background

Basic notations and definitions are first presented before discussing simple linear and non-linear constitutive relations. The same formalism is proposed for the non-linear constitutive relations and also for the heterogeneous elasticity. The reciprocity theorem for porous media is then extended to account for the non-linearities and the material heterogeneities.

4.2.1.
Stress, fluid pressure change, and mechanical equilibrium

The initial stress and fluid pressure within the domain of interest Ω_t are denoted by $\sigma_{0_{ij,j}}$ and p_{f0}. The production is accompanied by a change in the fluid pressure denoted Δp_f in the reservoir, a sub-domain denoted Ω_R, and resulting in a change in stress $\Delta\sigma_{ij,j}$ over the whole domain. Note that second-order tensors and

vectors are underlined twice and once only, respectively. Mechanical equilibrium for the total stress (initial + change) is enforced by the local conditions at any material point pointed by the vector x_i within the domain Ω_t. The vector field f_i is an external field such as the gravity (ρg_i with ρ the material volumetric mass and g_i the gravity acceleration) or could be a general force such as a point load. This differential equation set is completed by boundary conditions on $\partial\Omega_t{}^T$ where the force density is prescribed (the stress vector T_i is equal to the force density $T_i{}^d$). The complement to this boundary domain is $\partial\Omega_t{}^u$, a surface where the displacement is known.

$$\left(\sigma_{0ij,j} + \Delta\sigma_{ij,j}\right) + f_i = 0 \quad \forall\, x_i \in \Omega_t, \tag{4.1}$$

It is assumed that the transformation in terms of displacement (u_i) and deformation due to the fluid pressure changes is a small perturbation: the displacement is small compared to the characteristic problem length (e.g., depth of reservoir or reservoir thickness) and the deformation norm is small compared to one. The first consequence is that the linearized strain tensor is applicable

$$\varepsilon_{ij} = \frac{1}{2}\left(u_{i,j} + u_{j,i}\right). \tag{4.2}$$

The second consequence it that in the absence of geometrical effects in equation (4.1), the local equilibrium conditions for the stress changes are

$$\Delta\sigma_{ij,j} + f_i = 0 \quad \forall\, x_i \in \Omega_t, \tag{4.3}$$

in which f_i is any field of interest, except for the gravity effects since equation (4.1) is satisfied by the initial stress prior to any stress change.

In summary, the typical boundary valued problem to be solved is one where the displacement and strain are initially set to zero and the stress and fluid pressure are σ_{0ij} and P_0. The change in boundary conditions ΔT_i on $\partial\Omega_t{}^T$ or in displacement $u_i{}^d$ on $\partial\Omega_t{}^u$ or in fluid pressure over the sub-domain Ω_t results in a displacement field u_i, a linearized strain according to equation (4.2) and a stress change $\Delta\sigma_{ij}$ which satisfies the local equilibrium conditions (equation (4.3)) and the appropriate force density boundary conditions. These local equilibrium equations can also be equivalently enforced by satisfying the theorem of virtual work which reads

$$\int_{\Omega_t} \Delta\sigma_{ij}\,\hat{\varepsilon}_{ij}\,\mathrm{d}V = \int_{\partial\Omega_t} \Delta T_i\,\hat{u}_i\,\mathrm{d}S + \int_{\Omega_t} f_i\,\hat{u}_i\,\mathrm{d}V, \tag{4.4}$$

for any virtual displacement field $\hat{u}_i$, equal to zero on $\partial\Omega_t{}^u$, and the associated linearized strain $\hat{\varepsilon}_{ij}$.

4.2.2.
Poro-elasticity and non-linear constitutive response

The objective is now to relate the stress change to the strain with three possible constitutive relations. The linear poro-elasticity is first introduced, followed by a simple non-linear elasticity model to capture the role of the stress change in 4D effects. The third model is a plasticity model to study for example compaction in a depleting reservoir. The final sub-section discusses the introduction of a deviation in the elastic properties from the standard values considered for the auxiliary problem. This key ingredient is presented with a common notation with the non-linear constitutive responses.

4.2.2.1.
Linear poro-elasticity

The poro-elasticity response is a linear relation between stress change, linearized strain, and fluid pressure change

$$\Delta\sigma_{ij} = \mathbb{C}^e_{ijkl}\,\varepsilon_{kl} - A_{ij}\,\Delta P, \tag{4.5}$$

in which $\mathbb{C}$ and A are the fourth-order compliance tensor and the second-order Biot tensor, respectively. Considering isotropic media for sake of simplicity, this relation is explicitly

$$\Delta\sigma_{ij} = \left(3KJ_{ijkl} + 2GK_{ijkl}\right)\varepsilon_{kl} - \alpha\delta_{ij}\,\Delta P, \tag{4.6}$$

in terms of the material parameters K, G and α which are the incompressibility, the shear modulus and Biot coefficient, respectively. Note that in equation (4.6), δ_{ij} is the second-order identity tensor and J_{ijkl} and K_{ijkl} are fourth-order tensors. The former and the latter applied to any second-order tensor provides its spherical and symmetric deviatoric part, respectively.

4.2.2.2.
Non-linear poro-elasticity for 4D seismic

During production, there are changes in wave velocities studied for risk assessment and referred to as 4D seismic effects. The solid skeleton contribution to the change in wave velocity is due to variations in elastic properties, typically the

incompressibility and the shear modulus for initially isotropic media. The link between static and dynamic moduli, the former required for geomechanics modeling and the latter for wave propagation analysis is discussed in Appendix D.

Let us consider the following strain energy potential for initially isotropic media

$$E(\varepsilon_{kl}) = \frac{1}{2}\varepsilon_{ij}\mathbb{C}^e_{ijkl}\varepsilon_{kl} - \alpha(\Theta)\delta_{ij}\Theta\,\Delta P,$$
$$\text{with } \mathbb{C}^e_{ijkl} = 3K(\Theta)J_{ijkl} + 2G(\Theta)K_{ijkl} \tag{4.7}$$

in which the material properties are function of the volumetric strain:

$$\Theta = \delta_{ij}\varepsilon_{ij}, \tag{4.8}$$

The stress change is the partial derivative of the strain energy function with respect to the linearized strain

$$\Delta\sigma_{ij} \equiv \frac{\partial\varepsilon}{\partial\varepsilon_{ij}} = \mathbb{C}^e_{ijkl}\varepsilon_{kl} - \alpha(\Theta)\delta_{ij}\Theta - \Delta\sigma_{C_{ij}},$$
$$\text{with } \Delta\sigma_{C_{ij}} = \left(\mathbb{C}^e_{ijkl} - \mathbb{C}_{ijkl}(\Theta)\right)\varepsilon_{kl} - \frac{1}{2}\left(\Theta^2\frac{\partial K}{\partial\Theta} + \gamma^2\frac{\partial G}{\partial\Theta}\right)\delta_{ij}, \tag{4.9}$$
$$\gamma^2 = 2\varepsilon_{ij}K_{ijkl}\varepsilon_{kl},$$

Equation (4.9) has been written to introduce the deviation from the linear response through the stress change $\Delta\sigma_{C_{ij}}$. The reference moduli $\mathbb{C}^e_{ijkl}$ are the moduli under in-situ stress conditions only (zero volumetric strain).

Two items are further discussed to complement this sub-section. First, the non-linearities considered in the validation and application subsections 4.3 and 4.4 are presented. They consist of the following linear dependences of the incompressibility and shear moduli on the volumetric strain

$$K(\Theta) = K_0(1 + h_K\Theta), \quad G(\Theta) = G_0(1 + h_G\Theta) \tag{4.10}$$

in which h_K and h_G are two dimensionless coefficients and K_0 and G_0 the incompressibility and the shear moduli prior to any deformation.

The second item to be discussed concern the velocity changes upon deformation. Appendix D proposes from the analysis of the acoustic tensor expressions for the P and S wave velocity changes. The relative change in P velocity for a wave propagating in the direction n_i is

$$\frac{\Delta c_P}{c_{P_0}} = \left(\frac{1}{2} + R_\theta\right)\Theta + Rn_iK_{ij}n_j, \text{ with}$$
$$R_\theta = \frac{1}{2}\frac{1+\nu}{1-\nu}h_k \text{ and } R = \frac{1-2\nu}{1-\nu}h_G, \tag{4.11}$$

in which ν is Poisson's ratio in the reference configuration and C_{P_0} the wave velocity in the reference configuration.

4.2.2.3.
Poro-visco-plasticity

Permanent deformation can occur during fluid pressure changes, the linear elasticity relations in equation (4.5) are then amended such that the deformation entering on the right-hand side is the elastic deformation, the difference between the total deformation and the plastic deformation

$$\Delta\sigma_{ij} = \mathbb{C}^e_{ijkl}(\varepsilon_{kl} - \varepsilon_{kl}{}^p) - \alpha\delta_{ij}\,\Delta P, \qquad (4.12)$$

the latter being denoted $\varepsilon_{kl}{}^p$. This plastic deformation at a given time t through the production history is

$$\varepsilon_{ij}{}^p = \int_0^t \dot{\gamma}^p M_{ij} dt', \qquad (4.13)$$

in which M defines the flow direction, function of the current stress state and $\dot{\gamma}^p$ is the equivalent plastic strain rate obtained from the viscosity law

$$\dot{\gamma}^p = \Gamma\big(\sigma_{ij} + P\delta_{ij}, \gamma^p\big), \qquad (4.14)$$

Γ defining a generic function of its argument. It should be stressed that the viscosity function and the flow directions are based on the Terzaghi effective stress defined as the sum of the initial stress plus the stress change and plus the current fluid pressure. This simple, single internal variable approach (γ^p) is sufficient to capture the structure of the constitutive relations which is now presented as

$$\Delta\sigma_{ij} = \mathbb{C}^e_{ijkl}\varepsilon_{kl} - \alpha\delta_{ij}\Delta P - \Delta\sigma_{C_{ij}}$$
$$\text{with } \Delta\sigma_{C_{ij}} = \mathbb{C}^e_{ijkl}\varepsilon_{kl}{}^p \qquad (4.15)$$

4.2.2.4.
Heterogeneous elasticity

The last element of this section is a proposal to account for deviations from the elasticity properties considered for the Green's functions. These properties are represented by the tensor $\mathbb{C}^e_{ijkl}$. The elasticity properties at point x_i in the domain are given by the tensor $\mathbb{C}_{ijkl}(x_i)$ which is different from $\mathbb{C}^e_{ijkl}$. The poro-elasticity constitutive relations presented in (6) are then amended to take the same formalism as presented in (15) and (9)

$$\Delta\sigma_{ij} = \mathbb{C}^e_{ijkl}\varepsilon_{kl} - \alpha\delta_{ij}\Delta P - \Delta\sigma_{C_{ij}} \qquad (4.16)$$

$$\text{with } \Delta\sigma_{Cij} = \left(\mathbb{C}^e_{ijkl} - \mathbb{C}_{ijkl}(x_i)\right)\varepsilon_{kl}$$

In summary, we have proposed three linear or non-linear constitutive relations of interest with the same structure, a linear part, corresponding to equation (4.5) complemented by a non-linear stress correction either due to non-linear elasticity (equation (4.9)), plasticity (equation (4.15)), or deviation from the reference elastic properties (equation (4.16)).

4.2.3.
Reciprocity theorem extended to linear, heterogeneous porous media

Central to this work is the theorem of reciprocity which enables us to make use of the known solutions of auxiliary problems in linear poro-elasticity.

Consider two problems with the same material domain and definition of the boundary domain $\mathbb{C}^e_{ijkl}$, $\partial\Omega_t{}^T$ and $\partial\Omega_t{}^u$. Apply the mechanical equilibrium condition (4.4) to problem number 1 with the virtual field corresponding to the exact solution of problem number 2 and vice-versa:

$$\int_{\Omega_t} \Delta\sigma^{(1)}_{ij}\,\varepsilon^{(2)}_{ij}\,\mathrm{d}V = \int_{\partial\Omega_t} \Delta T^{(1)}_i\,u^{(2)}_i\,\mathrm{d}S + \int_{\Omega_t} f^{(1)}_i\,u^{(2)}_i\,\mathrm{d}V,$$

$$\int_{\Omega_t} \Delta\sigma^{(2)}_{ij}\,\varepsilon^{(1)}_{ij}\,\mathrm{d}V = \int_{\partial\Omega_t} \Delta T^{(2)}_i\,u^{(1)}_i\,\mathrm{d}S + \int_{\Omega_t} f^{(2)}_i\,u^{(1)}_i\,\mathrm{d}V.$$

$$(4.17)$$

in which the superscript denotes the problem number. Problem number 1 is the auxiliary problem and problem number 2 is the problem with an unknown solution. The stress change in problem number 1 is $\Delta\sigma^{(1)}_{ij}$ and is associated with a distributed force which is typically a point load within the domain or on the boundary. Only the former case is considered here ($\Delta T^{(1)}_i = 0$). This stress change is linked to the strain according to the poro-elasticity response (equations (4.5) and (4.6)) considering that there is no fluid pressure change ($\Delta P^{(1)} = 0$). Problem number 2 has the unknown stress field $\Delta\sigma^{(2)}_{ij}$ which is related to the strain field $\varepsilon^{(2)}_{ij}$ and the non-linear stress, as presented in subsection 4.2.2.3. There are no distributed forces $\Delta T^{(2)}_i$ for this second loading. Combine these constitutive relations and conditions into the equilibrium equations (4.17) and obtain

$$\int_{\Omega_t} \mathbb{C}^e_{ijkl}{}^{(1)} \varepsilon^{(1)}_{kl} \varepsilon^{(2)}_{ij} \, dV = \int_{\Omega_t} f^{(1)}_i u^{(2)}_i \, dV,$$

(4.18)

$$\int_{\Omega_t} \mathbb{C}^e_{ijkl}{}^{(2)} \varepsilon^{(2)}_{kl} \varepsilon^{(1)}_{ij} \, dV = \int_{\Omega_R} \alpha \Delta P^{(2)} \delta_{ij} \varepsilon^{(1)}_{ij} \, dV + \int_{\Omega_t} \Delta \sigma_{C\,ij}^{(2)} \varepsilon^{(1)}_{ij} \, dV$$

in view of the major symmetry of the fourth-order tensor $\mathbb{C}^e_{ijkl}$, the left-hand sides of the system (4.18) are equal and consequently

$$\int_{\Omega_t} f^{(1)}_i u^{(2)}_i \, dV = \int_{\Omega_R} \alpha \Delta P^{(2)} \delta_{ij} \varepsilon^{(1)}_{ij} \, dV + \int_{\Omega_t} \Delta \sigma_{C\,ij}^{(2)} \varepsilon^{(1)}_{ij} \, dV$$

(4.19)

It is assumed that this theorem is applicable to unbounded domain and to generalized forces (such as a Dirac delta) without any further justification. The interested reader is referred to Bonnet and Willey (2000) for further information. Consider such generalized force to be a point load P_{β_i} applied at the material point pointed by the vector X_i in Ω_t with β denoting one of the axis associated to the basis vector in e_i. This generalized force is defined by

$$\int_{\Omega_t} P_{\beta_i}(X_i) u^{(2)}_i(x_i) \, dV = u^{(2)}_i(X_i) e_{\beta_i},$$

(4.20)

thus, providing by convolution the displacement component of Problem number 2 in the direction β at point X_i. This result replaces the left-hand side of (19) which now reads

$$u_i(X_i) e_{\beta_i} = \int_{\Omega_R} \alpha \Delta P \Theta_\beta (x_i - X_i) \, dV + \int_{\Omega_t} \Delta \sigma_{C\,ij}(x_i) \varepsilon_{\beta_{ij}}(x_i - X_i) \, dV, \quad (4.21)$$

in which the superscript of Problem number 1 has been replaced by the direction β of the generalized force in subscript and the superscript of Problem number 2 has been suppressed since there is no risk of ambiguity.

4.2.4.
Numerical scheme

The final objective of this section is to present two possible numerical schemes to solve equation (4.21). It is assumed that the Green's function computational tool is available, and a data set composed first, of a spatial

discretization of the reservoir and most likely its close surroundings and second, of the pressure history during production, was provided by the reservoir engineers.

There are two ways to solve equation (4.21) which is implicit in terms of the displacement field for heterogeneous media and non-linear materials more generally. The first method consists in determining the linearized strain directly by computing the displacement gradient $\frac{\partial y}{\partial x}$ through a differentiation of the right-hand side of this equation. The task is certainly possible although care should be taken while taking the gradient of a singular field as pointed out by Bui (1978) after the first developments of the boundary integral approach to non-linear problems. The second method is certainly easier to apply and consists in introducing the spatial discretization used by the reservoir engineers, as illustrated in Figure 4.1 with part of a three-noded triangle mesh in 2D. Consider an isoparametric interpolation, as it is classically done in the finite-element literature, and the displacement will be determined at every node according to equation (4.21) which is thus enforced by the discrete collocation method (ATKINSON; FLORES, 1993). In the particular example of Figure 4.1, a linear interpolation is used to construct the displacement field over each three-noded triangle, and its gradient is then piecewise uniform. The non-linear stress will thus be uniform over each element as the fluid pressure change is likely to be chosen. Consequently, the β-component of the displacement at any node located at the generic point X_i in the discretized domain reads

$$
\begin{aligned}
u_i(X_i)\mathrm{e}_{\beta_i} = {} & \sum_{b=1}^{N_{\Omega_R}} \alpha^{(b)}\,\Delta\mathrm{P}^{(b)} \int_{\Omega_R^{(b)}} \Theta_\beta(x_i - X_i)\,\mathrm{d}V \\[2mm]
& + \sum_{b=1}^{N_{\Omega_t}} \Delta\sigma_{C_{ij}}{}^{(b)}(x_i) \int_{\Omega_t^{(b)}} \varepsilon_{\beta_{ij}}(x_i - X_i)\mathrm{d}V\,,
\end{aligned}
\tag{4.22}
$$

in which N_{Ω_R} and N_{Ω_t} are the number of triangular elements over the reservoir (discretized domain Ω_R) and the regions where non-linear deformation develops or elastic heterogeneities are accounted for (discretized domain Ω_t), respectively.
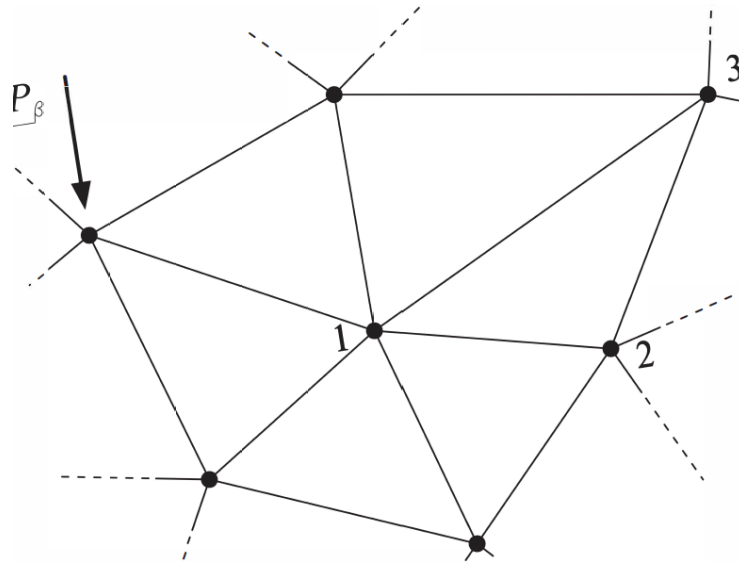
Figure 4.1 - A partial view on the 2D mesh, over the reservoir and the domain where non-linearities develop, composed of three-noded triangles. The 2D point load in direction β is applied at one of the node.

Three remarks to conclude this section. First, the volume change Θ_β within each element could be replaced by the displacement flux at the boundary by application of the divergence theorem. If the pressure change was uniform over the whole reservoir, it is on its boundary that the surface integral could be directly computed.

The second remark concerns the solution of the implicit equation (4.22) in which the non-linear stress is function of the current linearized strain. A fixed-point iterative method is proposed to integrate this non-linearity. At iteration $n + 1$, the displacement field at step n is used to construct the linearized strain and to update the non-linear stress term. The convergence criterion is based on the norm of the displacement field (square root of the sum of the squared nodal displacement components) over the discretized domain, which is the reservoir, plus where elasticity heterogeneities are found and plus where the non-linearities develop.

The third remark concerns the quadrature rule to estimate the two integrals in the right-hand side of equation (4.22). The example of the 2D point load in the β-direction of the infinite space is used to illustrate this comment which can be generalized to any auxiliary problem with a point load. The volumetric strain and the strain components are proportional to $\frac{1}{r}$ and to some trigonometric function $f(\theta)$ using the polar coordinate system (r, θ) defined for the β auxiliary solution. Some of the terms could be integrated exactly but a numerical quadrature appears to be

more convenient. If the point load is not at one of the node of the triangular element over which the quadrature is estimated, the simple quadrature proposed by Bartholomew (1959) is considered and is presented in Appendix B. The presence of the point load at one of the node renders the numerical scheme inaccurate and a Duffy's transformation is preferred (see Bonnet (2017) for a discussion and to Mousavi and Sukumar (2010) for a generalization to arbitrary singularity). The Duffy's transformation maps the triangular element to a rectangle over which the estimated function is not singular, and a classical Gaussian quadrature is then applied. Further information is found in Appendix B.

4.3.
Validation

Two convergence analyses are proposed, the first is the *h*-convergence to ensure that the exact solution is captured as the mesh size tends to zero. The second convergence concerns the iterative process to solve the implicit equation (4.22).

The model problem is a bi-layered cylinder embedded in an infinite medium. The core is of internal radius R while the outer shell is of external radius C, Figure 4.2. The outer layer is a proxy for the cap rock and is composed of a linear isotropic material of incompressibility K_C and shear modulus G_C. The initial pressure remains constant in the cap rock while the pressure changes by ΔP in the inner core. It corresponds to the reservoir and is composed of a non-linear porous material with constant shear modulus G_R and Biot coefficient α_R. The non-linearity is introduced via the incompressibility in the reservoir which is linearly related to the volumetric strain as presented in equation (4.10). The layered cylinder is within an infinite space composed of an isotropic, linear elastic material characterized by the moduli K_∞ and G_∞ and where the fluid pressure remains constant.

There is an analytical solution to this problem which is presented in Appendix C. The values selected for the numerical simulations are provided in Table 4.1. The meshes are created using the Delaunay triangulation algorithm implemented in the program Triangle (SHEWCHUK, 1996). The key factor for this validation step is the number of straight facets which are introduced to approximate the circular interfaces between the reservoir and the cap rock as well at the outer boundary of the cap rock. Further information on the mesh construction is found in the Electronic Supplement, Section C.

Table 4.1 – Material, geometrical and numerical data for the layered cylinder problem considered for validation.

Notation	Definition	Value/Range	Unit
C/R	Ratio Cap rock to reservoir radius	1.5	
Reservoir			
E_R	Elasticity modulus	10	GPa
ν_R	Poisson ration	0.2	
h_{k_R}	Hardening on incompressibility	-2020	
h_{G_R}	Hardening on shear modulus	0	
α_R	Biot coefficient	0.8	
ΔP	Fluid pressure change	-5	MPa
Cap rock			
E_C	Elasticity modulus	[5; 15]	GPa
ν_C	Poisson ration	0.2	
Infinite media			
E_∞	Elasticity modulus	10	GPa
ν_∞	Poisson ration	0.2	
Numerical scheme			
	Tolerance on displacement field	10^{-6}	
	Bartholomew level for quadrature	3	
	Gauss quadrature	3x3	
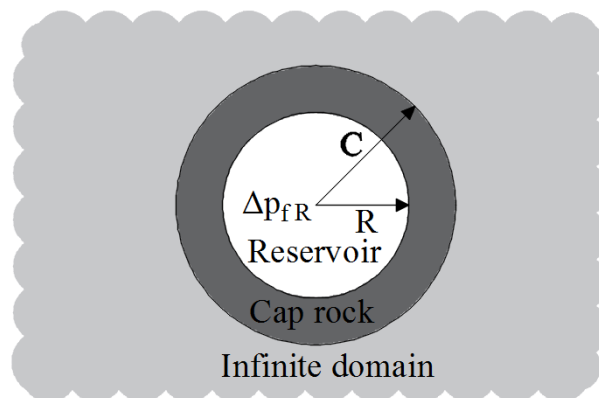
Figure 4.2. The geometry of the layered cylinder considered for the validation of the numerical algorithm

4.3.1.
h-convergence

The estimate of the error introduced by the spatial discretization is based on the norm of the displacement field

$$\frac{1}{V_{LC}} \int_{\Omega_{LC}} |u_i| \ dV \tag{4.25}$$

in which V_{LC} is the volume (area in 2D) of the layered cylinder. An exact value of this norm is computed from the analytical solution presented in Appendix C. It is the relative error, defined by the difference between the norm of the numerical solution and the norm of the analytical solution and normalized by the latter which is presented in Figure 4.3 as a function of the average element size. This element size is the average area of the elements divided by the area of the layered cylinder. For 50 facets, the error levels off at 0.15% for the fine meshes. One has to consider 200 facets at least to start to observe a convergence in the range of 10^{-4} which is sufficient for the class of engineering problems at hand. It is this number of facets which is chosen for the analysis of the convergence of the iterative algorithm reported next.

To illustrate the *h*-convergence, the radial displacements of the 2D predictions are plotted in Figure 4.4 in which the nodal displacements are presented with diamonds and the solid curves are the analytical solutions. The black curve corresponds to a linear, homogenous cylinder whereas the red and blue sets correspond to an increase and a decrease by 50% of the elasticity modulus in the cap rock, respectively, compared to the value for the infinite space. The green set corresponds to the simulation for the non-linear reservoir. In all cases, the difference between the analytical and the numerical solutions is negligible.
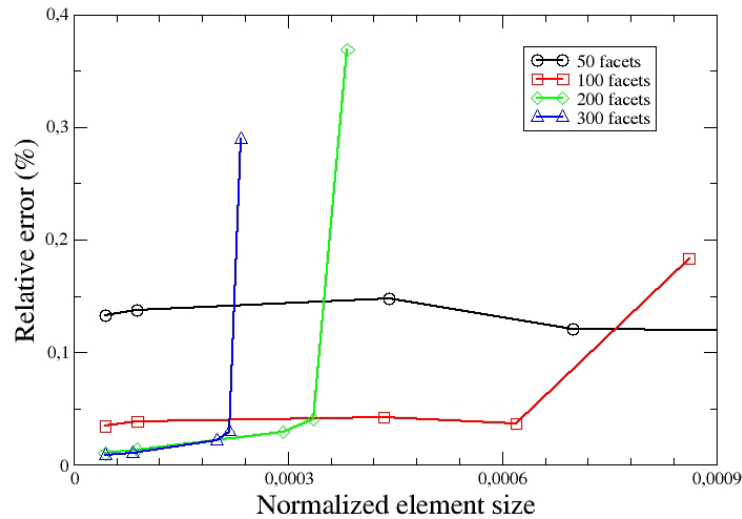
Figure 4.3. The relative error in displacement norm (in %) as function of the average element size for meshes composed of a different number of facets
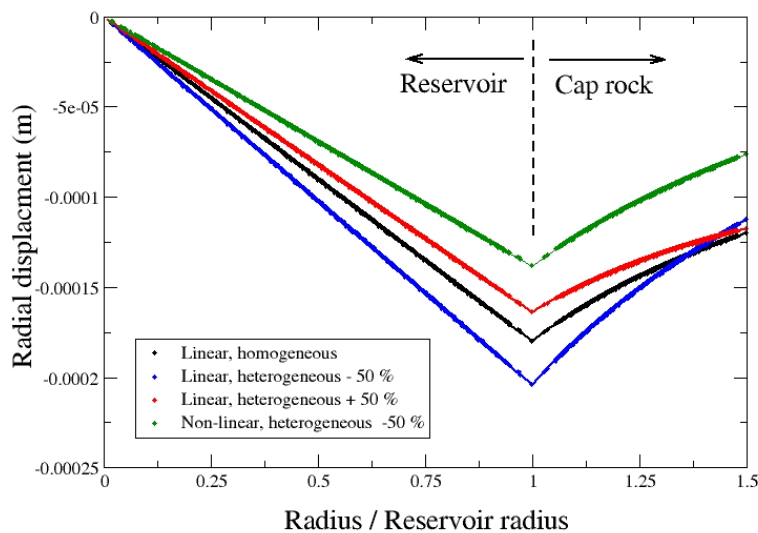
Figure 4.4. The radial displacement for the layered cylinder with a comparison of the numerical predictions (diamond symbol) and the analytical solution (solid lines). The elasticity modulus of the cap rock is varied by ±50 % compared to the value of the infinite space

4.3.2.
Iterative-convergence

This model problem is also interesting to check the rate of convergence of the iterative algorithm. Results are presented in Figure 4.5(a) in which the norm of the nodal displacement field DN, defined by the square root of the sum over the nodes of the displacement component square is plotted. This norm is normalized by the maximum value of DN which is obtained at the first iteration. The results show that the convergence is approximately linear with a slope which is decreasing in

magnitude as the elasticity contrast is increased. For example, the slope absolute value, which is referred to as the rate of convergence, is approximately 2 for 1% contrast (quadratic convergence) and drops to 0.4 for a contrast of -50 % (black triangles). These rates of convergence are plotted in Figure 4.5(b) as a function of the relative contrast in elasticity modulus. The convergence varies non-linearly from the quadratic rate to close to 0.1 for a contrast of 90%. The remarkable result is that convergence is achieved in all cases for a realistic range of physical parameters. This is certainly not a mathematical proof, but it provides some guidelines for applications.
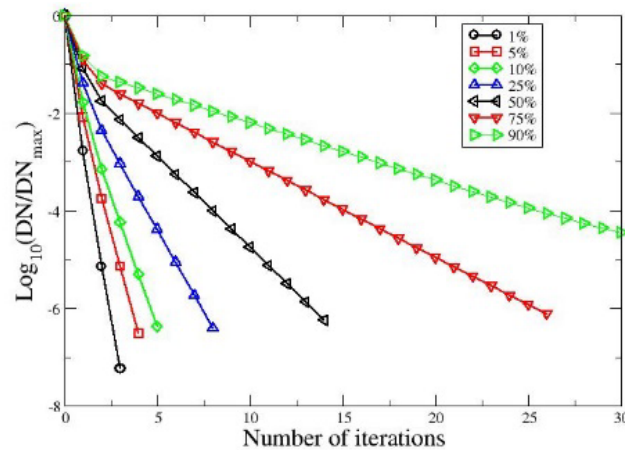
(a)
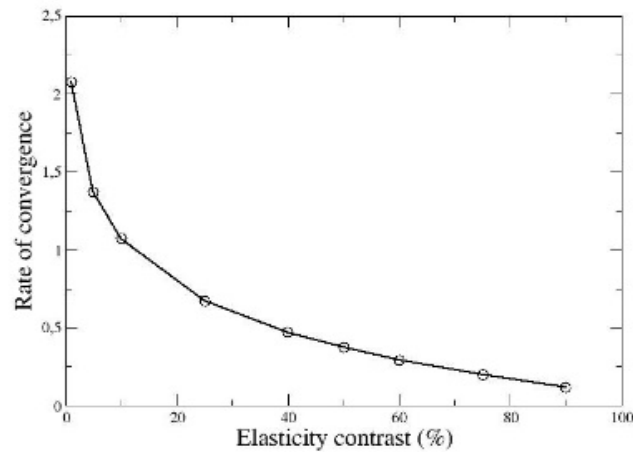
(b)

Figure 4.5. The displacement norm *DN* normalized by its maximum value as a function of the iteration number up to convergence for different contrasts in elasticity modulus in the cap rock compared to the one used for the Green's function, in (a). The rate of convergence (minus slope of curves in (a) of this iterative process as a function of the elasticity modulus contrast, in (b)
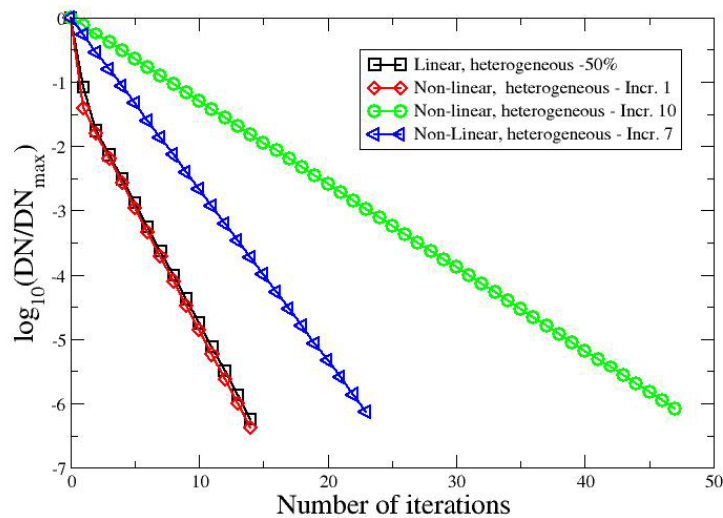
Figure 4.6. The normalized norm in the displacement field as functions of the iteration counter for linear heterogenous simulation (-50% in Elasticity modulus in the cap rock) and for the non-linear cap rock response considering the first, the seventh and the 10th increment of equal depletion of 5 MPa.

4.4.
Application: 4D effects in a depleting reservoir

The objective is to analyze the velocity changes of waves propagating within a gas reservoir sufficiently deeply buried for the application of the 2D Kelvin's Green's function to be justified. The reservoir is bounded by two listric faults forming a tilted blocks system, typical of an extensive geological setting. The lower reservoir boundary is the gas-water contact (GWC). The 2D prototype geometry, presented in Figure 4.7, occupies a rectangle having the dimensions of 2 by 1 km which is the computational domain. The quantity plotted in this graph is the relative change in elasticity modulus with respect to the one considered for the Green's function (zero difference within the reservoir). The overburden and the cap rock, corresponding to the light blue and dark blue layers just above the reservoir are more compliant than the reservoir by Atkinson and Flores (1993) and 50%, respectively. To the contrary, the substratum is stiffer than the reservoir by 50%. The mesh over the computational domain, composed of three-noded triangles, is constructed with the program Triangle (SHEWCHUK, 1996). The complete set of material, loading and numerical parameters is presented in Table 4.2.

Table 4.2 – Parameters for the tilted-block reservoir problem in Section 4. The reservoir in its initial conditions has the same properties as those used for the Green's function

Notation	Definition	Value/Range	Unit
Reservoir			
E_R	Elasticity modulus	10	GPa
ν_R	Poisson ration	0.2	
h_k	Hardening on incompressibility	-50	
h_G	Hardening on shear modulus	-50	
α_R	Biot coefficient	0.8	
ΔP	Fluid pressure change	-30	MPa
Cap rock			
E_C	Elasticity modulus	8	GPa
ν_C	Poisson ration	0.2	
Overburden			
E_O	Elasticity modulus	5	GPa
ν_O	Poisson ration	0.2	
Substratum			
E_S	Elasticity modulus	15	GPa
ν_S	Poisson ration	0.2	
Infinite media			
E_∞	Elasticity modulus	10	GPa
ν_∞	Poisson ration	0.2	
Numerical scheme			
R	Scalar for P-wave velocity change due to normal strain	-37.5	
R_θ	Scalar for P-wave velocity change due to volumetric strain	-37.5	
	Tolerance on displacement field	10^{-6}	
	Bartholomew level for quadrature	3	
	Gauss quadrature	3x3	
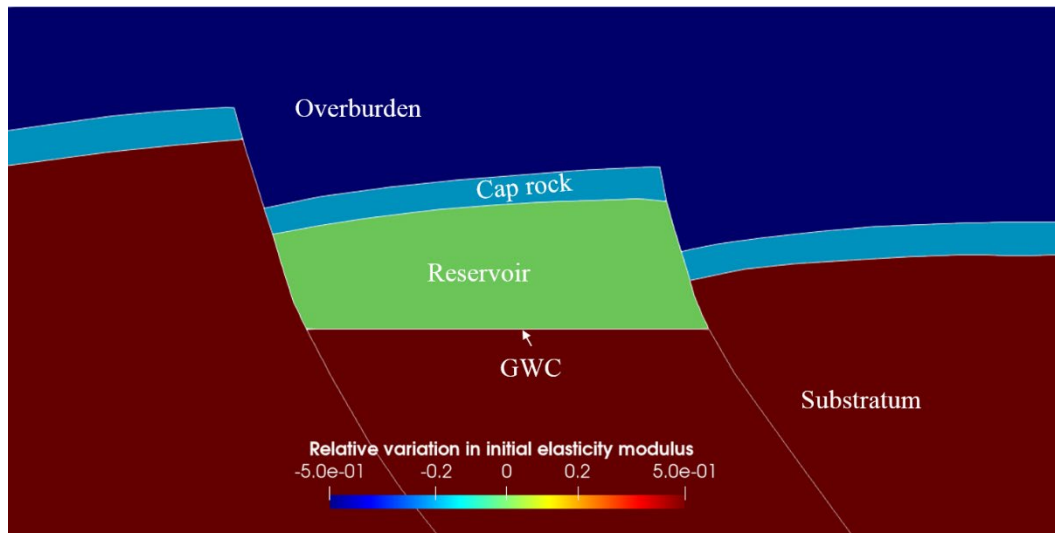
Figure 4.7. The gas reservoir in a system of tilted blocks. The reservoir has the same properties as those considered for the Green's function and the quantity plotted here corresponds to the deviation in elasticity from this reference value

The discussion of the results is started by considering the case of a homogenous linear elastic space since two features of the solutions are known. First, the volume change occurs only within the reservoir and is indeed zero outside1. The numerical procedure converges in a single iteration for this homogenous case. The results, not presented here for sake of conciseness, are in line with this first feature of the exact solution and the numerical volumetric change remains of the order at most 10^{-4} outside the reservoir, the larger values being attained close to its four corners. The second feature concerns these corners and Nowacki (2013) has shown, for a rectangular-shaped reservoir, that the shear component of the stress field is singular at these points ($\log r$ in which r is the distance to the corner). Such singularity is not captured by our three-noded, constant-strain element resulting in a numerical error which is classical in the Finite-Element literature.

The second set of results concerns the elastically heterogeneous prototype with the reservoir non-linear response. We first present the distribution in volumetric strain and in vertical strain, the two variables which controls the velocity changes for wave propagating vertically.

It is shown in Appendix C for the validation problem that the elasticity heterogeneity in the cap rock implies a local volume change which is proportional to the contrast in shear moduli with the one used for the infinite space. The volumetric strain is thus expected to be non-zero around the reservoir for the

heterogeneous prototype and is presented in Figure 4.8(a). The absolute values remain small around compared to within the reservoir despite the 20% contrast in elasticity modulus in the cap rock and ±50% in the substratum and overburden, respectively.

The vertical strain distribution is presented in Figure 4.8(b). It is compressive in the reservoir sides and extensive above it, as expected. This spatial variation is consistent with the geophysics observation above the reservoir which has steered a strong interest from the 4D geophysicists for the interpretation of 4D seismic surveys. Note that such spatial gradient does not show on the volumetric strain distribution.
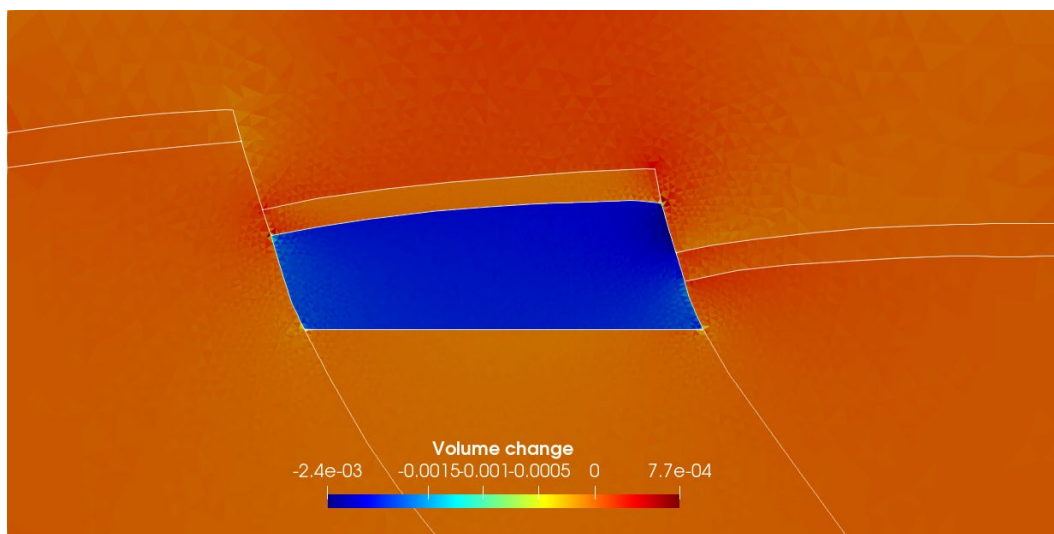
(a)
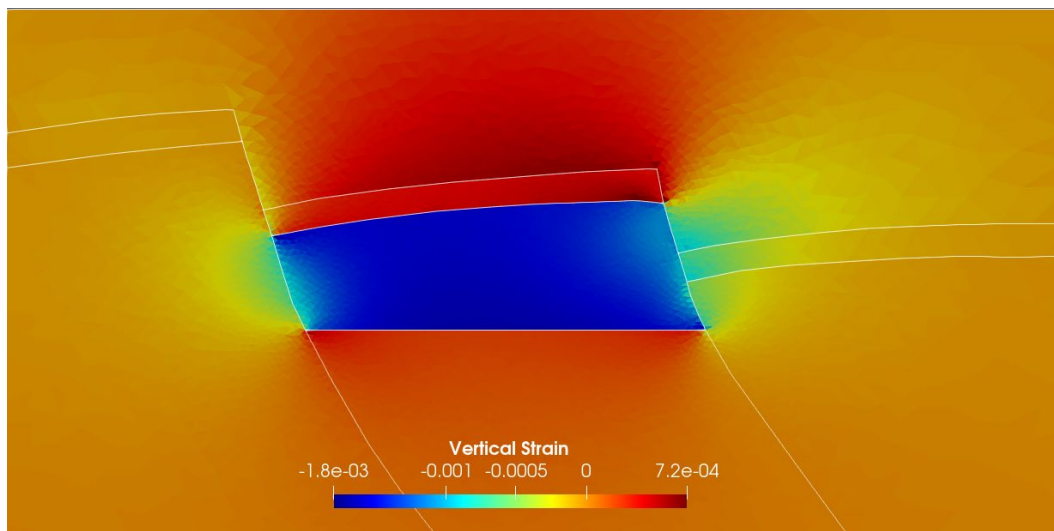
(b)

Figure 4.8. The volume change in (A) and the vertical strain in (B), following a depletion of 300 bars in the reservoir

Attention is finally turned to the velocity changes within the reservoir. Appendix D provides the complete derivation of the P and S wave velocity changes and the final result for P wave is found in Section 2.2.2 with equation (4.11). It is the sum of two terms, the first proportional to the volumetric strain with the constant $(1/2 + R\theta)$ and the second to the strain in the direction of propagation (referred to as the normal strain in what follows) with the constant R. These two scalars $R\theta$ and R are proportional to hK and hG, respectively. The two have the same value -37.5 for the material parameters in Table 4.2, meaning that the volume strain and the normal strain have the same weight on the P wave velocity changes. Note that the proportionality constant to the normal strain coincides with the classical R-factor proposed by Hatchell and Bourne (2005) for vertical propagation, although the value considered here is large compared to the one found in the literature.

Results concerning the relative velocity changes within the reservoir are presented in Figure 4.9 for the non-linear elasticity model in (a) and based solely on the R factor approach in (b). The ranges are not the same for the two plots since the velocity changes based only on the R factor is approximately half the complete velocity change. The distribution in velocity changes based only on the R-factor is simply a scaling of the vertical strain presented in Figure 4.8(b). The non-linear elasticity predictions combine the influence of the volume change and the vertical strain presented in this Figure 4.9(a). The comparison between the two approaches is further done in terms of position of maximum and gradient. The maximum is in the lower central part for the R-factor and within the central part for the complete approach. The vertical gradient along the two lateral boundaries is also interesting. They differ because of the contrast in elasticity in the surrounding rock.
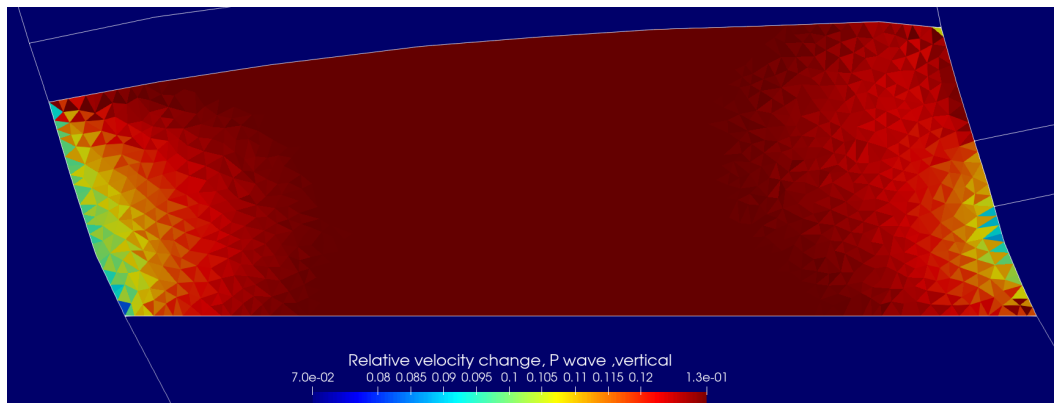
(a)
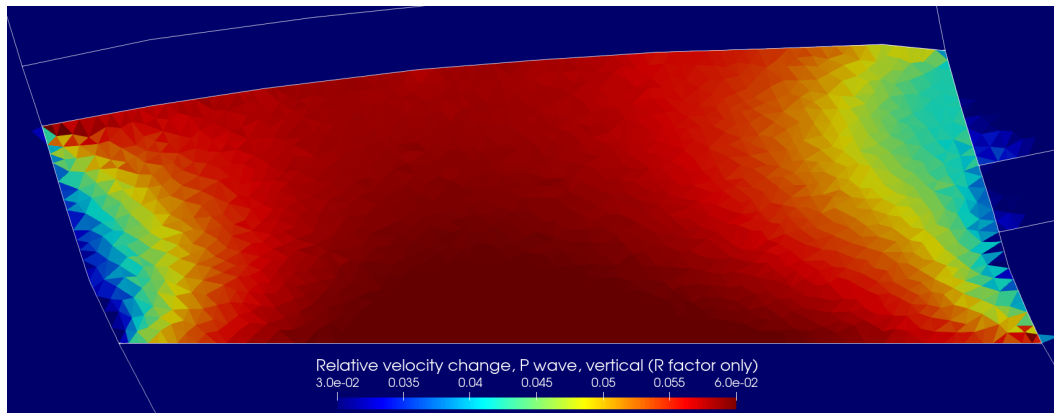
(b)
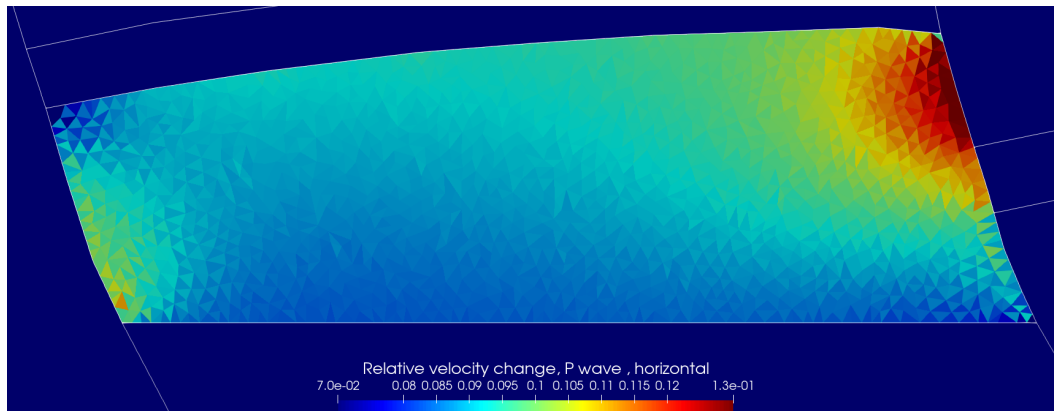
(c)

Figure 4.9. The relative velocity changes based on the variation in the elasticity properties in (a) and solely on the R factor approach in (b) for a vertical propagation. The relative velocity change for waves propagating horizontally in (c). Zoom on the reservoir

A final point to discuss is the anisotropy in the P-wave velocity changes. It is proposed to examine the relative velocity change for a wave traveling horizontally, Figure 9C. The distribution is over the same range as for the vertically propagating wave presented in Figure 9A. The two distributions share the same contribution of the volumetric strain through the $R\theta$ factor but the contribution of the normal strain is different. For the horizontal propagation, the normal strain is the horizontal strain which for an infinitely long reservoir is zero (oedometric conditions). In our example, the horizontal strain is of the order of one tenth of the vertical strain. The maximum in relative velocity change for the horizontal propagation is at the upper part of the right boundary where the surrounding rock is the softer. The non-linear elasticity model proposed here, despite its isotropic properties, has thus the merits to pick-up the wave anisotropy which is due to the structural response (field scale) and not to the material response.

4.5.
Conclusion

This contribution reports on a feasibility study to use classical Green's functions as auxiliary solutions to capture the evolution of the stress state in elastically heterogeneous and non-linear fluid-saturated porous media, typically a fluid reservoir and its close surroundings. The non-linearity could be due to irreversible deformations such as compaction or to the non-linear elasticity properties to produce 4D predictions, as it is illustrated here.

It is shown that the Green's functions for homogenous media (Kelvin for infinite space and Mindlin for half-spaces) thanks to the reciprocity theorem could indeed be used to capture such non-linear stress evolutions through an iterative approach. At each step a Maysel's type integral equation is solved. It requires first to estimate the stress difference between the stress based on the elasticity properties considered for the Green's function and the actual stress resulting from the elasticity heterogeneities, the non-linear material response and the fluid pressure change. Second, the work done by this stress difference on the conjugate strain of the auxiliary problem is then estimated in a convolution integral to find the displacement at any point where the point load of the auxiliary problem is applied.

A spatial discretization of the domain where the non-linearities develops, where the elasticity deviates from the reference value and where the fluid pressure is changing is required for constructing this Maysel's type integral equation. It is based on constant strain, three-noded triangles for the 2D examples considered in this contribution. The quadrature over each triangle is classical if the point load is not applied at one of its three nodes. If it is the case, a Duffy's transformation is considered to eliminate the singularity and a classical Gauss quadrature is sufficient on the transformed domain. During the iterative process, the displacement at iteration k is used to update the stress difference and the convolution provides the nodal displacements at iteration $k + 1$. Convergence is based on the norm of the displacement field over the computational domain.

The numerical scheme is validated by comparing the predictions with an analytical solution for a bi-layered cylinder embedded in an infinite space in 2D. The non-linearities are in the core and the deviation from the Green's function elasticity properties in the outer layer. It is shown that the convergence in terms of

mesh-size is achieved with a strong influence of the number of straight facets considered to approximate the boundaries between the two cylindrical layers and the outer space. It is also shown that the convergence of the iterative process is very sensitive to the young modulus contrast from the Green's function value. The convergence is close to quadratic in displacement norm for a few percent of contrast and degenerates to sub-linear for elasticity contrast greater than 15%. Convergence is still achieved for larger contrasts (up to 90% tested) but at the low rate of 0.1. Although the convergence results presented here do not constitute a mathematical proof, they provide guidelines for applications.

The numerical scheme is then applied to a depleting gas reservoir in a tilted blocks system with a contrast in elasticity modulus of up to -50% in the overburden and +50% in the substratum. The non-linearities develops within the depleting reservoir by application of a non-linear elasticity response in which the incompressibility and the shear modulus are function of the volumetric strain. It is shown, from a thorough analysis of the acoustic tensor, that the wave velocity changes are sensitive to the volume change as well as to the strain in the propagation direction (referred to as the normal strain). Considering a vertical propagation, the velocity changes within the reservoir are thus not reproduced by a classical R-factor approach and requires to account for the influence of the volumetric strain. The exact weights of the two deformation features on the velocity changes are linked to the material properties and need to be estimated from laboratory data or from the inversion of the seismic surveys considered for 4D studies as in 19. Note that despite the selection of an isotropic elasticity model in its reference configuration, it is shown that because of the normal strain dependence, the relative P-wave velocity change is anisotropic.

The main merit of the proposed approach is that the mesh construction is limited to the reservoirs and to the regions of interest where rock properties are hopefully available. The main disadvantage compared to a classical finite-element approach is that an iterative solution is constructed even for a purely elastic response which becomes CPU-intensive for 3D problems. The computational cost for a single iteration is of the order of the number of degrees of freedom time the total number of quadrature points. For 2D, constant strain elements, this number can be reduced significantly since the quadrature can be done analytically, as reported by Nintcheu Fata (2011). Such improvement may not be applicable for

isochoric plastic deformation since higher-order elements will be necessary to avoid mesh locking and the strain will not be uniform over the element. The difficulty thus remains especially for 3D problems. as in various branches of physics dealing with many particles' interactions. Improvements have come with the multipole method (FU et al., 1998; GREENGARD; ROKHLIN, 1997) requiring iterative computations. The question is then whether to invest in such sophisticated approach or to rely more on a more systematic development of parallel computation based, for example, on GPU.

Future developments on the proposed approach thus include a parallelization effort for application to 3D setting. The case of pre-salt carbonate reservoirs is of interest and the use of Mindlin's Green's function for the half-space will be required. The development of micro-structurally based elasticity constitutive relations to replace the phenomenological non-linear model considered here should be considered especially for 4D analysis within the overburden since the volumetric strain remains there low despite the elasticity heterogeneities. The micro-structural approach is well established for laboratory experiments (FORTIN; GUÉGUEN; SCHUBNEL, 2007; SAYERS; KACHANOV, 1995) and has been considered for applications at the field scale although the interpretation of the micro-crack defects is debated. Finally, a comparison with an industrial finite-element code such as Abaqus would also be of interest to establish in greater details the pros and cons of the proposed approach.

5
"Intelligent element: Coupling Green function approach and artificial intelligence to reduce discretization effort"

Paper published by Matheus L. Peres, Elisa D. Sotelino, and Leonardo C. Mesquita in the International Journal for Numerical and Analytical Methods in Geomechanics[2].

Abstract

This research work presents a method that modifies a classical numerical method using artificial intelligence and takes advantage of an analytical method to minimize the usual need for increasing discretization. Its formulation is based on the integration of two main concepts: the reciprocity theorem and the generalization capability of artificial neural networks. The reciprocity theorem is used to formulate the mathematical expression governing the geomechanical problem, which is then discretized in space into intelligent elements. The behavior of the strain field inside these new elements are predicted using an artificial neural network. To make these predictions, the neural network uses displacement boundary conditions, material properties and the geometric shape of the element as input data. The comparison was performed for two examples, in which the first had a uniform depletion of the reservoir, while the second had a non-uniform variation of the pore pressure. For the same level of accuracy, the proposed method was ten times faster than the traditional method for the first example and five times faster for the second example on a computer with 12 threads of 2,6GHz and 32GB RAM.

5.1.
Introduction

The extraction or injection of fluids in a rock mass generates a pore pressure variation in the porous medium that impacts the mechanical behavior of the entire

---

massif. Some of the main changes caused due to pore pressure variation that deserve attention are the compaction of the reservoir, which affects the permeability of the rock, reducing the fluid extraction rate (GAMAGE et al., 2011; OSTENSEN, 1986; VAIROGS J et al., 1971) and, possibly, closing the well (BRUNO, 1992; YUDOVICH; CHIN; MORGAN, 1988); the subsidence or lifting of the free surface which can affect the functionality and stability of structures present in the region (FIGUEROA-MIRANDA et al., 2018). In addition, the monitoring of the massif behavior during the production of hydrocarbons is done through seismic measurements (BARKVED et al., 2005; HATCHELL et al., 2007; HERWANGER; HORNE, 2009; TEMPONE; LANDRØ; FJÆR, 2012), which relate to the variation of the strain field and to the variation of pore pressure in the reservoir to make predictions regarding the state of the massive.

The predictions of the massif behavior due to pore pressure variation can be made in two different ways: using analytical models or using numerical models. One of the first analytical models for subsidence prediction was developed by (GEERTSMA, 1957, 1966, 1973b, 1973a) based on the nuclei of strain principle introduced by (MINDLIN; CHENG, 1950a, 1950b). The model proposed by Geertsma can predict the subsidence caused by the depletion of a cylindrical reservoir embedded in a semi-infinite medium of linear elastic material.

Opstal (OPSTAL, 1974) expanded Geertsma's model for calculating the subsidence caused by a reservoir embedded in a semi-infinite medium with a rigid base. In practical terms, the rigid base can be the simplification of a layer of crystalline rocks or rigid carbonates. Tempone (TEMPONE; FJÆR; LANDRØ, 2010) expanded the Opstal model to obtain the displacement and strain fields throughout the massif. (SEGALL, 1992) based on Geertsma's research, developed an analytical model to analyze the strains and stresses around a reservoir of any axisymmetric shape subjected to axisymmetric pore pressure variation. (SOLTANZADEH; HAWKES, 2008) used the inclusion theory proposed by (ESHELBY, 1957, 1959, 1961) to simulate 2D models with elliptical or rectangular cross-section reservoirs. Also, in terms of geometry generalization, without the need for axisymmetry, Muñoz (MUÑOZ; ROEHL, 2017) proposed a formulation applicable to 3D reservoirs of any geometry and observed that when analyzing the problem three-dimensionally, the integration of singular functions is eliminated. All three models presented in (MUÑOZ; ROEHL, 2017; SEGALL, 1992;

SOLTANZADEH; HAWKES, 2008) simplified the problem by considering the reservoir embedded in a linear elastic homogeneous semi-infinite medium. Du (DU; OLSON, 2001), Mehrabian (MEHRABIAN; ABOUSLEIMAN, 2015), Wangen (WANGEN; HALVORSEN, 2019) developed analytical models for the analysis of displacement and strain fields in a massif with three layers of different materials. In these works, the perturbation in the massif was caused by the axisymmetric variation of pore pressure in a cylindrical reservoir. Furthermore, Mehrabian (MEHRABIAN; ABOUSLEIMAN, 2015) showed that their model can be expanded to a stratigraphy with any number of layers. Also aiming to build a more generic model in relation to the stratigraphy of the massif, Fokker (FOKKER; ORLIC, 2006) presented a semi-analytical model capable of considering multiple viscoelastic layers.

Numerical methods, in addition to allowing the simulation of models of the most varied geometries and constitutive models, allow the consideration of flow simulations coupled to geomechanical simulations. Most numerical simulations are performed using the finite element method (FEM) (ALTMANN et al., 2010; GAMBOLATI et al., 2001; KOSLOFF; SCOTT; SCRANTON, 1980a; ZHOU; VOYIADJIS, 2019), because it makes possible to consider different types of nonlinearities, such as plasticity (KOSLOFF; SCOTT; SCRANTON, 1980b; NIU; LI; WEI, 2017), viscosity (CHANG; MAILMAN; ZOBACK, 2014; VOYIADJIS; ZHOU, 2018), fracturing (WANGEN, 2013) and fault reactivation (LESUEUR; POULET; VEVEAKIS, 2020). However, the representation of boundary conditions is always a challenge, mainly due to the difficulty in modeling semi-infinite medium condition using precise elements. Numerical methods are able to better represent form and materials compared to analytical and semi-analytical methods. This is due to their generic formulations that provide adaptability to any mechanical problem. In contrast, these numerical methods require more time for modeling and processing compared to analytical and semi-analytical. An alternative to simplify the modeling in numerical simulations is the formulation of methods that consider particularities of the addressed problem, but which are not necessarily applicable to any other problem. Furthermore, these methods must be generic enough to represent the geometry, materials, and boundary conditions of real reservoir geomechanics problems. Thus, the efforts to develop numerical solutions must seek a balance between specificity and generality.

The present work proposes a numerical method for the calculation of displacement, strain, and stress fields in compliance with the idea of balancing specificity and generality. The proposed method is based on the application of artificial neural networks (ANN) to a mathematical formulation based on the principle of reciprocity of Green functions. The ANN associated with this mathematical formulation is named intelligent elements in this work. These intelligent elements are developed to be general enough for reservoir geomechanics problems and, consequently, demand coarsely refined mesh only over the region of interest in comparison with traditional elements such as finite element which require finely refined meshes over a very large domain away from the region of interest. Thus, the size of the problem can lead to prohibitive computational times and large storage requirements. The proposed method avoids both limitations, reduces CPU time and requires less storage.

5.2.
Systematic Literature Review

The Systematic Literature Review (SLR) was carried out in three stages: formulation of the question, location of articles and analysis of results. Thus, it was defined that the question would be: "How does the integration between machine learning and numerical methods for geomechanical simulations occur?". Through the selection of articles that brought answers about this question, the state of the art in this area was verified, which lead to the path that this research followed. Figure 5.1 shows a block diagram of the SLR.

The databases used in the SLR were Scopus, Web of Science, and Engineering Village. No exclusions were made based on the year of publication. By using this combination, the search found papers that study the training of neural networks to perform inverse analysis (SOUZA; ROEHL, 2019; ZHANG et al., 2020a, 2020b), which uses in loco measurements to build meta models for the massive (ALBAHRANI; PAPAMICHOS; MORITA, 2021; BOBET, 2010; DEO, 2010; TANDON, 2019; VASILYEVA et al., 2021; ZHANG et al., 2014, 2016). In these works, neural networks are used to build constitutive models based on laboratory tests (ALERIGI; BATARSEH; ASSIRI, 2020; HEIDER; SUH; SUN, 2021). Only one research work was found that proposes a numerical method based on machine learning (ZHAO, 2021). In this work, a model reduction is proposed to

predict displacements and stresses combining "proper orthogonal decomposition" (POD) and "multi-output support vector machine" (MSVM). To achieve this, it is necessary to generate finite element models with different properties (elasticity modulus, Poisson's ratio, initial stresses) and their respective orthogonal decomposition. Then the MSVM algorithm generates a relationship between the coefficients of the POD vectors and the properties of the model under study. Thus, this method requires that for each new model of different geometry the entire procedure be performed again.
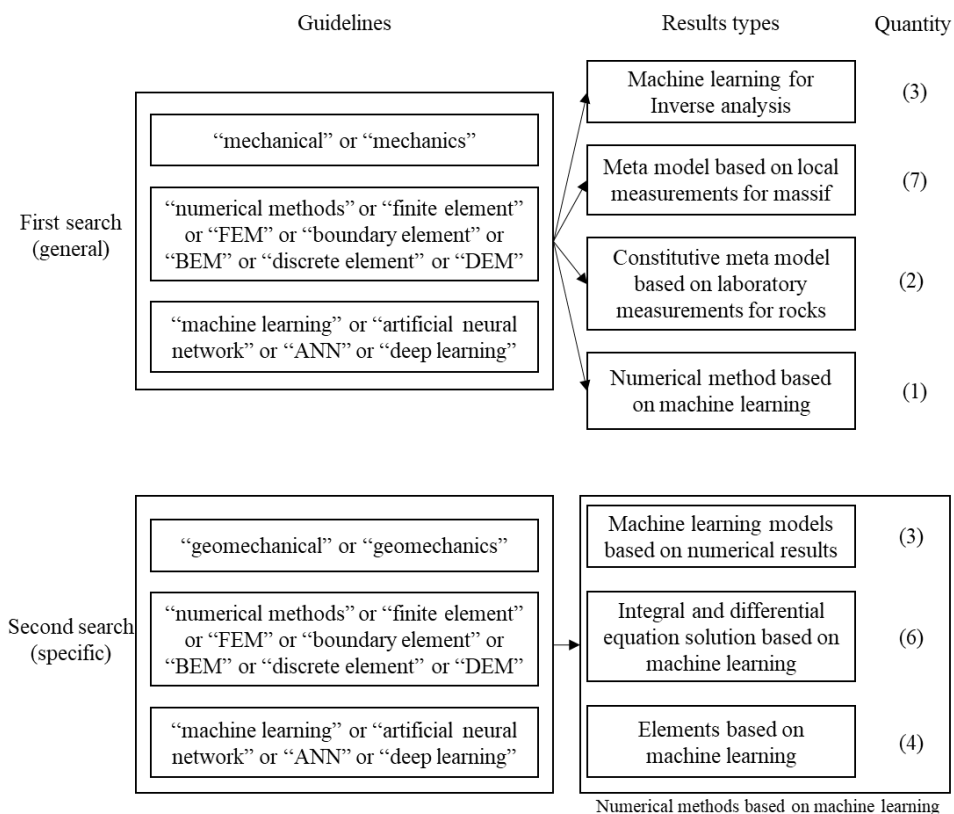
Figure 5.1. SLR block diagram

Therefore, a knowledge gap was identified regarding the integration between machine learning and numerical methods applied to geomechanics. It was verified gap also exists for the simulation of other mechanical problem in a second search. This search for papers generated around two thousand papers, indicating that machine learning has been applied in some way along with numerical methods to solve mechanical problems. Each of these works had at least the title read to filter the works that studied the integration between the two areas and not just applied the two methods together. During the filtering process, three main areas were identified

in which artificial intelligence and numerical methods were integrated: biomechanics, modeling of constitutive properties and monitoring of the structural safety of bridges. However, only thirteen papers used artificial intelligence to modify or create numerical methods. These thirteen filtered papers can be classified into three groups.

The research of the first group used results of numerical methods to train a neural network, which were used to obtain answers with a shorter processing time. More specifically, the neural networks were used to provide the answer of micromodels (GHAVAMIAN; SIMONE, 2019), to relate surface forces applied to a body of any geometry to the generated displacement field (MENDIZABAL; MÁRQUEZ-NEILA; COTIN, 2020), and to determine the von-Mises stress in the aorta from medical examination images (LIANG et al., 2018).

The second group of the filtered articles is composed of research works that used artificial neural networks to solve differential or integral equations. Samaniego (SAMANIEGO et al., 2020) and Nguyen-Thanh (NGUYEN-THANH; ZHUANG; RABCZUK, 2020) used the concept of minimum potential energy as the objective function to train a neural network capable of predicting the displacement of a given body subjected to external forces. Lin (LIN; ZHOU; GUO, 2020) and Nabian (NABIAN; MEIDANI, 2019) proposed the use of the partial differential equation for heat transfer as an objective function for training a neural network. Huang (HUANG; WANG; YANG, 2020) proposed the solution of low order nonlinear partial differential equations in two phases. In the first phase, a neural network is trained, using the PDE that governs the problem as an objective function to obtain an initial result. In the second phase, there would be an iterative process whose initial solution would be the result obtained in the first phase. Finally, Brevis (BREVIS; MUGA; VAN DER ZEE, 2020) coupled an artificial neural network model to the weighted residuals method to solve PDEs.

The third set of works found after the filtering process groups articles that worked on the development of elements based on neural networks. Capuano (CAPUANO; RIMOLI, 2019) developed a method in which machine learning algorithms and the finite element method are used together to solve nonlinear mechanical problems through a stiffness matrix obtained by numerical differentiation of nodal forces calculated by the artificial intelligence (AI). Koeppe (KOEPPE; BAMER; MARKERT, 2020) also proposed a method in which the

stiffness matrix of an element with a specific material would be calculated from the nodal forces which in turn would obtain through a convolutional recurrent neural network whose input data would be the nodal displacements. Jung (JUNG; YOON; LEE, 2020) suggested that the matrix terms relating the nodal displacements to the strains within a linear elastic quadrilateral element should be provided by a neural network. And at last, Liu (LIU, 2020) proposed the use of artificial neural networks as a shape function in finite elements.

It can be concluded that group one presents solutions with a higher computational performance gain than the solutions presented by the other research works, but the situations in which these solutions can be applied are more specific. On the other hand, the solutions presented in set two are applicable to any differential or integral equation, but their computational cost is high. Finally, the research works in the third set are between the other two groups in terms of generalization and computational performance. For this reason, through the structured literature review it is identified that the use of applied artificial intelligence is an efficient way of modifying numerical methods to obtain computational gain while still solving more general problems.

5.3.
Intelligent element based on Green's function approach

5.3.1.
Formulation

The formulation of the intelligent element method is the combination of the method based on Green functions with the generalization capability of artificial neural networks. The Green function method, presented by (PERES et al., 2021), consists of applying the principle of reciprocity to a pair of geomechanical systems, the first system is characterized by a classical problem that has an analytical solution (Green Function) and the second is the problem to be solved. For the sake of illustration, without loss of generality, consider as the classical problem the case of a force applied in a linear elastic semi-infinite medium (whose Green function was presented by (TELLES; BREBBIA, 1981) and based on is shown in Appendix A) and as the desired problem a geomechanical reservoir being depleted, located in a stratified zone embedded in a semi-infinite medium (Figure 5.2). The application

of the reciprocity theorem results in equation (5.1) for the continuous media. In this work, the variables with superscript "*" are related to the auxiliary problem.
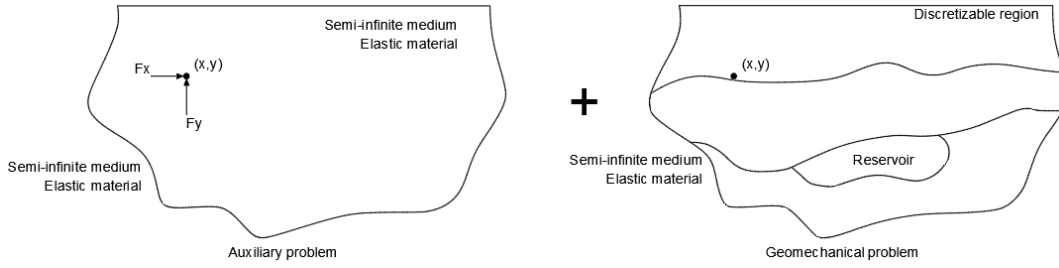
Figure 5.2. Combining auxiliary problem with reservoir geomechanics.

$$u_k(X_i) = \int_R \alpha(x_i)\Delta P(x_i)\delta_{mn}\varepsilon_{mnk}{}^*(x_i, X_i)\, dV$$

$$+ \int_C \left(C_{mnjl}{}^* - C_{mnjl}(x_i)\right)\varepsilon_{jl}(x_i)\varepsilon_{mnk}{}^*(x_i, X_i)\, dV,$$

(5.1)

where $C_{mnjl}{}^*$ is the constitutive tensor of semi-infinite medium, $u_k(X_i)$ is the displacement vector at position X_i, $\alpha(x_i)$, $\Delta P(x_i)$, $C_{mnjl}(x_i)$ and $\varepsilon_{jl}(x_i)$ are, respectively, the Biot coefficient, the pore pressure variation, the constitutive tensor, and the strain variation tensor at position x_i of the real problem. δ_{mn} and $\varepsilon_{mnk}{}^*(x_i, X_i)$ are, respectively, the Kronecker delta and the strains at the position X_i due to a point load with direction k applied at x_i. Furthermore, the domain R represents the region of the model where there is pore pressure variation and the domain C symbolizes the stratified region where the reservoir is located, referred to in this work as a complementary region.

The continuous problem can be discretized into nR elements in the reservoir region and nC elements in the complementary region, resulting in equation (5.2).

$$u_k(X_i) = \sum_{p=1}^{nR} \int_{RE_p} \alpha(x_i)\Delta P(x_i)\delta_{mn}\varepsilon_{mnk}{}^*(x_i, X_i)dV$$

$$+ \sum_{q=1}^{nC} \int_{CE_q} \left(C_{mnjl}{}^* - C_{mnjl}(x_i)\right)\varepsilon_{jl}(x_i)\varepsilon_{mnk}{}^*(x_i, X_i)\, dV$$

(5.2)

Since the information on the pore pressure variation is usually provided by flow models, solved using discrete numerical methods, it is realistic to consider that the pore pressure and the Biot coefficient are uniform in each element.

$$u_k(X_i) = \sum_{p=1}^{nR} \alpha(x_i) \Delta P(x_i) \int_{RE_p} \delta_{mn} \varepsilon_{mnk}{}^*(x_i, X_i) dV$$

$$+ \sum_{q=1}^{nC} \int_{CE_k} \left(C_{mnjl}{}^* - C_{mnjl}(x_i) \right) \varepsilon_{jl}(x_i) \varepsilon_{mnk}{}^*(x_i, X_i) \, dV \tag{5.3}$$

As $\varepsilon_{jl}(x_i)$ is defined by $\frac{1}{2}\left(u_{j,l}(x_i) + u_{l,j}(x_i)\right)$, it is possible to use a collocation method (ATKINSON; FLORES, 1993) to solve the problem at all nodes of the discretized model. To do that, equation (5.3) can be rewritten in a recurrence form as shown in equation (5.4), where the initial solution, $u_k(X_i)^0$, is given by equation (5.5). The discretization used for the initial solution can be the same used for flow simulation and the region of integration for the second term can be discretized in intelligent elements.

$$u_k(X_i)^{r+1} = u_k(X_i)^0 + \sum_{q=1}^{nC} \int_{CE_k} \left(C_{mnjl}{}^* - C_{mnjl}(x_i) \right) \varepsilon_{jl}(x_i)^r \varepsilon_{mnk}{}^*(x_i, X_i) \, dV, \tag{5.4}$$

$$u_k(X_i)^0 = \sum_{p=1}^{nR} \alpha(x_i) \Delta P(x_i) \int_{RE_p} \delta_{mn} \varepsilon_{mnk}{}^*(x_i, X_i) dV, \tag{5.5}$$

with the upper script r denotating the iteration.

5.3.2.
The intelligent element

As the computational effort in discrete methods is directly related to mesh refinement, the use of an element that can reach convergence with a less refined mesh could reduce the time spent in the simulations. It is with this objective that this work proposes the development of elements based on an artificial neural network. The development of intelligent elements is based on the idea of replacing a triangular region of a refined mesh with a single super element with 9 nodes, as seen in Figure 5.3. The AB side of the element illustrated in Figure 5.3 will always be used to denote the longest side of the element.

An intelligent element uses as input data the coordinates of the nodes, the nodal displacements, the coordinate of the internal evaluation point, and the Poisson's ratio, and as output data the strain field at the evaluation position. The

element processes the input data and then uses a feedforward multilayer perceptron neural network to obtain the strain field in local coordinates normalized by the maximum nodal displacement.
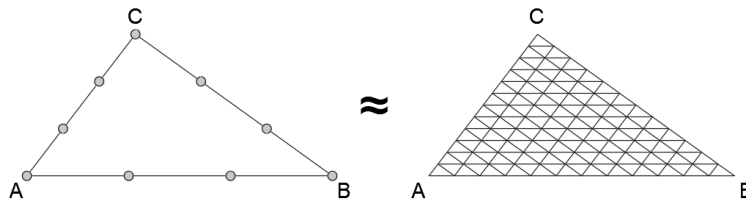
Figure 5.3. Replacing a refined triangular region with an intelligent element.

The concept of an artificial neural network is based on how the human nervous system processes information. Likewise, the basic processing unit, or artificial neuron, that makes up an ANN is based on the biological neuron. These artificial neurons are organized in layers, forming the artificial neural network, which in the present work is composed of an input layer, two hidden layers and an output layer (Figure 5.4a).

The artificial neuron, like a biological neuron, has elements for capturing and transmitting impulses (information) and an element for processing the received information. These two regions are indicated in Figure 5.4b by the colors blue and red, respectively.
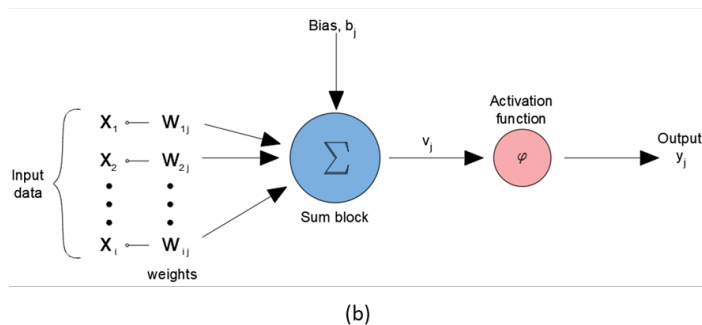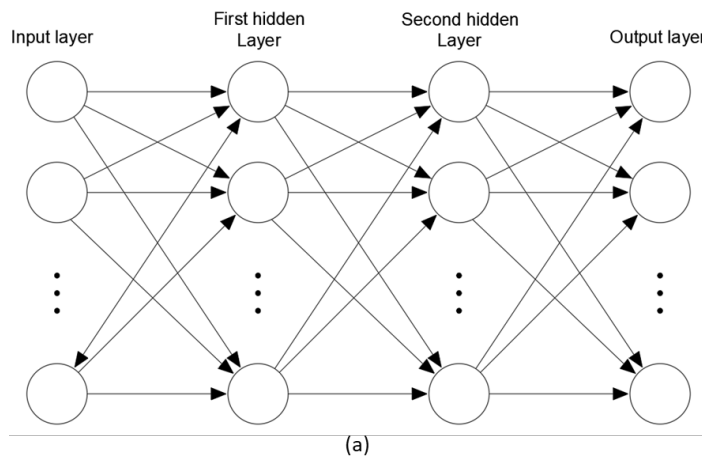
Figure 5.4. (a) Artificial Neural Network. (b) Artificial Neuron.

Mathematically, an artificial neuron can be understood as a composite function, given by equation (5.6):
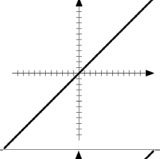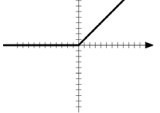
$$y_j = \varphi\left(v_j(x_i)\right), \tag{5.6}$$

in which y_j is the answer or the output of neuron j, $\varphi(v_j)$ is named activation function and $v_j(x_i)$ is the sum presented in equation (5.7), in which x_i are the are the input of the neuron, n is the number of impulses received, w_{ij} is the weight which multiplies the input x_i received by neuron j, and b_j is the bias of neuron j.

$$v_j = \sum_{j=0}^{n} w_{ij} x_i + b_j, \tag{5.7}$$

Activation functions have the role of determining the amplitude of the output value and can be of several types, depending on the problem in which the network will be applied (HAYKIN, 2009). For the construction of the intelligent element, the relu function was used in the neurons of the intermediate layers and the linear activation function in the output layers, whose characteristics are shown in Table 5.1. The two types of functions were chosen because they present reduced computational effort due to their simplicity.

Table 5.1 - Activation function

Function	Math expression	Graph
Linear	$\varphi(v_j) = v_j$	
Relu	$\varphi(v_j) = \begin{cases} 0 \ if \ v_j < 0 \\ v_j \ if \ v_j \geq 0 \end{cases}$	

Between each neuron layer, a batch normalization layer was used to increase the stability of the element (IOFFE; SZEGEDY, 2015). This layer has the function of normalizing the output of the previous layer according to the equations (5.8), (5.9) and (5.10), in which ϵ is a constant add for numerical stability:

$$\mu_B = \frac{1}{m}\sum_{i=1}^{m} x_i \tag{5.8}$$

$$\sigma_B{}^2 = \frac{1}{m}\sum_{i=1}^{m} (x_i - \mu_B)^2 \tag{5.9}$$

$$\hat{x}_i = \frac{x_i - \mu_B}{\sqrt{\sigma_B^2 + \epsilon}} \tag{5.10}$$

The weights and biases of the network are defined so that the output of the network represents the strain field inside the intelligent element. For this, it is necessary to have a set of input and output data to be used as a reference. The process of defining weights and biases is called training and was performed using a backpropagation algorithm.

The backpropagation algorithm can be divided into two phases: propagation and backpropagation. In the first phase, the signal is propagated through the network, from the input layer towards the output layer, while the weights and biases are fixed. This propagation is basically an attempt to make predictions from the input data. The results of these predictions are compared to the output data samples, producing an error signal. In the second phase, the result of this error is propagated again, layer by layer, from the output towards the input. In this phase, the weights and biases of the neurons are successively adjusted by means of an optimization algorithm, to reduce the error. For the training of the intelligent element, the mean absolute error, shown in Table 5.2, was used as the error measure, in which Y is the output value present in the database, $\hat{Y}$ is the value obtained by the neural network and n is the total number of samples in the database. This error measurement was used because the if MAPE or RMSPE was used the training process would focus on samples with Y_i close to zero, and the convergence for other samples would be slower. Furthermore. If RMSE was used the training process would focus on the larger samples, i.e., samples with the stress concentration results. Thus, MAE is the measurements that had better results for most of the samples, the ones with middle magnitude.

Table 5.2 - Error measurements.

MAE (mean absolute error)	$\dfrac{1}{n}\sum_{i=1}^{n} \lvert Y_i - \hat{Y}_i \rvert$
MAPE (mean absolute percentage error)	$\dfrac{1}{n}\sum_{i=1}^{n} \dfrac{\lvert Y_i - \hat{Y}_i \rvert}{Y_i}$
RMSPE (root mean square percentage error)	$\sqrt[2]{\dfrac{1}{n}\sum_{i=1}^{n} \dfrac{\left(Y_i - \hat{Y}_i\right)^2}{Y_i^{\,2}}}$
RMSE (root mean square error)	$\sqrt[2]{\dfrac{1}{n}\sum_{i=1}^{n} \left(Y_i - \hat{Y}_i\right)^2}$

In this research the optimization algorithm used during the backpropagation step was a gradient-based algorithm, called ADAM (Adaptive Moment Estimation) (KINGMA; BA, 2015). This algorithm was chosen because it is more efficient when compared to heuristic-based algorithms. It also demands less memory and is invariant to the diagonal rescaling of gradients, being, therefore, suitable for problems that have a large amount of data. To avoid stopping at local minima, a learning rate of 0.001 was used. The algorithm proposed by (GLOROT; BENGIO, 2010) is adopted in the present work for the initialization of weights and biases.

5.3.2.1.
Mathematical formulation

The proposed intelligent element uses as input data the nodal coordinates, the nodal displacements, the coordinate of the internal evaluation point, and Poisson's ratio, and it outputs the strain field at the evaluation position. However, to reduce the amount of information needed for training the network, without loss of generality, the input data of the element are transformed and normalized. First, the geometric transformations listed below and shown in Figure 5.5 and expressed mathematically in equation (5.11) are performed.

1. Translation, so that vertex A is positioned at the origin of a local coordinate system.

2. Rotation, so that the longest side is positioned on the coordinate system´s abscissa.

3. Mirroring around the axis normal to side AB passing through its midpoint.

4. Resizing, so that the longest side has unit length.
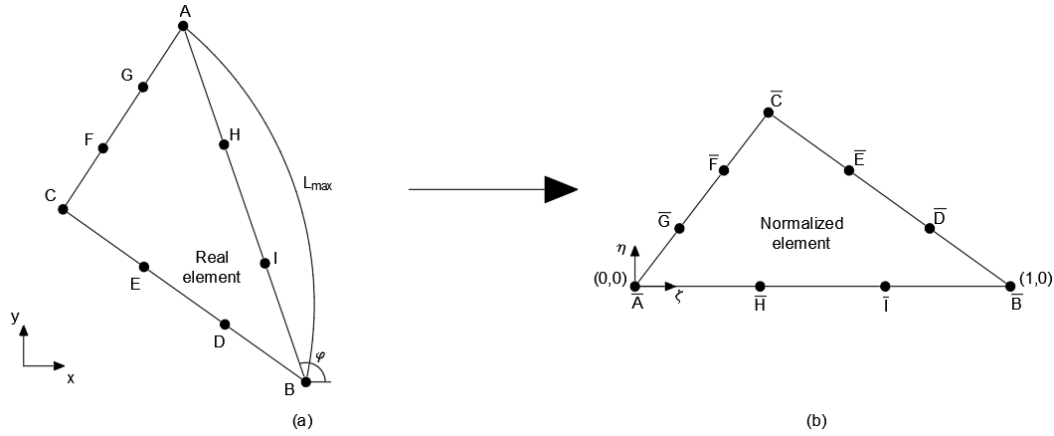
Figure 5.5. Pre-calculation for geometric transformations

$$\begin{Bmatrix} \xi \\ \eta \end{Bmatrix} = \begin{Bmatrix} 1 \\ 0 \end{Bmatrix} - \frac{1}{L_{\overline{AB}}} \cdot \begin{bmatrix} \cos\varphi & -\sin\varphi \\ \cos\varphi & \cos\varphi \end{bmatrix} \cdot \left(\begin{Bmatrix} x \\ y \end{Bmatrix} - \begin{Bmatrix} x_B \\ y_B \end{Bmatrix} \right) \tag{11}$$

After the geometric transformations are performed, the rigid body displacements are removed in such a way that the displacements at node A ($\overline{u_A}$, $\overline{v_A}$) and the vertical displacement at node B ($\overline{v_B}$) are null. Then, the nodal displacements are normalized so that the displacement with the highest value has unit magnitude and the one with the smallest value is null. The coordinates of the internal evaluation point are then expressed using area coordinates ($\overline{\overline{\xi}}$ and $\overline{\overline{\eta}}$ presented in equations (5.12) and (5.13) and the value of Poisson's ratio is normalized by 0.5, as it is the maximum value that this variable can assume.

$$\overline{\overline{\xi}} = \frac{\eta}{2 \cdot A} \tag{5.12}$$

$$\overline{\overline{\eta}} = \frac{\xi \cdot \eta_c - \eta \cdot \xi_c}{2 \cdot A} \tag{5.13}$$

in which A is the area of the element after the geometric transformation.

Therefore, the neural network used in the intelligent element has twenty input data:

- Fifteen nodal displacements: $\overline{u_B}, \overline{u_C}, \overline{v_C}, \overline{u_D}, \overline{v_D}, \overline{u_E}, \overline{v_E}, \overline{u_F}, \overline{v_F}, \overline{u_G}, \overline{v_G},$ $\overline{u_H}, \overline{v_H}, \overline{u_I}, \overline{v_I}$.

- Two coordinates after transformation: ξ_c, η_c

- Two area coordinates of the point where the strain field is evaluated: $\overline{\overline{\xi_\iota}}, \overline{\eta_\iota}$

- The normalized Poisson's ratio: $\overline{v}$

The output data of the neural network are the three non-zero components of the strain tensor of the plane strain state $(\overline{\varepsilon_x}, \overline{\varepsilon_y}, \overline{\gamma_{xy}})$, referenced to the element's local coordinates and normalized by the maximum displacement (d_{max}). Therefore, the strain field evaluated at the point of global coordinates is obtained using equations (5.14), (5.15) and (5.16).

$$\varepsilon_x = \left[\frac{(\overline{\varepsilon_x} + \overline{\varepsilon_y})}{2} + \frac{(\overline{\varepsilon_x} - \overline{\varepsilon_y})}{2} \cdot \frac{\cos 2\varphi}{2} + \overline{\gamma_{xy}} \cdot \frac{\sin 2\varphi}{2} \right] \cdot d_{max} \qquad (5.14)$$

$$\varepsilon_y = \left[\frac{(\overline{\varepsilon_x} + \overline{\varepsilon_y})}{2} - \frac{(\overline{\varepsilon_x} - \overline{\varepsilon_y})}{2} \cdot \frac{\cos 2\varphi}{2} - \overline{\gamma_{xy}} \cdot \frac{\sin 2t}{2} \right] \cdot d_{max} \qquad (5.15)$$

$$\gamma_{xy} = \left[\overline{\gamma_{xy}} \cdot \cos 2t - (\overline{\varepsilon_x} - \overline{\varepsilon_y}) \cdot \sin 2t \right] \cdot d_{max} \qquad (5.16)$$

5.3.2.2.
Database construction

To train the neural network, it is necessary to have a robust set of input data and their respective output data, which properly characterizes the phenomenon for which the network is going to be used. To create the set of data for training the neural network used by the intelligent element it was necessary to generate almost 4000 finite element models with linear triangle element meshes like the one shown in Figure 5.6. These models had different triangular shapes and elastic material properties. The strain field for each model was generated due to prescribed displacements over the sides $\overline{AB}$, $\overline{BC}$ and $\overline{CA}$ of the triangular model, which were also different for each model. By doing this, enables the intelligent element to model the relationship between nodal displacements, element shape, and material with relation to their strain field. To generate this set of models, it was considered a geometry in which vertex A is at the origin, vertex B is at the point (1, 0) and vertex C is at a point in the domain Γ, as shown in Figure 5.7. For the construction

of the Γ domain, the four constraints given by equations (5.17), (5.18), (5.19) and (5.20), were considered, in which x_C, y_C are the coordinates of vertex C and e α and β are, respectively, the angles between sides $\overline{AB}$ and $\overline{CA}$, and between sides $\overline{BC}$ and $\overline{BA}$.
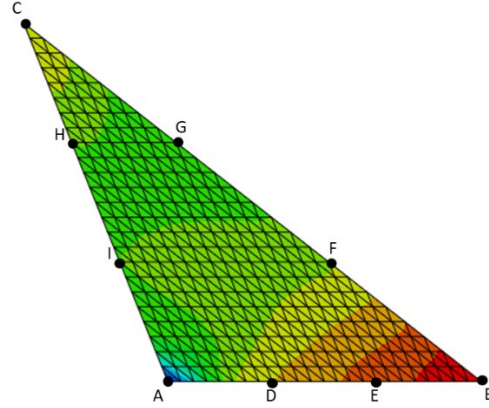
Figure 5.6 - Horizontal strain over a triangular finite element model used for neural network training.
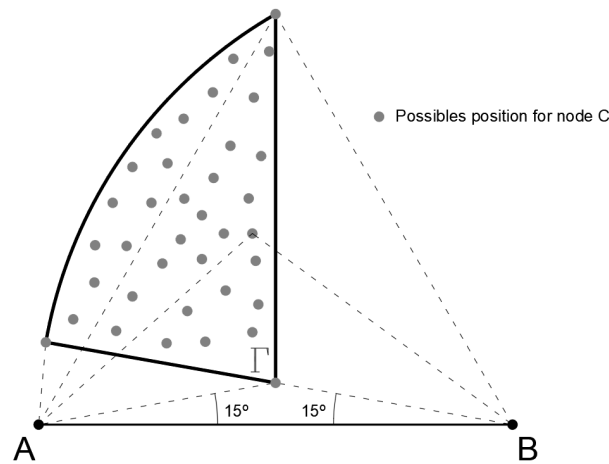
Figure 5.7. Region where it is possible to position vertex C.

$$x_C \leq 0.5, \qquad (5.17)$$

$$y_C > 0.0, \qquad (5.18)$$

$$\alpha \geq 15°, \qquad (5.19)$$

$$\beta \geq 15°, \qquad (5.20)$$

The displacements of the triangular region were generated in such a way that the model did not have rigid body displacements and rotations and considering that the curve of each portion of the displacement on each side was one of the types shown

in Figure 5.8(a). The first two types represent curves where there is a maximum and a minimum point on the side, types 3 and 4 show curves in which there is a maximum or minimum point on the side, and types 5 and 6 represent curves in which there is no maximum and minimum points on de side. Figure 5.8(b) shows an example of an element with nodal displacement following the presented rules. Regarding the material, the Poisson's ratio was varied in the interval [0.0 ,0.5[.
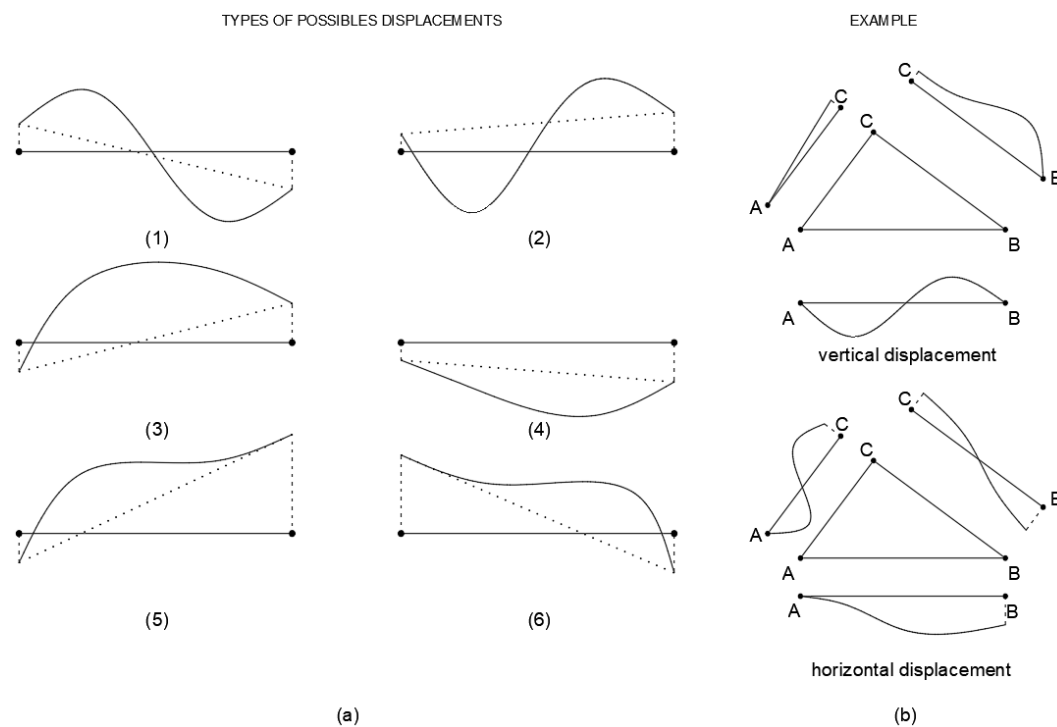
Figure 5.8. (a) Types of possible prescribed side displacements. (b) Example of an element with possible nodal displacements.

5.3.2.3.
Intelligent element topology

The neural network topology is the name given to the way neurons are connected to each other, i.e., it is the number of hidden layers and the number of neurons in each layer. To avoid a trial-and-error procedure, the topology of the intelligent element was defined using a Bayesian search (WU et al., 2019). This procedure is basically a Bayesian Optimization in which the objective function is the error metric, MAE and the variables are the number of hidden layers and the number of neurons per hidden layer. The methodology consisted of training different networks, in which, for each trained network, the topology of the next one was defined in such a way that the average absolute error calculated based on a

validation database had a greater probability of being smaller than the trained networks until that moment. During this process, it was considered that the neural network would have between one and five hidden layers and between 1 and 300 neurons per hidden layer. Finally, the network that presented the best performance was selected, having two hidden layers with 287 neurons in the first hidden layer and 147 neurons in the second hidden layer.

5.3.3.
Numerical integration

The strain and displacement fields of the auxiliary problems are non-polynomial and present singularity at the point load position. When considering the problems that are not expressed by polynomials, numerical integration was performed through the Bartholomew quadrature, and Duffy's transformation was used to treat the singularity.

5.3.3.1.
Bartholomew quadrature

To solve a numerical integration using the Bartholomew quadrature (BARTHOLOMEW, 1959), the physical domain (Ω_t) is mapped to a computational domain (Ω_ξ) shown in Figure 5.9.
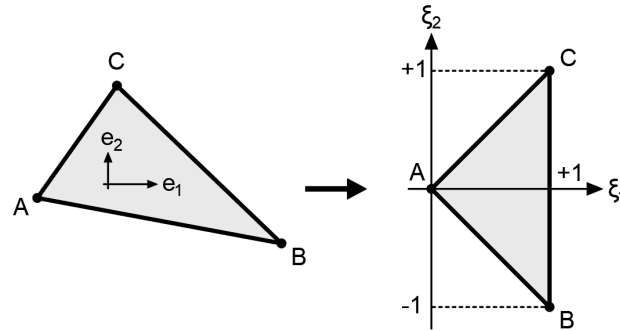
Figure 5.9. Mapping of the physical domain $(\mathbf{\Omega_t})$ to the computational domain $(\mathbf{\Omega_\xi})$.

This mapping is expressed in equation (5.21):

$$x_i = A_{ij}\xi_j + x_i^{(A)} , \qquad (5.21)$$

with:

$$A_{ij} = \frac{1}{2}\left(x_i^{(C)} + x_i^{(B)} - 2x_i^{(A)}\right)e_j \quad \text{if} \quad i = j$$

$$A_{ij} = \frac{1}{2}\left(x_i^{(C)} - x_i^{(B)}\right)e_j \quad \text{if} \quad i \neq j , \qquad (5.22)$$

where ξ_j and e_j are the orthonormal bases of the computational (Ω_ξ) domain and physical domain (Ω_t), respectively.

The level of integration of Bartholomew quadrature is defined by subdivisions in the edges of the computational domain as shown in Figure 5.10. Level n corresponds to 2^{n-1} divisions on each side of the triangular reference element and 4^{n-1} sub-triangles of the same area with the integration point positioned in the middle of the edges of the sub-triangles. If the integration point is on the boundary of the reference triangle it is equal to $1/3 \cdot 1/4^{n-1}$, else it is equal to $2/3 \cdot 1/4^{n-1}$.
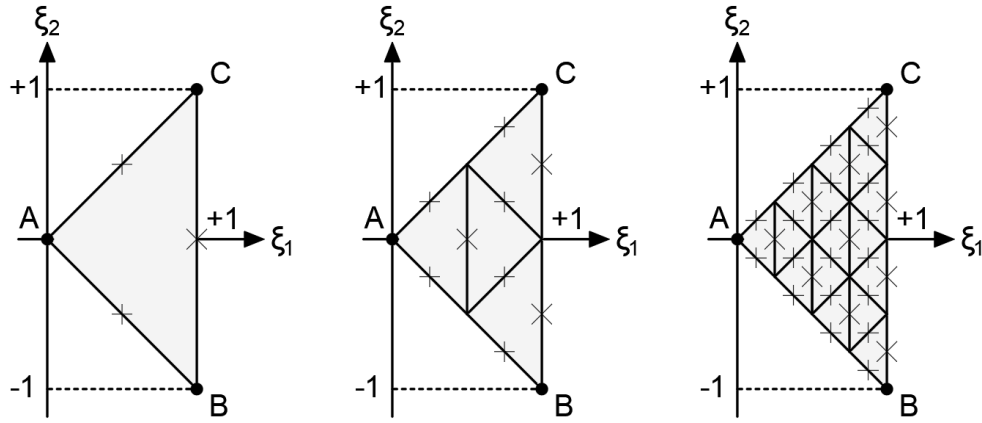
Figure 5.10. Three integration levels with integration points positioned in the computational domain.

5.3.3.2.
Duffy transformation

The application of Duffy's transformation vanishes singularities of the type $\frac{1}{d}$ (where d is the distance from the point load) by mapping the triangular element to a quadrilateral element (BONNET, 2017; MOUSAVI; SUKUMAR, 2010) using equation (5.23):

$$2^n \xi_1 - 1 = \eta_1 \,, \text{and}$$
$$\xi_2 = \xi_1 \, \eta_2 \,,$$

(5.23)

where the Jacobian of the transformation is $\xi_1/2^n$.

This mapping considers the unit point load applied at node A of the first sub-triangle defined by Bartholomew quadrature with level n, and results in a quadrilateral element with both side lengths equal to two, as shown in Figure 5.11.
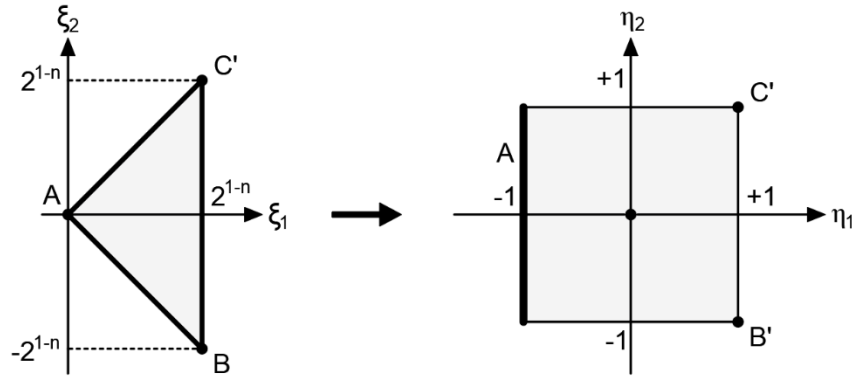
Figure 5.11. Duffy's transformation applied to the first sub-triangle of the Bartholomew quadrature with integration level n.

The integral of the strain field of the auxiliary problem in the computational domain (Ω_t) can be written as shown in equation (5.24):

$$\int_{\Omega_\xi} \frac{f(\alpha)}{d_\xi} J_1 dV_\xi \tag{5.24}$$

where $f(\alpha)$ is a non-singular term, d_ξ is the distance from the point load in the computational domain and J_1 is the Jacobian of the transformation of the physical domain to the computational domain.

Knowing the point load is applied at node A, the first sub-triangle of the Bartholomew quadrature (Figure 5.11) can be transformed into a quadrilateral element through equation (5.25), eliminating the singularity problem in the integrand.

$$\int_{\Omega_\eta} \frac{f(\alpha)}{C_{\xi\xi}^{1/2} (1 + \eta_2^2)^{1/2}} \frac{J_1}{2^n} dV_\eta \, , \tag{5.25}$$

where $C_{\xi\xi} = A_{ij} A_{ji}$.

5.4.
Numerical examples

In this section, two applications of the intelligent element method in reservoir geomechanics problems are presented. The first example consists of a depleting trapezoidal-shaped reservoir into a two-layered stratigraphy. The upper layer is named overburden and the lower is the underburden, as shown in Figure 5.12, both embedded in a semi-infinite media. The material of the overburden, underburden, reservoir and semi-infinite media are linear poro-elastic with

properties shown in Table 5.3. The initial pressure decays inside the reservoir but it remains constant outside.

In the second case, a reservoir located between two geological faults is analyzed, simulating the activities of two wells, one being injected (in the left-side reservoir compartment), and the other being depleted (in the right-side reservoir compartment). The faults also divide the problem in two regions, the overburden and the underburden, as shown in Figure 5.15, also embedded in a semi-infinite media. The materials of the overburden, underbuden, reservoir and semi-infinite media are linear poro-elastic material with properties shown in Table 5.4. The initial pore pressure increases in the left-side reservoir compartment, decreases in the right-side reservoir compartment, and remains constant outside the reservoir. In both cases, the results obtained using intelligent elements are compared with the results obtained from an analysis using a refined mesh of constant strain triangle (T3) elements. As the use of intelligent elements differs from the use of linear elements on the strain calculation. Thus, the processing efficiency can be verified based on the FLOPs (floating point operations) necessary to obtain the strains on the integration points of all elements.

5.4.1.
h-convergence and material properties variation

For the analysis of the first example, the model using T3 elements required a discretization in 4154 elements totaling 4340 degrees of freedom to achieve convergence, while for the model discretized using intelligent elements, 14 elements were needed, totaling 124 degrees of freedom. The two meshes are shown superimposed in Figure 5.12. In both models a level three Bartholomew quadrature was used. The complete set of material properties and loading is presented in Table 3. Comparing the FLOPs of the two types of analysis for this first application it is observed that the use of intelligent element demanded $5{,}91 \cdot 10^9$ FLOPs while the use of a mesh of linear element demanded $1{,}78 \cdot 10^{10}$. This is a threefold improvement in efficiency.

Table 5.3 – Geomechanics properties used in example 1.

Notation	Definition	Value	Unit
Overburden			
E_O	Elasticity modulus	6	GPa
ν_O	Poisson's ratio	0.15	-
Reservoir			
E_R	Elasticity modulus	10	GPa
ν_R	Poisson's ratio	0.2	-
α	Biot coefficient	0.8	-
ΔP_p	Pore pressure change	-15	MPa
Underburden			
E_U	Elasticity modulus	10	GPa
ν_U	Poisson's ratio	0.2	-
Infinite media			
E_∞	Elasticity modulus	20	GPa
ν_∞	Poisson's ratio	0.25	-
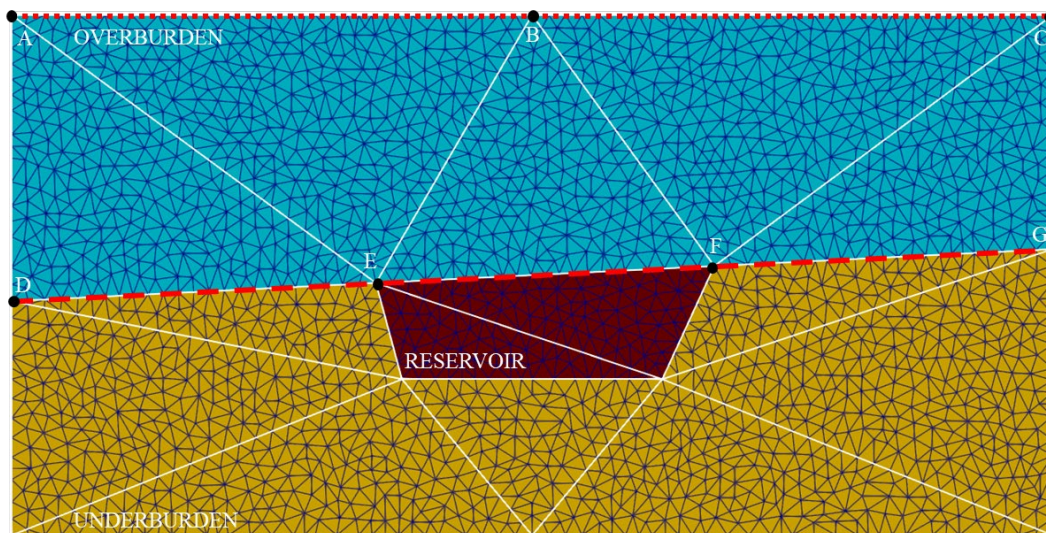
Figure 5.12. Model discretized in T3 elements and in Intelligent element for example 1 overlaid.

Figure 5.13 shows the nodal displacements at the dotted red line at the top of the model (a) and at the dashed red line passing at the top of the reservoir (b) shown in Figure 5.12. The results obtained with both meshes showed maximum subsidence near the center and surface lifting near the right and left edges of the model. On the other hand, the horizontal displacements showed an inversion in the sign of the values close to point B. The numerical results obtained with the intelligent elements are slightly smaller (R2 = 99% for horizontal displacement and R2 = 98% for vertical displacement, where R is the Pearson correlation coefficient) than those obtained with the mesh of T3 elements. However, it was observed that the

displacements calculated for the surface of the massif by the mesh of intelligent elements follow the same shape as the displacement distribution of a mesh with T3 elements that has 35 times more degrees of freedom. A similar pattern was observed for the displacements corresponding to the section marked by the dashed line. In this case, the horizontal and vertical displacements above the reservoir (section between points E and F) obtained by the mesh of intelligent elements are very similar to the ones obtained with the mesh of T3 elements ($R^2 = 99\%$ for horizontal and vertical displacements). In addition, the similarity between the curves obtained by both meshes can be seen, with the advantage of requiring less discretization when using the intelligent element.

Figure 5.13. Displacements over (a) doted segment, and (b) traced segment for numerical example 1.

The comparison between the strain fields obtained with the two meshes shows good agreement, and it is possible to identify the same regions of maximum deformations (Figure 5.14). In both meshes the maximum horizontal elongations occur in the underburden near the two upper vertices of the reservoir, while the maximum horizontal shortenings occur in the interior of the reservoir near the lower vertices. The region near to the center of the reservoir showed a small perturbation in the result of the horizontal strain obtained using the intelligent element mesh. Despite that, for both cases, the average values in this region are within the same order of magnitude ($2 \cdot 10^{-4}$). A similar perturbation is observed in the vertical strain, in which the maximum compaction zone is located near the center of the reservoir for the T3 element mesh but is slightly displaced upwards in the intelligent element mesh. However, the regions of maximum vertical elongation are found in the overburden, close to points E and F in both cases. Similarly, it is observed that in both cases there is a concentration of shear strains at the four corners of the

reservoir. It can, thus, be concluded that a coarse mesh of intelligent elements can obtain similar precision to a mesh of T3 elements, which has approximately 35 times the number of degrees of freedom.
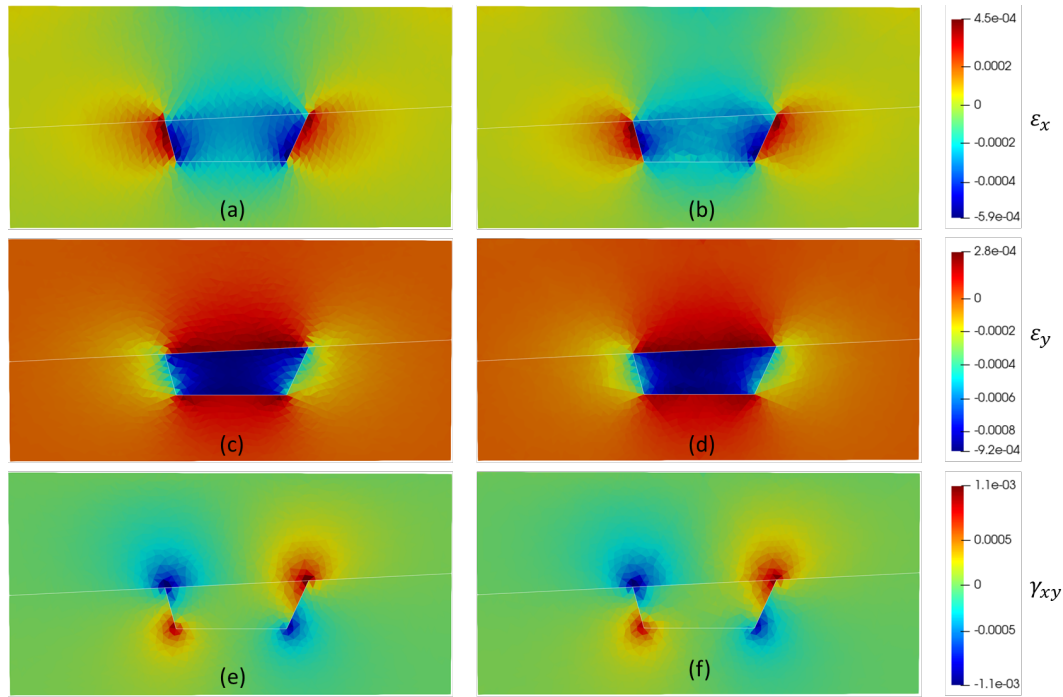
Figure 5.14. Strain fields for T3 element mesh (left) and intelligent element mesh for numerical example 1.

(a) $\varepsilon_{x,T3}$, (b) $\varepsilon_{x,I}$, (c) $\varepsilon_{y,T3}$, (d) $\varepsilon_{y,I}$, (e) $\gamma_{xy,T3}$, (f) $\gamma_{xy,I}$.

5.4.2.
Reservoir with simultaneous injection and depletion

In this section, the case of simultaneous injection and depletion is used to verify the application of the proposed method in problems with non-uniform pore pressure variation. For the analysis using a mesh of T3 elements, a discretization in 4106 elements was necessary, totaling 4294 degrees of freedom, while for the model discretized using intelligent elements, 21 elements were needed, totaling 176 degrees of freedom The two meshes are shown superimposed in Figure 5.15. In both models a level three Bartholomew quadrature was used. The complete set of material and loading parameters is presented in Table 5.4. Comparing the FLOPs of the two types of analysis for this application it is observed that the use of intelligent element demanded $1,12 \cdot 10^{10}$ FLOPs and the use of linear element demanded $1,75 \cdot 10^{10}$. That is the proposed approach is 1.6 times faster.

Figure 5.16 shows the displacements at the dotted red line at the top of the model (a) and at the dashed red line which separates the overburden from underburden (b) shown in Figure 5.15. The results obtained using the two meshes show that the model did not present lifting in any region of its surface, unlike the first example (Section 4.1). In this example, the coarse discretization using intelligent elements did not capture the points of maximum vertical and horizontal displacement, but it was observed that the displacements calculated for the surface of the massif by the mesh of intelligent elements follow the same pattern as the distribution of displacements of a mesh with T3 elements that has approximately 10 times more nodes. In both meshes, the vertical and horizontal displacement in the segment between D and E were almost null. In addition, for both meshes, the point G presents the maximum horizontal displacement (-0,385 m for T3 element mesh and -0,387 m for intelligent element mesh) and the segment between G and H presents de minimum vertical displacement (-0,308 m for T3 element mesh and -0,306 m for intelligent element mesh).

Table 5.4 – Geomechanics properties of example 2.

Notation	Definition	Value	unit
Overburden			
E_O	Elasticity modulus	5	GPa
ν_O	Poisson's ratio	0.15	-
Reservoir A (injecting compartment)			
E_{RI}	Elasticity modulus	15	GPa
ν_{RI}	Poisson's ratio	0.25	-
α_{RI}	Biot coefficient	0.8	-
$\Delta P_{p_{RI}}$	Pore pressure change	20	MPa
Reservoir B (depleting compartment)			
E_{RD}	Elasticity modulus	15	GPa
ν_{RD}	Poisson's ratio	0.25	-
α_{RD}	Biot coefficient	0.8	-
$\Delta P_{p_{RD}}$	Pore pressure change	-20	MPa
Underburden			
E_U	Elasticity modulus	15	GPa
ν_U	Poisson's ratio	0.25	-
Infinite media			
E_∞	Elasticity modulus	20	GPa
ν_∞	Poisson's ratio	0.3	-
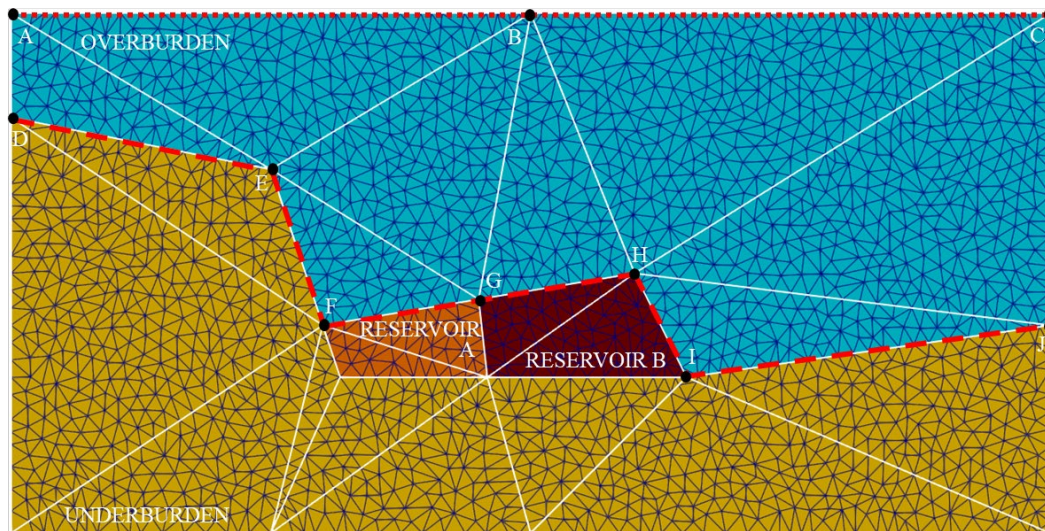
Figure 5.15. Model discretized in T3 elements and in Intelligent element for example 2 overlaid.
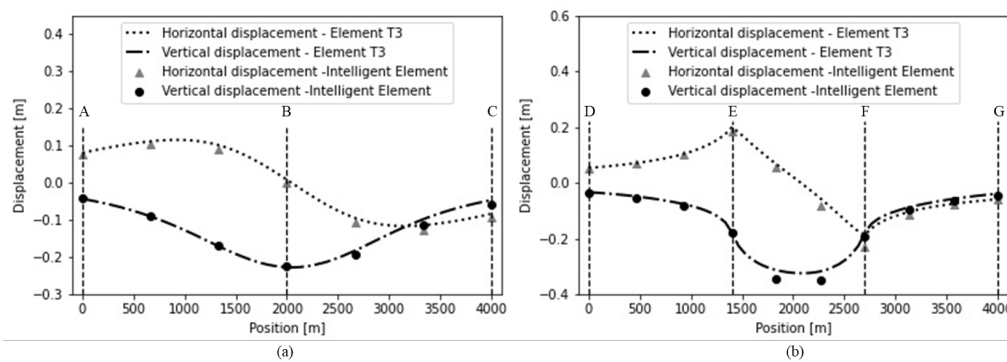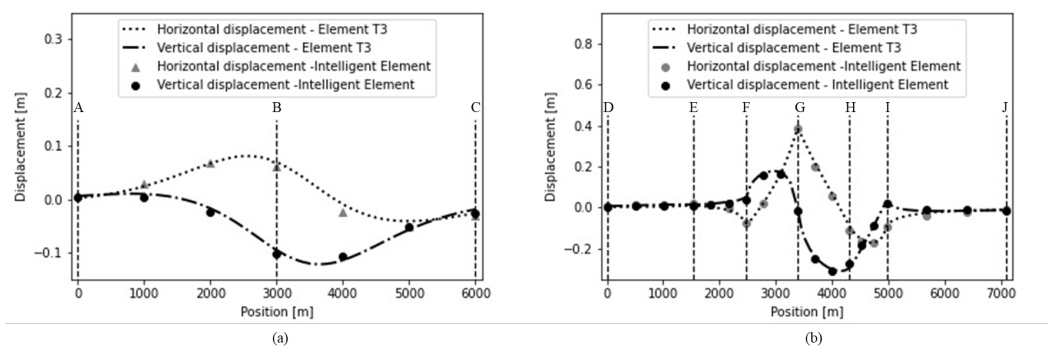

Figure 5.16. Displacements over (a) doted path, and (b) traced path for numerical example 2.

When comparing the strain field obtained by both meshes, it is observed very similar contour plots. It is possible to identify the same regions of maximum deformations, but the concentration of strains is slightly smoother in the intelligent element mesh when compared to the results obtained by the T3 element mesh (Figure 5.17). In both meshes it is possible to observe that the greatest horizontal elongation occurs over the left compartment of the reservoir with magnitude of $9{,}2 \cdot 10^{-4}$, while the maximum shortening occurs in the right compartment with magnitude of $7{,}6 \cdot 10^{-4}$ and, in both cases, close to the boundary between the compartments. Also, close to the same boundary an almost zero vertical strain is observed. Like the numerical example in Section 4.1, for both meshes there is a concentration of shear strain at the vertices of the reservoir compartments. It can,

thus, be concluded that a coarse mesh of intelligent elements can obtain similar precision to a mesh of T3 elements that has approximately 25 times more degrees of freedom.
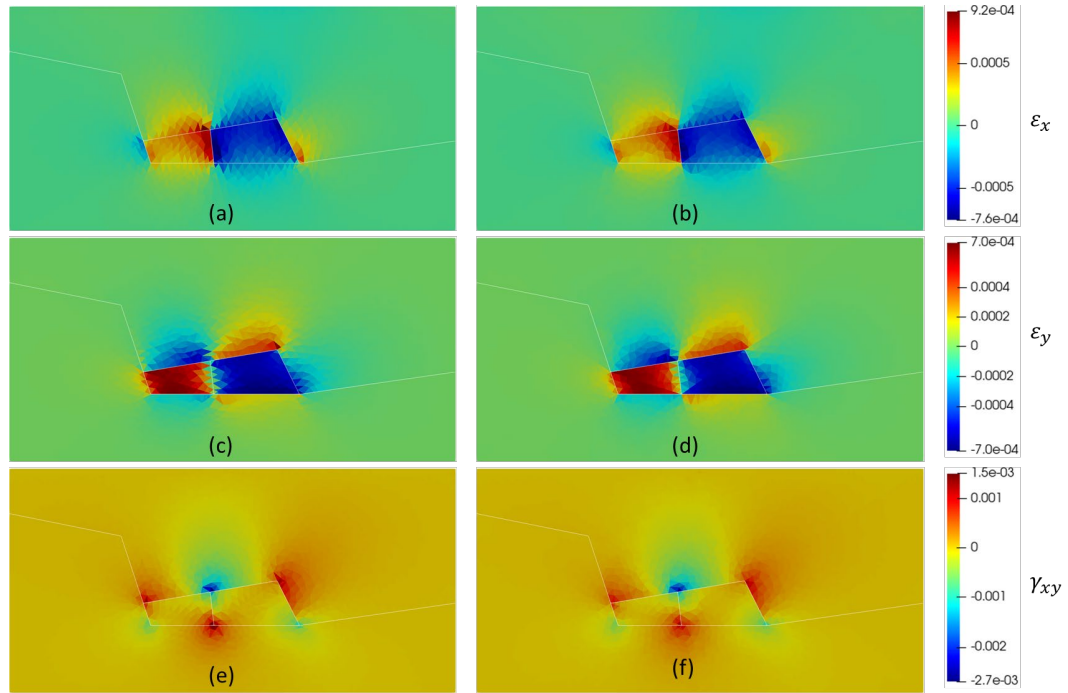
Figure 5.17. Strain fields for T3 element mesh (left) and intelligent element mesh for numerical example 2. (a) $\varepsilon_{x,T3}$, (b) $\varepsilon_{x,I}$, (c) $\varepsilon_{y,T3}$, (d) $\varepsilon_{y,I}$, (e) $\gamma_{xy,T3}$, (f) $\gamma_{xy,I}$.

5.5.
Conclusion

The structured literature review showed the potential of new research that study the use of artificial intelligence to modify numerical methods applied to mechanics and mainly to geomechanics. This research was carried out to explore this potential by proposing a method that combines artificial neural networks with a Green functions approach to solve reservoir geomechanics problems. Thus, the use of intelligent elements allows balancing the need for discretization of classical numerical methods with the specificity of analytical models. To verify the effectiveness and precision of the proposed method, two problems of reservoir geomechanics were analyzed using both a mesh of intelligent elements and a well-discretized mesh of T3 elements.

The first problem consisted in the uniform depleting reservoir embedded in two layered massive. The intelligent element mesh used for this problem had 35

times less degrees of freedom and 300 times less elements than the T3 element mesh. The results for both, displacements, and strains, were similar for both meshes.

The analysis of a second example was carried out to verify the applicability of the method to problems with non-uniform pore pressure variation inside the reservoir. In this example, the results obtained using the intelligent element mesh and the T3 element mesh were also similar. The first mesh had 25 times fewer degrees of freedom and 200 times fewer elements than the second. Thus, the effectiveness of the method in reducing the level of discretization of the model was verified without loss of precision of the results for solving reservoir geomechanics problems.

Besides the fact that the use of intelligent elements instead of a mesh of linear elements requires less FLOPs, it is also important to highlight that the use of artificial neural network enables a simple GPU parallelization, which would also help improve efficiency even further.

Comparing the results of the two examples, it is noticed that there is a reduction in the advantage of using an intelligent element as the geometric complexity of the stratigraphy increases. This occurs because as the geometry of the problem becomes more complex to accurately capture, it is necessary the use of smaller intelligent elements to fit in thin layers, which goes in the opposite direction of the proposed approach.

The results of both examples also validate the reliability of the proposed element since the data used in both applications are different from the data used to train the neural network used in the intelligent element. So, it is expected that for others reservoir geomechanics examples, the element will produce reliable results.

The proposed approach using intelligent elements can be expanded to non-linear and three-dimensional problems. However, to make it feasible it would be necessary an increase in the complexity of the training of the ANN used in the intelligent element. For instance, for three-dimensional problems the training database would require the inclusion of more complex deformation modes. For problems that involve materials with nonlinear behavior, elements that implement different constitutive models would need to be developed. Thus, for its effective use in these types of problems, further studies must be carried out. However, once the network is trained, the use of the intelligent element would be identical to what was presented in the examples.

6
"ANN-based Green's function approach for reservoir geomechanics"

Paper submitted by Matheus L. Peres, Elisa D. Sotelino, and Leonardo C. Mesquita in a peer-reviewed journal.

Abstract

The application of Green's function has been a tool to analyze important effects of the reservoir geomechanics like subsidence, compaction, well closure and the permeability variation. However, the classical Green's function is related to linear elastic, homogenous and geometrically simplified medias. The use of auxiliary functions that consider heterogeneous media has the potential to simplify the numerical analyses of some complex problems. This research work proposes a new approach of the Green's function method based on artificial neural networks (ANN) to consider stratified media with direct application in reservoir geomechanics. These solutions obtained through ANN have as output the normalized displacement at any point of the stratified massif due to the application of a point load inside the massif. The input data of the proposed ANN are the material properties of the media (the elastic properties and the thickness of each layer), the position of the point load, and the location where the displacement is to be evaluated. By using the developed ANN-based Green's function together with the classical Green's function approach, it is possible to obtain the displacement at any point of the massif due to a pore pressure variation within the reservoir without having to solve for the other points in the mesh. Furthermore, with the proposed method, only the reservoir boundary needs to be discretized. These two features lead to a more efficient method when compared to traditional methods, such as the finite element method. For the points of interest, seafloor, and top and bottom of the reservoir, the numerical example presented was 25 times faster than the classic Green function approach on a computer with 12 threads of 2,6GHz and 32GB RAM. This reduction in processing

time is crucial for decision-makers to act in field applications.

6.1. Introduction

Green's functions are traditionally known as a solution of differential equations due to a point disturbance in a medium in several applications and in particular, for the differential equations of static equilibrium which is of interest in this work. These functions are also basis for classical numerical methods like the boundary element method and meshless methods.

Usual Green's functions are formulated for homogeneous media due to the complexity of obtaining analytical expressions for more generic media. One way to overcome this barrier is to calculate Green's functions numerically. However, for some applications, such as fluid dynamics (LIU; IWASHITA; HU, 2015), geophysics (OLSON; ORCUTT; FRAZIER, 1984) and fracture mechanics (TELLES; GUIMARÃES, 2000),the need to numerically solve the Green's function and then apply it to the problem in question becomes computationally expensive. A solution for these situations is the use of Artificial Intelligence as a proxy of Green's functions for more generic material distribution through the media. One class of the AI algorithms that can be used for this purpose consists of artificial neural networks. Since this is the algorithm selected for this work, the developed method is referred to as the ANN-based Green's functions.

Artificial intelligence has been widely applied to mechanical and geomechanical problems. A common application of AI in these areas is the replacement of time-consuming calculation by an AI model (ABDEL AZIM, 2020; KOLAPO et al., 2023; MIANROODI; H. SIBONI; RAABE, 2021). Hence, in this research work the ANN is used as a proxy of a generic Green's function.

The use of Green's functions for heterogeneous media can reduce the computational cost for reservoir geomechanical problems by avoiding the need for solving a non-linear system of equations. The use of the proposed ANN-based Green's function also reduces the computational effort because it only demands the reservoir discretization, while the traditional linear elastic Green's function demands the discretization of the reservoir and the regions around it. Thus, this research work improves the Green's function approach using ANN in order to achieve a Green's function for stratified media. The artificial neural networks used

are multilayer Percepetron type (a feedforward neural network) and their training was based on a database composed of the numerical solutions of several problems that used Green's functions applied to heterogeneous stratified media.

6.2.
Green's function approach for reservoir geomechanics

The Green's function approach for reservoir geomechanics is based on the reciprocity theorem, which relates the solution of two Systems, one auxiliary system and one system of interest. The auxiliary system has as solution a Green's function and the system of interest is the reservoir geomechanics problem to be solved. For the sake of illustration, without loss of generality, consider the Green's function for a force applied in a linear elastic semi-infinite medium (Melan Fundamental Solution), shown in Appendix A, and the problem of interest is a geomechanical reservoir with a porepressure variation located in a stratified zone embedded in a semi-infinite medium (Figure 6.1).
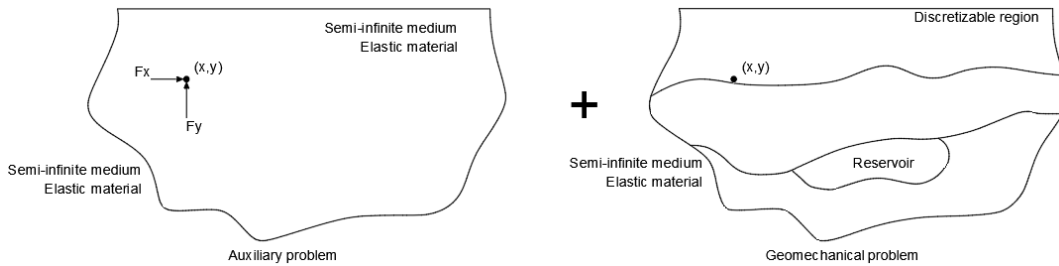
Figure 6.1 - Combining auxiliary problem with reservoir geomechanics.

Defining System number 1 as the auxiliary system and system number 2 as the system of interest, equation (6.1) is obtained applying the mechanical equilibrium condition to the auxiliary system with the virtual displacement field corresponding to the exact solution of the system of interest and vice-versa, in which the superscript denotes the problem number

$$\int_{\Omega_t} \Delta\sigma_{ij}^{(1)}\,\varepsilon_{ij}^{(2)}\,\mathrm{d}V = \int_{\Omega_t} f_i^{(1)}\,u_i^{(2)}\,\mathrm{d}V,$$

$$\int_{\Omega_t} \Delta\sigma_{ij}^{(2)}\,\varepsilon_{ij}^{(1)}\,\mathrm{d}V = \int_{\Omega_t} f_i^{(2)}\,u_i^{(1)}\,\mathrm{d}V.$$

(6.1)

The vectors f_i and u_i represent external force and displacement fields, respectively, the stress change in problem number 1 is $\Delta\sigma_{ij}^{(1)}$ and is associated with

a point load within the domain or on the boundary. Problem number 2 has the unknown stress field $\Delta\sigma_{ij}^{(2)}$ which is related to the strain field $\varepsilon_{ij}^{(2)}$ and a complementary stress $\left(\Delta\sigma_{C_{ij}}^{(2)}\right)$. Considering the constitutive relations (which will be discussed in subsection 6.2.1)

$$\int_{\Omega_t} \mathbb{C}^e_{ijkl}{}^{(1)} \varepsilon_{kl}^{(1)}\varepsilon_{ij}^{(2)} \; dV = \int_{\Omega_t} f_i^{(1)} \, u_i^{(2)} \, dV,$$

$$\int_{\Omega_t} \mathbb{C}^e_{ijkl}{}^{(2)} \varepsilon_{kl}^{(2)}\varepsilon_{ij}^{(1)} \; dV = \int_{\Omega_R} \alpha\Delta P^{(2)}\delta_{ij}\varepsilon_{ij}^{(1)} \, dV + \int_{\Omega_C} \Delta\sigma_{C_{ij}}^{(2)} \, \varepsilon_{ij}^{(1)} \, dV \tag{6.2}$$

in which $\mathbb{C}^e_{ijkl}{}^{(1)}$ is the elastic constitutive tensor, which is symmetrical and, consequently, makes the left-hand sides of the two equations in the system (6.2) equal to each other. Thus, equating the right-hand side of the two equations of the system, results in the expression (6.3)

$$\int_{\Omega_t} f_i^{(1)} \, u_i^{(2)} \, dV = \int_{\Omega_R} \alpha\Delta P^{(2)}\delta_{ij}\varepsilon_{ij}^{(1)} \, dV + \int_{\Omega_C} \Delta\sigma_{C_{ij}}^{(2)} \, \varepsilon_{ij}^{(1)} \, dV \tag{6.3}$$

Knowing that $f_i^{(1)}$ is a generalized force such as a Dirac delta with direction k, equation (6.3) can be rewrite as

$$u_k{}^{(2)}(X_i) = \int_{\Omega_R} \alpha(x_i)\Delta P^{(2)}(x_i)\delta_{mn}\varepsilon_{mnk}{}^{(1)}(x_i, X_i) \, dV$$

$$+ \int_{\Omega_C} \Delta\sigma_{C_{ij}}^{(2)}\varepsilon_{jl}(x_i)\varepsilon_{mnk}{}^{(1)}(x_i, X_i) \, dV, \tag{6.4}$$

where $u_k(X_i)$ is the displacement vector at position X_i, $\alpha(x_i)$, $\Delta P(x_i)$, $C_{mnjl}(x_i)$ and $\varepsilon_{jl}(x_i)$ are, respectively, the Biot coefficient, the pore pressure variation, the constitutive tensor, and the strain variation tensor at position x_i of the real problem. $\varepsilon_{mnk}{}^*(x_i, X_i)$ are the strains at the position X_i due to a point load with direction k applied at x_i. Furthermore, the domain Ω_R represents the region of the model where there is pore pressure variation and the domain Ω_C symbolizes the stratified region where the reservoir is located, referred to in this work as a complementary region.

6.2.1.
Linear poroelasticity applied to heterogeneous problems

The stress field is calculated based on the principle of equivalent stresses, for which the expression in equation (6.5) applies.

$$\Delta\sigma_{ij} = \mathbb{C}_{ijkl}\,\varepsilon_{kl} - A_{ij}\,\Delta\mathrm{P} \tag{6.5}$$

If the term $\mathbb{C}^e_{ijkl}\varepsilon_{kl}$ is added and subtract to equation (6.5), it can be rewritten as

$$\Delta\sigma_{ij} = \mathbb{C}^e_{ijkl}\varepsilon_{kl} - \alpha \cdot \Delta P_p - \left(\mathbb{C}^e_{ijkl} - \mathbb{C}_{ijkl}(x_i)\right)\varepsilon_{kl} \tag{6.6}$$

The third term of the right-hand side of equation (6.6) is defined as the complementary stress

$$\Delta\sigma_{C\,ij} = \left(\mathbb{C}^e_{ijkl} - \mathbb{C}_{ijkl}(x_i)\right)\varepsilon_{kl} \tag{6.7}$$

6.2.2.
Numerical scheme

To solve equation (6.4) the continuous media can be discretized into nR elements in the reservoir region and nC elements in the complementary region, resulting in equation (6.8).

$$
\begin{aligned}
u_k^{(2)}(X_i) = &\sum_{p=1}^{nR} \int_{RE_p} \alpha(x_i)\Delta\mathrm{P}^{(2)}(x_i)\delta_{mn}\varepsilon_{mnk}^{(1)}(x_i, X_i)dV \\
&+ \sum_{q=1}^{nC} \int_{CE_q} \left(\mathbb{C}^e_{mnjl} - \mathbb{C}_{mnjl}(x_i)\right)\varepsilon_{jl}(x_i)\varepsilon_{mnk}^{(1)}(x_i, X_i)\,dV
\end{aligned}
\tag{6.8}
$$

Considering that que pore pressure and the Biot coefficient are uniform in each element, reduces to equation (6.9).

$$
\begin{aligned}
u_k^{(2)}(X_i) = &\sum_{p=1}^{nR} \alpha(x_i)\Delta P_p^{(2)} \int_{RE_p} \delta_{mn}\varepsilon_{mnk}^{(1)}(x_i, X_i)dV \\
&+ \sum_{q=1}^{nC} \int_{CE_q} \left(\mathbb{C}^e_{mnjl} - \mathbb{C}_{mnjl}(x_i)\right)\varepsilon_{jl}(x_i)\varepsilon_{mnk}^{(1)}(x_i, X_i)\,dV
\end{aligned}
\tag{6.9}
$$

This consideration is realistic since the pore pressure variation information is usually provided by discrete models used to define the flow inside the reservoir.

In addition, it is also possible to apply Green's theorem in the integral relative to the reservoir. For the two-dimensional case, the equation (6.10) is obtained

$$u_k{}^{(2)}(X_i) = \sum_{p=1}^{nR} \alpha_p \Delta P_p{}^{(2)} \int_{\partial RE_p} u_{1k}{}^{(1)}(x_i, X_i)dy - u_{2k}{}^{(1)}(x_i, X_i)dx$$

$$+ \sum_{q=1}^{nC} \int_{CE_q} \left(\mathbb{C}^e_{mnjl} - \mathbb{C}_{mnjl}(x_i) \right) \varepsilon_{jl}(x_i) \varepsilon_{mnk}{}^{(1)}(x_i, X_i) \, dV \qquad (6.10)$$

The application of Green's theorem is not trivial for the case under study because the solution of Melan's problem is singular at the position where the point load is applied.

A collocation method can be used to solve equation (6.10) in all points of the discrete model, (ATKINSON; FLORES, 1993). Thus, equation (6.10) can be rewritten in its recurrence form as shown in equation (6.11).

$$u_k{}^{(2)}{}_{a+1}(X_i) = \sum_{p=1}^{nR} \alpha_p \Delta P_p{}^{(2)} \int_{\partial RE_p} u_{1k}{}^{(1)}(x_i, X_i)dy - u_{2k}{}^{(1)}(x_i, X_i)dx$$

$$+ \sum_{q=1}^{nC} \int_{CE_q} \left(\mathbb{C}^e_{mnjl} - \mathbb{C}_{mnjl}(x_i) \right) \varepsilon_{jl_a}(x_i) \varepsilon_{mnk}{}^{(1)}(x_i, X_i) \, dV \qquad (6.11)$$

With the initial solution given by

$$u_k{}^{(2)}{}_0(X_i) = \sum_{p=1}^{nR} \alpha_p \Delta P_p{}^{(2)} \int_{\partial RE_p} u_{1k}{}^{(1)}(x_i, X_i)dy - u_{2k}{}^{(1)}(x_i, X_i)dx \qquad (6.12)$$

The discretization for the first term of equation (6.12) can be the same as the one used for flow simulation. Furthermore, the integration region of the second term of the equation can be discretized in traditional polynomial elements as was done by Peres et al. (2021).

6.3.
ANN-based Green's function Approach

The use of a Green's function that considers the media according to the geomechanical problem makes possible the elimination of the second term on the right side of equation (6.11).

$$u_k{}^{(2)}(X_i) = \sum_{p=1}^{nR} \alpha_p \Delta P_p{}^{(2)} \int_{\partial RE_p} u_{1k}{}^{(1)}(x_i, X_i)dy - u_{2k}{}^{(1)}(x_i, X_i)dx \qquad (6.13)$$

Thus, an iterative solution would not be necessary since the displacements for each point would be obtained from the integration of the Green's function over the contour of the elements within the reservoir. In this work, artificial neural networks of the feedforward multilayer perceptron type were trained to obtain Green's functions that consider a stratified media.

This type of ANN has three types of layers: the input, the output and the Hidden layers as shown in Figure 6.2. Furthermore, it is based on the mathematical expression given by equation (6.14).

$$a_{n+1} = f_{n+1}(W_{n+1}a_n + b_{n+1}) \qquad (6.14)$$

In which a_{n+1} and a_n are the current and the previous layer output, respectively, f_{n+1} and b_{n+1} are the activation function and the bias of the current layer and W_{n+1} is the weight which connects the prior layer to the current. Consequently, a_0 indicates the input data.

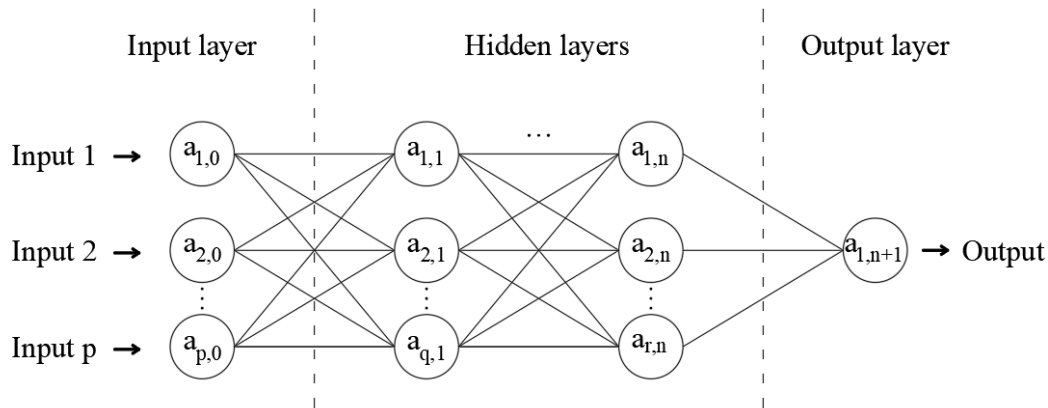Figure 6.2 - Schematic representation of a Multilayer perceptron

However, it is important to highlight that the neural network Green's function, as traditional Green's function presents singularities at the location where the point load is applied.

6.3.1.
Input and output data

The neural networks used as a proxy of the Green's function for stratified media have as input the following parameters:

- The Poisson's ratio of semi-infinite media and each layer

- The elastic modulus of each layer normalized by the elastic modulus of the semi-infinite media

- Each layers thickness

- The depth where the point load is applied

- The relative position between the evaluation point and the point load

For each specific media, different ANN were used depending on its number of layers. This was done to avoid having to consider the number of layers as an input.

Four ANN were trained, one for each of the four displacements considered (vertical or horizontal displacement due to vertical or horizontal unit force). In addition, the output data was normalized (equation (6.15)) to keep its magnitude close to the unit and, thus, improving the efficiency in the training process.

$$\overline{u_{ik}} = \frac{u_{ik}}{u_{kk}^{\infty}} \tag{6.15}$$

where u_{ik} and $\overline{u_{ik}}$ are the displacement and the normalized displacement in i direction due to a unitary point load in k direction, respectively, and u_{kk}^{∞} is the displacement in i direction due to a unitary point load in k direction considering a homogeneous semi-infinite media.

6.3.2.
Data set generation

To train the neural network, it is necessary to have a robust set of input data and their respective output data, which properly characterizes the phenomenon for which the network is going to be used. For the training of the networks used in this research, it was necessary to build a database that had the vertical and horizontal displacements caused by vertical and horizontal unit forces, applied to stratified environments. The displacements were numerically calculated for 24 different media, in order to make the ANN capable of generalizing to different stratigraphies.

The displacements used for training the ANN were obtained numerically from the equation (6.16), which can be obtained based on the reciprocity theorem

analogous to equation (6.10), but for this case the system of interest is the stratified model subjected to a point load.

$$u_k^{(2)}(X_i) = u_k^{(1)}(X_i)$$

$$+ \sum_{q=1}^{nC} \int_{CE_q} \left(\mathbb{C}_{mnjl}^e - \mathbb{C}_{mnjl}(x_i) \right) \varepsilon_{jl}(x_i) \varepsilon_{mnk}^{(1)}(x_i, X_i) \, dV \qquad (6.16)$$

6.3.3.
Neural network training

For the training of the neural networks, data was generated by 24 different models, which were subdivided into 3 groups, i.e., a training group, a validation group, and a test group, corresponding to 70%, 15%, and 15% of the total amount of data, respectively. All models had a discretized width (L) equal to 41km and a discretized depth ($d_1 + d_2 + d_3 + d_4$) varying from 3km to 8km (Figure 5.2).
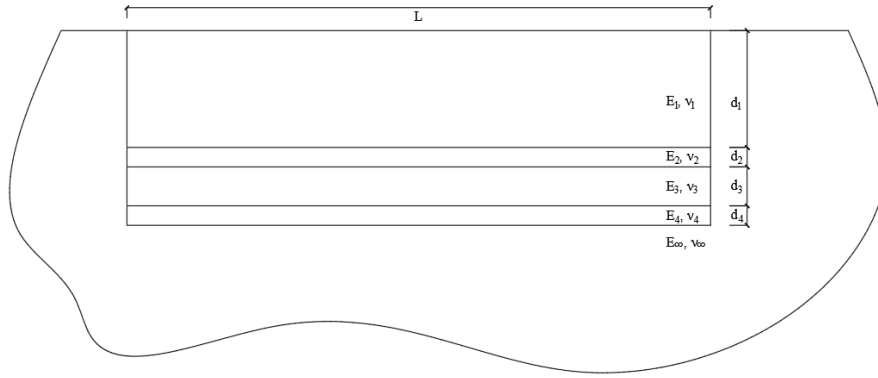
Figure 6.3- Models geometry in the training dataset

The training process traditionally consists of defining weights and biases which produces results that fits the training data. Thus, this process can be understood as an optimization in which the objective function is a measure of error between the output obtained by the training group and the output predicted by the ANN. However, to guarantee extrapolation capacity for other data than the ones from the training group, the early stopping method (KUHN; JOHNSON, 2013) as a regularization technique was used. This method uses the validation group in each training iteration to verify if overfitting is occurring, i.e., it prevents the ANN model from adapting to the training data without adapting to the validation group data. In this article, error measurement considered is the mean squared error.

The training follows the ADAM (Adaptive Moment Estimation) algorithm (KINGMA; BA, 2015), which is a gradient-based algorithm. It was chosen because

it has better efficiency when compared to heuristic-based algorithms. It also demands less memory and is invariant to the diagonal rescaling of gradients, being, therefore, suitable for problems that have a large amount of data. To avoid stopping at local minima, a learning rate of 0.001 was used. The optimization process was initialized with weight and bias defined by the algorithm proposed by Glorot and Bengio (2010). This algorithm initializes the weight and bias following a Gaussian distribution with mean value equal to zero and the variance equal to $\sqrt[2]{2/(f_{in} + f_{out})}$, in which f_{in} is the number of input connections with the first hidden layer and f_{out} is the number of output connections with the last hidden layer.

In addition to the training process involving the calibration of weights and biases, it was also necessary to define the number of hidden layers, the number of neurons per hidden layer, and the activation function to be used in the problem. This was achieved using an iterative training process based on Bayesian search. This adopted procedure is basically a Bayesian Optimization in which the objective function is the error metric calculated for the validation data set and the variables are the activation function, the number of hidden layers and the number of neurons per hidden layer. The methodology consisted of training different networks, in which, for each trained network, the topology of the next one was defined in such a way that the average absolute error calculated based on a validation database had a greater probability of being smaller than the trained networks until that moment. During this process, it was considered that the neural network would have between three and eight hidden layers and between 1 and 300 neurons per hidden layer. Finally, the networks that presented the best performance were selected. These neural networks use the Relu function as activation function for the input and for the hidden layers and a linear function as activation function for the output layer. The number of neurons in each layer are presented in Table 6.1.

Table 6.1 – Number of neurons per layer of each trained ANN

Output	Neurons per layer
$\overline{u_{11}}$	$17 - 242 - 104 - 116 - 92 - 1$
$\overline{u_{21}}$	$17 - 221 - 94 - 262 - 263 - 1$
$\overline{u_{12}}$	$17 - 217 - 198 - 68 - 83 - 72 - 5 - 264 - 1$
$\overline{u_{22}}$	$17 - 97 - 244 - 76 - 179 - 1$

6.4.
Numerical application

In this section, an application of the neural network Green's function is presented. This example consists of a depleting rectangular-shaped reservoir into a four layered stratigraphy. The upper layer is named overburden, the second layer is the cap rock, the third layer is where the reservoir is embedded, and the fourth layer is the substratum as shown in Figure 6.4. The dashed lines in Figure 6.4 represents the delimitation of the reservoir while the letters "L", "R", "T", and "B" represents the left side, the right side, the top and the bottom of the reservoir. The entire model is embedded in a semi-infinite media and all the materials are linear elastic with properties shown in Table 6.2. The initial pressure decays inside the reservoir, but it remains constant outside, which is a usual behavior of reservoir during oil and gas extraction.

This example was solved by the classical Green's function approach and by the ANN-based Green's function approach. Both Results were discussed and compared in relation accuracy and processing time. The discretization considered for the classical approach had 2880 elements and 3066 degrees of freedom and the numerical integration adopted was a level 3 Bartholomew quadrature (BARTHOLOMEW, 1959). For the ANN-based approach, the model was discretized in 44 linear elements around the reservoir, with three-point gauss quadrature rule for numerical integration.
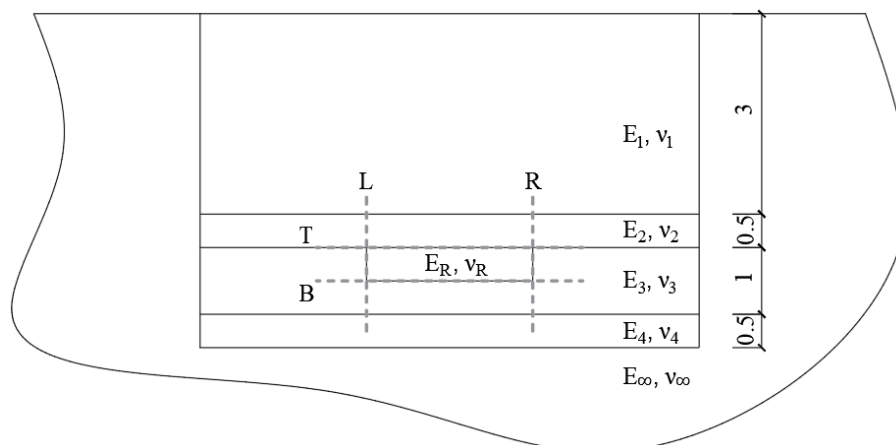
Figure 6.4 – Stratified media of the numerical application.

Table 6.2 – Geomechanics properties for numerical application

Notation	Definition	Value	Unit
Layer 1			
E_1	Elasticity modulus	34	GPa
ν_1	Poisson's ratio	0.25	-
Layer 2			
E_2	Elasticity modulus	46	GPa
ν_2	Poisson's ratio	0.23	-
Layer 3			
E_3	Elasticity modulus	7	GPa
ν_3	Poisson's ratio	0.33	-
Reservoir			
E_R	Elasticity modulus	7	GPa
ν_R	Poisson's ratio	0.33	-
α	Biot coefficient	0.8	-
ΔP_p	Pore pressure change	-10	MPa
Layer 4			
E_4	Elasticity modulus	38	GPa
ν_4	Poisson's ratio	0.34	-
Semi-infinite media			
E_∞	Elasticity modulus	46	GPa
ν_∞	Poisson's ratio	0.20	-

Figure 6.5 shows the vertical displacement in the model's middle along the depth of the model, with the starting point being at the surface and the end point at a depth -5000 m, which represents the contact between the last layer and the semi-infinite media. The proposed ANN-based Green's function approach presented similar results as those obtained using the classical approach. It was observed two points where the neural network Green's function has reduced precision, at the top ($y = -3500$) and at the bottom of the reservoir ($y = -4000$).
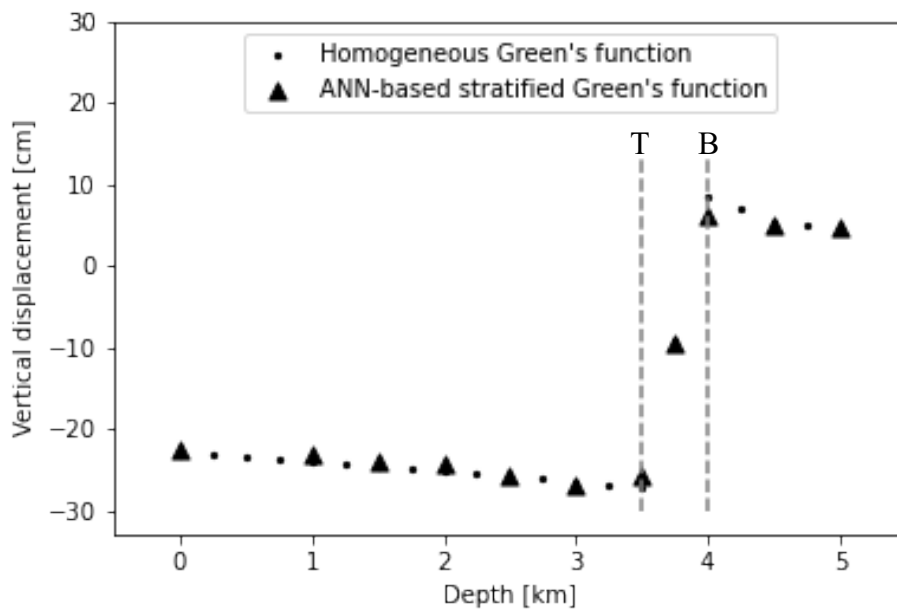
Figure 6.5 – Vertical displacement through depth over (a) x = 0 (inside reservoir)

Figure 6.6 shows the vertical displacement along the width of the model at the surface (a), at the top reservoir (b) y = -3500, and at the bottom reservoir (c) y = -4000. The subsidence results show good agreement between the classical and the neural network approaches. For top and bottom reservoir, it was possible to mimic the shape of the function, but it is observed a gap between classical and neural network curves within the reservoir width.
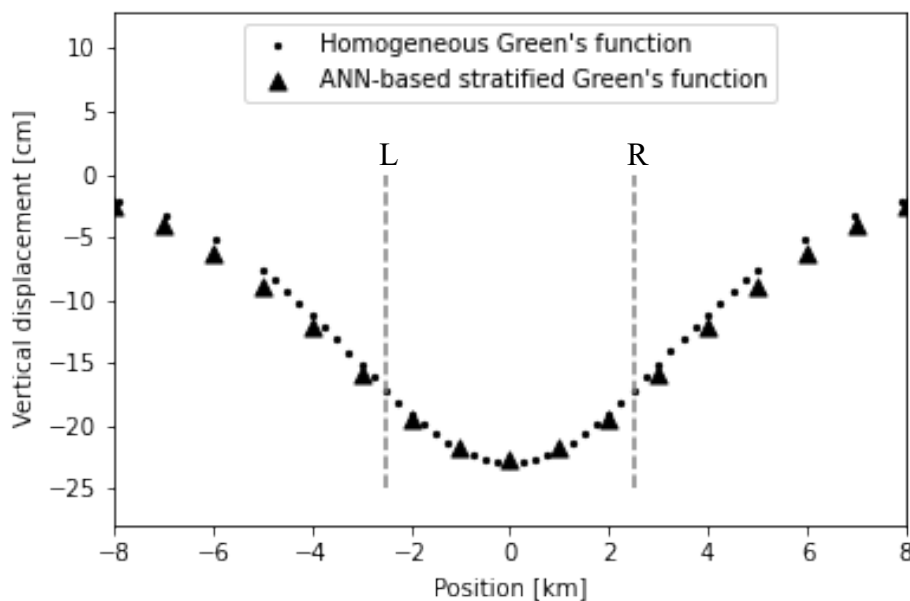
(a)
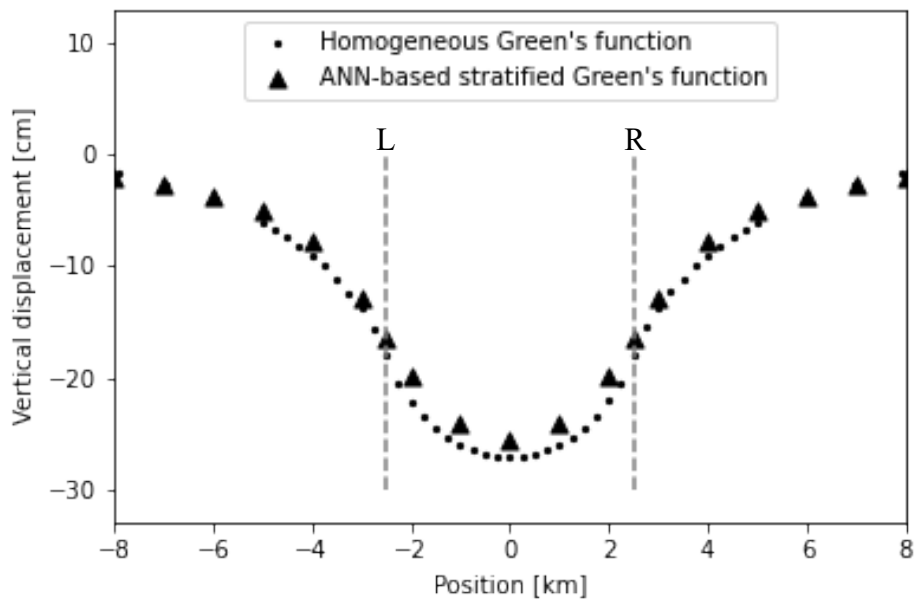
(b)
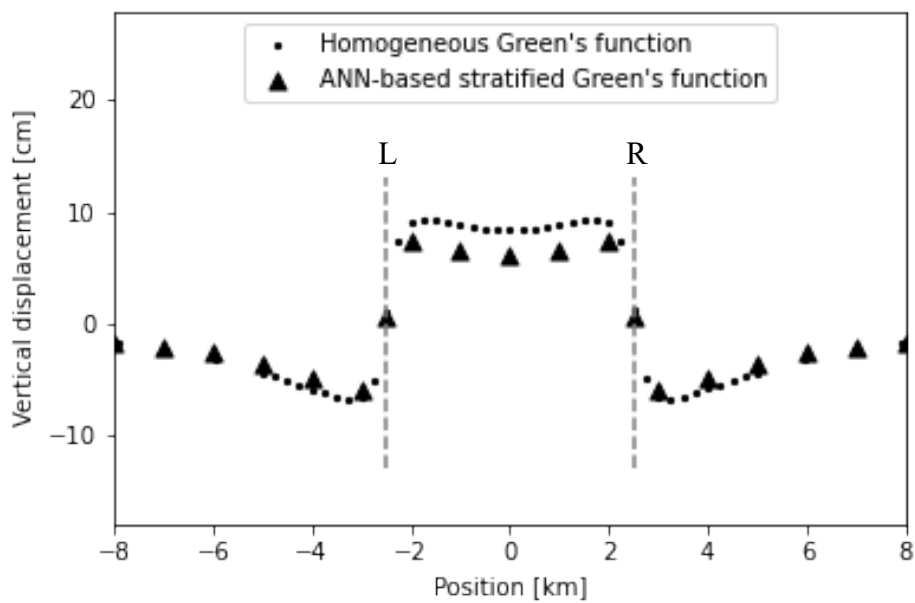
(c)

Figure 6.6 – Vertical displacement through width (a) on the surface above (b) the reservoir and (c) below the reservoir

Figure 6.7 shows the horizontal displacement along the width of the model at the surface (a), at the top reservoir (b) y = -3500, and at the bottom reservoir (c) y = -4000. It can be observed that there is a good agreement between the two approaches at the surface. At the top reservoir both curves are slight difference, but

they present similarities such as a peak at the top corners (with different magnitudes) and a null horizontal displacement at the middle. Observing the horizontal displacement at the bottom of the reservoir the reservoir one can see that the maximum displacements for this depth are in agreement in the two approaches, and the shape of the curve are similar in both cases.

In summary, the ANN-based Green's function approach can provide displacements consistent with the displacements obtained using the classical approach. The main difference between the two approaches is the CPU time required, which is reduced by 25 in 12 threads of 2,6GHz hardware for the neural network approach when compared with the classical one.
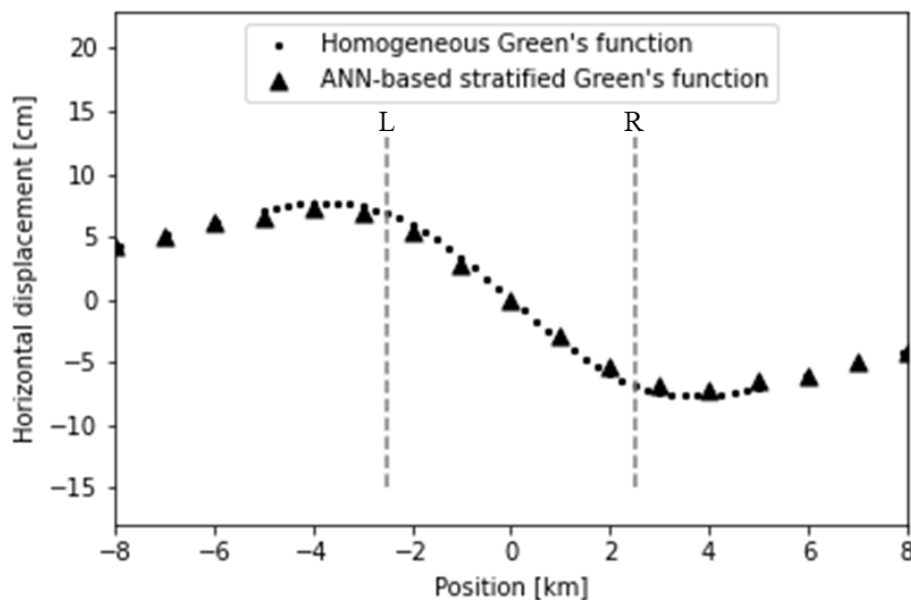
(a)
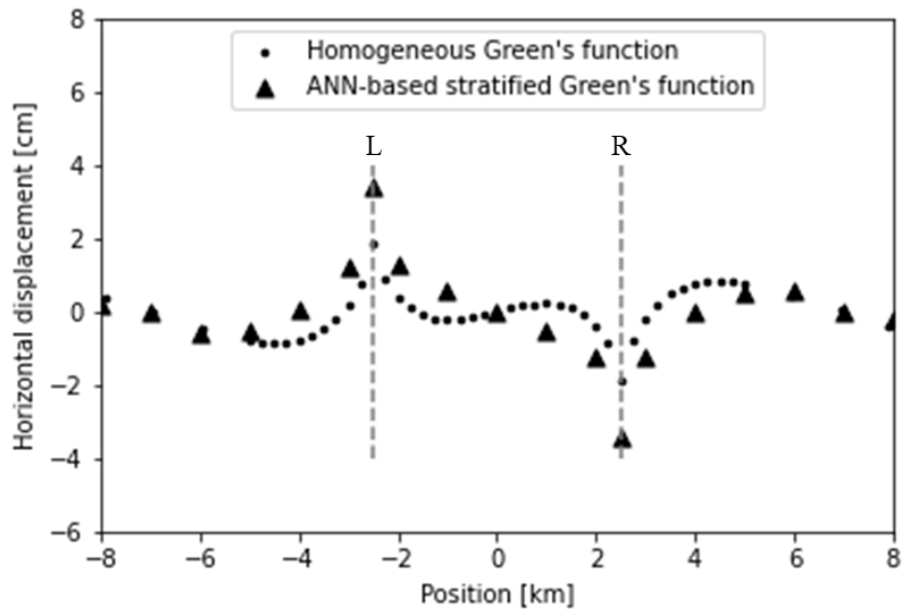
(b)
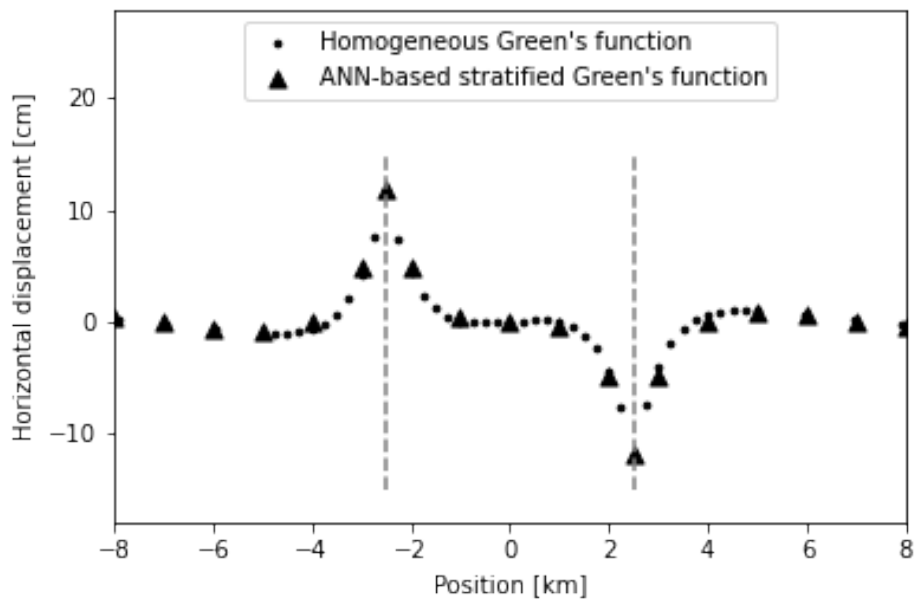
(c)

Figure 6.7 – Horizontal displacement through model width (a) on the surface and (b) below the reservoir.

6.5.
Conclusion

The use of neural networks as a proxy for Green's function makes it possible to obtain generalized fundamental solution more efficiently when compared to the classical method. Using these neural Green's function, it is possible to calculate the displacement field due to a reservoir pore pressure variation discretizing only the boundary reservoir, while the classical approach demands the discretization of the whole massive near the reservoir. Because of this, it is possible to calculate the displacement in each point of the massif without the needing of calculate the displacement in other points of the model. Also, in the proposed approach the iterative process used in the classical approach is no more necessary.

The numerical application consisted in the uniform depleting reservoir embedded in a four layered massive, which is a typical pre-salt field stratigraphy configuration (seafloor, albian, salt and underburden). The Green's function approach demanded the reservoir boundary discretization in 44 linear unidimensional elements while the traditional approach demanded a mesh with 2880 elements and 3066 degrees of freedom. The displacements obtained by the two methods were similar. This validates the reliability of the proposed neural network Green's function, since the data used in the application is different from the data used for the training of the neural network. So, it is expected that for other reservoir geomechanics examples, this approach will also produce reliable results.

The proposed neural Green's function approach can be expanded to non-linear, three-dimensional problems, and to non-horizontal seafloor. However, to make it feasible it is necessary to increase the complexity of the ANNs training. For instance, for three-dimensional problems the training database would require the inclusion of more complex deformation modes. For problems that involve nonlinear materials, the training dataset must be composed of numerical solutions of nonlinear media, which can be time consuming. The neural Green's function can be applied also for more generic material distribution, but it also demands the use of more complex neural network, such as the convolution ANNs. However, once the network is trained, the use of the ANN-based Green's function will be identical to what was presented in the example. For problems with non-horizontal seafloor,

the method is basically the same, but the training dataset would be composed of models with this characteristic.

7
Summary, conclusions, suggestions for future work

This chapter provides an overview of the present research work. The first section summarizes the findings and conclusions on the possibilities of numerical methods improved by artificial intelligence algorithms applied in reservoir geomechanics. The second section suggests the possible paths for future research on this topic.

7.1.
Summary and general conclusions

The structured literature review has clearly shown that although artificial intelligence is a research topic that has received a lot of attention lately. It also showed that the integration between AI and numerical methods applied to mechanics is a promising research area, but it has not been fully explored. Based on the analysis of the papers available in the *Periódicos Capes* database, it was shown that the use of artificial intelligence as a tool to modify classical numerical methods is a path that has the potential to impact the solution of boundary value problems. Consequently, the development of this research work was divided into three phases: the formulation of an approach based on classical mechanics and two improvements of this approach through artificial intelligence algorithms.

In the first phase the Green's function approach was proposed as a simple method that is able to deal with heterogeneous media, and nonlinear materials. The main advantages of using this approach are its capability of demanding only the discretization of regions around the reservoir and its implicitly consideration of the boundary condition by assuming that the reservoir in embedded in a semi-infinite media.

The convergence of the Green's function approach was numerically verified, and its analysis results were compared to the analytical response of a circular reservoir embedded in an infinite media. The disadvantage of this approach is the need of iterative solution even for linear media. Besides that, its

computational cost is directly related with the number of degrees of freedom and the material heterogeneity level.

Based on the Green's function approach, two improvements using artificial neural networks were proposed. The first improvement is the use of intelligent elements for the model discretization. The proposed element uses ANN to proxy the strain field inside the element. These ANN were trained based on triangular finite element model which calculates the strain field inside the model with the boundary displacements constrained. The boundary conditions of the FEM models were set in order to avoid rigid body motion and reduce the size of the training group. After training, an intelligent element with 24 degrees of freedom able to mimic the strain field of a discretized mesh of finite elements was obtained. This element reduces the number of degrees of freedom compared with classical triangular elements, thus considerably speeding up the computations. As the main characteristic of this improvement is the replacement of several linear elements by an intelligent element, this advantage may be not observed for problems with geometries that demand high discretization like stratigraphies with curvilinear surfaces or thin layers.

Two examples were performed in order to verify the ability of the intelligent element to solve geomechanical problems. The intelligent element meshes generated similar results to those obtained using linear triangular elements. However, the mesh of intelligent elements had at least ten times fewer degrees of freedom when compared to the mesh of traditional elements.

The second improvement to the Green's function approach was achieved using ANN-based Green's function for horizontally layered stratigraphy. It consisted in the use of neural networks as a proxy of Green's function for heterogenous media. These ANN were trained based on the displacement field numerically calculated for a point load inside a stratified massive. Therefore, the displacement field due to a pore pressure variation inside a massive is obtained direct without iteration when the ANN-based Green's function is applied. Besides that, its application only demands the discretization of the reservoir boundary and the displacement at one point can be calculate without the needing of compute the displacement for other points of the massive. The main challenge of this approach is the generalization of the ANN-based Green's function for generic stratigraphies beyond the ones with horizontal layers.

The principle used in these two improvements can be applied to order mechanics problems. Furthermore, the results obtained by this research work validate the findings from the literature review that artificial intelligence algorithms are capable of modify and improve classical numerical methods.

7.2.
Future research

This work illustrates that artificial intelligence is capable of improving the computational performance of numerical methods. The proposed strategies can be explored and improved in the development of new approaches.

One of the possible ways to follow is the use of convolutional neural networks to determine the strain fields inside the intelligent element. It is also possible to investigate the creation of elements that incorporate non-linear constitutive properties. For this, one can test other types of neural networks, such as recurrent neural networks, due to the inherent consideration of time-steps required in this type of constitutive model.

In relation to Green's neural function approach, adaptations can be proposed for its application to other geomechanical problems such as hydraulic fracturing and inter-fault sliding. One can also study the use of convolutional networks as a proxy for Green's function, thus allowing the consideration of more generic material distributions other than stratified media. In addition, it is possible to study the application of recurrent neural networks for the consideration of non-linear materials, as was commented in the chapter describing the intelligent element.

8   References

ABDEL AZIM, R. Application of artificial neural network in optimizing the drilling rate of penetration of western desert Egyptian wells. **SN Applied Sciences**, v. 2, n. 7, p. 1–13, 2020.

ABREU, R.; MEJIA, C.; ROEHL, D. Inverse analysis of hydraulic fracturing tests based on artificial intelligence techniques. **International Journal for Numerical and Analytical Methods in Geomechanics**, v. 46, n. 13, p. 2582–2602, 2022.

ALBAHRANI, H.; PAPAMICHOS, E.; MORITA, N. Building an integrated drilling geomechanics model using a machine-learning-assisted poro-elasto-plastic finite element method. **SPE Journal**, v. 26, n. 4, p. 1893–1913, 2021.

ALERIGI, D. P. S. R.; BATARSEH, S. I.; ASSIRI, W. Advances towards a comprehensive model of laser-rock interaction. **Offshore Technology Conference Asia 2020, OTCA 2020**, 2020.

ALTMANN, J. B. et al. Poroelastic contribution to the reservoir stress path. **International Journal of Rock Mechanics and Mining Sciences**, v. 47, n. 7, p. 1104–1113, 2010.

ATKINSON, K.; FLORES, J. The discrete collocation method for nonlinear integral equations. **IMA Journal of Numerical Analysis**, v. 13, n. 2, p. 195–213, 1993.

BARKVED, O. I. et al. The 4D seismic response of a compacting reservoir – SEG / Houston 2005 Annual Meeting SEG / Houston 2005 Annual Meeting. v. 0, n. 1, p. 2508–2512, 2005.

BARTHOLOMEW, G. E. Numerical Integration Over the Triangle. **Mathematical Tables and Other Aids to Computation**, v. 13, n. 68, p. 295, 1959.

BOBET, A. Numerical methods in geomechanics. **Arabian Journal for Science and Engineering**, v. 35, n. 1, p. 27–48, 2010.

BONNET, M. Boundary Integral Equation Methods for Elastic and Plastic Problems. In: **Encyclopedia of Computational Mechanics Second Edition**. Chichester, UK: John Wiley & Sons, Ltd, 2017. p. 1–33.

BONNET, M.; WILEY, J. Boundary Integral Equations for Solids and Fluids. **Journal of Engineering Mechanics**, v. 126, n. 1, p. 120–121, 2000.

BREVIS, I.; MUGA, I.; VAN DER ZEE, K. G. A machine-learning minimal-residual (ML-MRes) framework for goal-oriented finite element discretizations. **Computers and Mathematics with Applications**, n. xxxx, 2020.

BRUNO, M. S. Subsidence-induced well failure. **SPE drilling engineering**, v. 7, n. 2, p. 148–152, 1992.

BUI, H. D. Some remarks about the formulation of three-dimensional thermoelastoplastic problems by integral equations. **International Journal of Solids and Structures**, v. 14, n. 11, p. 935–939, 1978.

CAPUANO, G.; RIMOLI, J. J. Smart finite elements: A novel machine learning application. **Computer Methods in Applied Mechanics and Engineering**, v. 345, p. 363–381, 2019.

CHANG, C.; MAILMAN, E.; ZOBACK, M. Time-dependent subsidence associated with drainage-induced compaction in Gulf of Mexico shales bounding a severely depleted gas reservoir. **AAPG Bulletin**, v. 98, n. 6, p. 1145–1159, 2014.

CYBENKO, G. Approximation by superpositions of a sigmoidal function. **Mathematics of Control, Signals, and Systems**, v. 2, p. 303–314, 1989.

DEO, M. C. Artificial neural networks in coastal and ocean engineering. **Indian Journal of Marine Sciences**, v. 39, n. 4, p. 589–596, 2010.

DU, J.; OLSON, J. E. A poroelastic reservoir model for predicting subsidence and mapping subsurface pressure fronts. p. 181–197, 2001.

ESHELBY, J. D. The determination of the elastic field of an ellipsoidal inclusion , and related problems. p. 376–396, 1957.

ESHELBY, J. D. The elastic field outside an ellipsoidal inclusion. p. 561–569, 1959.

ESHELBY, J. D. Elastic inclusions and inhomogeneities in transversely isotropic solids. n. 1957, p. 239–252, 1961.

FIGUEROA-MIRANDA, S. et al. Land subsidence by groundwater over-exploitation from aquifers in tectonic valleys of Central Mexico : A review. **Engineering Geology**, v. 246, n. August, p. 91–106, 2018.

FOKKER, P. A.; ORLIC, B. Semi-Analytic Modelling of Subsidence 1. v. 38, n. 5, p. 565–589, 2006.

FORTIN, J.; GUÉGUEN, Y.; SCHUBNEL, A. Effects of pore collapse and grain crushing on ultrasonic velocities and Vp/Vs. **Journal of Geophysical Research: Solid Earth**, v. 112, n. 8, p. 1–16, 2007.

FU, Y. et al. A fast solution method for three-dimensional many-particle problems of linear elasticity. **International Journal for Numerical Methods in Engineering**, v. 42, n. 7, p. 1215–1229, 1998.

GAMAGE, K. et al. Permeability-porosity relationships of subduction zone sediments. **Marine Geology**, v. 279, n. 1–4, p. 19–36, 2011.

GAMBOLATI, G. et al. Finite element analysis of land subsidence above depleted reservoirs with pore pressure gradient and total stress formulations. **International Journal for Numerical and Analytical Methods in**

Geomechanics, v. 25, n. 4, p. 307–327, 2001.

GEERTSMA, J. The Effect of Fluid Pressure Decline on V olumetric Changes of Porous Rocks. 1957.

GEERTSMA, J. **Problems of rock mechanics in petroleum production**. Proceedings of 1st ISRM Congress. **Anais**...1966

GEERTSMA, J. Land Subsidence Above Compacting Oil and Gas Reservoirs FGd. **Journal of Petroleum Technology**, 1973a.

GEERTSMA, J. A basic theory of subsidence due to reservoir compaction: the homogeneous case. 1973b.

GHAVAMIAN, F.; SIMONE, A. Accelerating multiscale finite element simulations of history-dependent materials using a recurrent neural network. **Computer Methods in Applied Mechanics and Engineering**, v. 357, p. 112594, 2019.

GLOROT, X.; BENGIO, Y. Understanding the difficulty of training deep feedforward neural networks. **Journal of Machine Learning Research**, v. 9, p. 249–256, 2010.

GREENGARD, L.; ROKHLIN, V. A fast algorithm for particle simulations. **Journal of Computational Physics**, v. 135, n. 2, p. 280–292, 1997.

HAMET, P.; TREMBLAY, J. Artificial intelligence in medicine. **Metabolism: Clinical and Experimental**, v. 69, p. S36–S40, 2017.

HATCHELL, P. et al. Monitoring reservoir compaction from subsidence and time-lapse timeshifts in the Dan field Top Chalk. p. 2867–2871, 2007.

HATCHELL, P.; BOURNE, S. Rocks under strain: Strain-induced time-lapse time shifts are observed for depleting reservoirs. **Leading Edge (Tulsa, OK)**, v. 24, n. 12, p. 1222–1225, 2005.

HAYKIN, S. **Neural networks and learning machines**. third edit ed. New Jersey: Prentice Hall, 2009.

HEIDER, Y.; SUH, H. S.; SUN, W. C. An offline multi-scale unsaturated poromechanics model enabled by self-designed/self-improved neural networks. **International Journal for Numerical and Analytical Methods in Geomechanics**, v. 45, n. 9, p. 1212–1237, 2021.

HERWANGER, J. Seismic geomechanics: how to build and calibrate geomechanical models using 3D and 4D seismic data. **European Association of Geoscientists & Engineers**, p. cp-439, 2014.

HERWANGER, J. V; HORNE, S. A. Linking reservoir geomechanics and time-lapse seismics : Predicting anisotropic velocity changes and seismic attributes. v. 74, n. 4, 2009.

HUANG, J.; WANG, H.; YANG, H. Int-Deep: A deep learning initialized iterative method for nonlinear problems. **Journal of Computational Physics**, v.

419, p. 109675, 2020.

IOFFE, S.; SZEGEDY, C. Batch normalization: Accelerating deep network training by reducing internal covariate shift. **32nd International Conference on Machine Learning, ICML 2015**, v. 1, p. 448–456, 2015.

JUNG, J.; YOON, K.; LEE, P. S. Deep learned finite elements. **Computer Methods in Applied Mechanics and Engineering**, v. 372, p. 113401, 2020.

KAKANI, V. et al. A critical review on computer vision and artificial intelligence in food industry. **Journal of Agriculture and Food Research**, v. 2, n. November 2019, p. 100033, 2020.

KINGMA, D. P.; BA, J. L. Adam: A method for stochastic optimization. **3rd International Conference on Learning Representations, ICLR 2015 - Conference Track Proceedings**, p. 1–15, 2015.

KOEPPE, A.; BAMER, F.; MARKERT, B. An intelligent nonlinear meta element for elastoplastic continua: deep learning using a new Time-distributed Residual U-Net architecture. **Computer Methods in Applied Mechanics and Engineering**, v. 366, p. 113088, 2020.

KOLAPO, P. et al. DFN: An Emerging Tool for Stochastic Modelling and Geomechanical Design. **Eng**, v. 4, n. 1, p. 174–205, 2023.

KOSLOFF, D.; SCOTT, R. F.; SCRANTON, J. Finite element simulation of Wilmington oil field subsidence: I. Linear modelling. **Tectonophysics**, v. 65, n. 3–4, p. 339–368, 1980a.

KOSLOFF, D.; SCOTT, R. F.; SCRANTON, J. Finite element simulation of wilmington oil field subsidence: II. Nonlinear modelling. **Tectonophysics**, v. 70, n. 1–2, p. 159–183, 1980b.

KUHN, M.; JOHNSON, K. **Applied predictive modeling**. [s.l.] Springer, 2013. v. 26

LEE, S.; LEE, C. Prediction of shear strength of FRP-reinforced concrete flexural members without stirrups using artificial neural networks. **Engineering Structures**, v. 61, p. 99–112, 2014.

LEHNER, F. K.; KNOGLINGER, J. K.; D, F. F. Use of a Maysel integral representation for solving poroelastic inclusion problems. **Sixth International Congress on Thermal Stresses, 26-29 May 2005, Vienna, Austria**, p. 77–80, 2005.

LESUEUR, M.; POULET, T.; VEVEAKIS, M. Three-scale multiphysics finite element framework (FE3) modelling fault reactivation. **Computer Methods in Applied Mechanics and Engineering**, v. 365, p. 112988, 2020.

LIANG, L. et al. A deep learning approach to estimate stress distribution: a fast and accurate surrogate of finite-element analysis. **Journal of the Royal Society Interface**, v. 15, n. 138, 2018.

LIN, J.; ZHOU, S.; GUO, H. A deep collocation method for heat transfer in

porous media: Verification from the finite element method. **Journal of Energy Storage**, v. 28, n. October 2019, p. 101280, 2020.

LIU, G. R. A Neural Element Method. **International Journal of Computational Methods**, v. 17, n. 7, 2020.

LIU, Y.; IWASHITA, H.; HU, C. A calculation method for finite depth free-surface green function. **International Journal of Naval Architecture and Ocean Engineering**, v. 7, n. 2, p. 375–389, mar. 2015.

MARKENSCOFF, X.; TRIANTAFYLLIDIS, N. Effects of third-order elastic constants on the buckling of thin plates. **International Journal of Solids and Structures**, v. 15, n. 12, p. 987–992, 1979.

MASTIO, N. et al. Determination of a stress-dependent rock-physics model using anisotropic time-lapse tomographic inversion. **Geophysics**, v. 85, n. 4, p. C141–C152, 2020.

MEHRABIAN, A.; ABOUSLEIMAN, Y. N. Journal of Petroleum Science and Engineering Geertsma ' s subsidence solution extended to layered stratigraphy. **Journal of Petroleum Science and Engineering**, v. 130, p. 68–76, 2015.

MENDIZABAL, A.; MÁRQUEZ-NEILA, P.; COTIN, S. Simulation of hyperelastic materials in real-time using deep learning. **Medical Image Analysis**, v. 59, p. 101569, 2020.

MIANROODI, J. R.; H. SIBONI, N.; RAABE, D. Teaching solid mechanics to artificial intelligence—a fast solver for heterogeneous materials. **npj Computational Materials**, v. 7, n. 1, p. 1–10, 2021.

MINDLIN, R. D. Force at a point in the interior of a semi-infinite solid. **Journal of Applied Physics**, v. 7, n. 5, p. 195–202, 1936.

MINDLIN, R. D.; CHENG, D. H. Nuclei of Strain in the Semi-Infinite Solid. v. 926, n. April 1950, 1950a.

MINDLIN, R. D.; CHENG, D. H. Thermoelastic Stress in the Semi-. v. 931, n. April 1950, p. 7–10, 1950b.

MOULINEC, H.; SUQUET, P. A numerical method for computing the overall response of nonlinear composites with complex microstructure. **Computer Methods in Applied Mechanics and Engineering**, v. 157, n. 1–2, p. 69–94, 1998.

MOUSAVI, S. E.; SUKUMAR, N. Generalized Duffy transformation for integrating vertex singularities. **Computational Mechanics**, v. 45, n. 2–3, p. 127–140, 2010.

MÜLLER, A. C.; GUIDO, S. **Introduction to Machine Learning with Python**. 1. ed. United States of America: O'Reilly Media, 2017.

MUÑOZ, L. F.; ROEHL, D. An analytical solution for displacements due to reservoir compaction under arbitrary pressure changes. v. 52, p. 145–159, 2017.

NABIAN, M. A.; MEIDANI, H. A deep learning solution approach for high-

dimensional random differential equations. **Probabilistic Engineering Mechanics**, v. 57, n. August 2018, p. 14–25, 2019.

NGUYEN-THANH, V. M.; ZHUANG, X.; RABCZUK, T. A deep energy method for finite deformation hyperelasticity. **European Journal of Mechanics, A/Solids**, v. 80, n. July 2019, p. 103874, 2020.

NINTCHEU FATA, S. Explicit expressions for three-dimensional boundary integrals in linear elasticity. **Journal of Computational and Applied Mathematics**, v. 235, n. 15, p. 4480–4495, 2011.

NIU, Z.; LI, Q.; WEI, X. Estimation of the surface uplift due to fluid injection into a reservoir with a clayey interbed. **Computers and Geotechnics**, v. 87, p. 198–211, 2017.

NOURAFKAN, A.; KADKHODAIE-ILKHCHI, A. Shear wave velocity estimation from conventional well log data by using a hybrid ant colony-fuzzy inference system: A case study from Cheshmeh-Khosh oilfield. **Journal of Petroleum Science and Engineering**, v. 127, p. 459–468, 2015.

NOWACKI, W. **Thermoelasticity**. [s.l.] Elsevier, 2013.

OLSON, A. H.; ORCUTT, J. A.; FRAZIER, G. A. The discrete wavenumber/finite element method for synthetic seismograms. **Geophysical Journal of the Royal Astronomical Society**, v. 77, n. 2, p. 421–460, 1984.

OPSTAL, V. **The effect of base-rock rigidity on subsidence due to reservoir compaction**. 1974

OSTENSEN, R. W. Effect of Stress-Dependent Permeability on Gas Production and Well Testing. **SPE Formation Evaluation**, v. 1, n. 3, p. 227–235, 1986.

PAN, E. Static Green's functions in multilayered half spaces. **Applied Mathematical Modelling**, v. 21, n. 8, p. 509–521, 1997.

PERES, M. L. et al. Stress evolution in elastically heterogeneous and non-linear fluid-saturated media with a Green's function approach. **International Journal for Numerical and Analytical Methods in Geomechanics**, v. 45, n. 10, p. 1323–1346, 2021.

RUDNICKI, J. W. Eshelby's Technique for Analyzing Inhomogeneities in Geomechanics. **CISM International Centre for Mechanical Sciences, Courses and Lectures**, v. 533, p. 43–72, 2011.

SAMANIEGO, E. et al. An energy approach to the solution of partial differential equations in computational mechanics via machine learning: Concepts, implementation and applications. **Computer Methods in Applied Mechanics and Engineering**, v. 362, p. 112790, 2020.

SAYERS, C. M.; KACHANOV, M. Microcrack-induced elastic wave anisotropy of brittle rocks. **Journal of Geophysical Research: Solid Earth**, v. 100, n. B3, p. 4149–4156, 1995.

SEGALL, P. Stress and Subsidence Resulting From Subsurface Fluid Withdrawal in the Epicentral Region of the 1983 Coalinga Earthquake. v. 90, n. July 1983, p. 6801–6816, 1985.

SEGALL, P. Induced stress due to fluid extraction from axisymmetric reservoirs. **Pure and Applied Geophysics**, v. 139, n. 3, 1992.

SHEWCHUK, J. R. Applied Computational Geometry Towards Geometric Engineering. **Triangle: Engineering a 2D Quality Mesh Generator and Delaunay Triangulator**, v. 1148, p. 203–222, 1996.

SOLTANZADEH, H.; HAWKES, C. D. Semi-analytical models for stress change and fault reactivation induced by reservoir production and injection. **Journal of Petroleum Science and Engineering**, v. 60, p. 71–85, 2008.

SOUZA, L. M. S.; ROEHL, D. Predicting elastic properties of geomechanical models with Genetic Programming. **53rd U.S. Rock Mechanics/Geomechanics Symposium**, 2019.

SPENCER, B. F.; HOSKERE, V.; NARAZAKI, Y. Advances in Computer Vision-Based Civil Infrastructure Inspection and Monitoring. **Engineering**, v. 5, n. 2, p. 199–222, 2019.

STROUD, A. H.; SECREST, D. **Gaussian Quadrature Formulas: By AH Stroud and Don Secrest**. [s.l.] Prentice-Hall, 1966.

SWEDLOW, J. L.; CRUSE, T. A. Formulation of boundary integral equations for three-dimensional elasto-plastic flow. **International Journal of Solids and Structures**, v. 7, n. 12, p. 1673–1683, 1971.

TANDON, S. Improved analysis of stimulated reservoir volumes in unconventional reservoirs using supervised learning techniques. **SPE Eastern Regional Meeting**, v. 2019- Octob, 2019.

TARIQ, Z. et al. A new technique to develop rock strength correlation using artificial intelligence tools. **Society of Petroleum Engineers - SPE Reservoir Characterisation and Simulation Conference and Exhibition, RCSC 2017**, p. 1340–1353, 2017.

TELLES, J. C. F.; BREBBIA, C. A. On the application of the boundary element method to plasticity. **Applied Mathematical Modelling**, v. 3, n. 6, p. 466–470, 1979.

TELLES, J. C. F.; BREBBIA, C. A. Boundary element solution for half-plane problems. **International Journal of Solids and Structures**, v. 17, n. 12, p. 1149–1158, 1981.

TELLES, J. C. F.; GUIMARÃES, S. Green's function: A numerical generation for fracture mechanics problems via boundary elements. **Computer Methods in Applied Mechanics and Engineering**, v. 188, n. 4, p. 847–858, 2000.

TEMPONE, P.; FJÆR, E.; LANDRØ, M. Improved solution of displacements due to a compacting reservoir over a rigid basement. **Applied Mathematical Modelling**, v. 34, n. 11, p. 3352–3362, 2010.

TEMPONE, P.; LANDRØ, M.; FJÆR, E. 4D gravity response of compacting reservoirs : Analytical approach. v. 77, n. 3, p. 45–54, 2012.

VAIROGS J et al. Effect of rock stress on gas production from low-permeability reservoirs. **JPT, Journal of Petroleum Technology**, v. 23, p. 1161–1167, 1971.

VASILYEVA, M. et al. Preconditioning Markov Chain Monte Carlo Method for Geomechanical Subsidence using multiscale method and machine learning technique. **Journal of Computational and Applied Mathematics**, v. 392, p. 113420, 2021.

VOYIADJIS, G. Z.; ZHOU, Y. Time-dependent modeling of subsidence due to drainage in bounding shales: Application to a depleted gas field in Louisiana. **Journal of Petroleum Science and Engineering**, v. 166, n. January, p. 175–187, 2018.

WALSH, J. B. Subsidence above a planar reservoir. **Journal of Geophysical Research: Solid Earth**, v. 107, n. B9, p. ETG 6-1-ETG 6-9, 2002.

WANGEN, M. Finite element modeling of hydraulic fracturing in 3D. **Computational Geosciences**, v. 17, n. 4, p. 647–659, 2013.

WANGEN, M.; HALVORSEN, G. A Three-Dimensional Analytical Solution for Reservoir Expansion , Surface Uplift and Caprock Stress Due to Pressurized Reservoirs. **Mathematical Geosciences**, v. 52, n. 2, p. 253–284, 2019.

WEBSTER, J.; WATSON, R. T. a Nalyzing the Past To P Repare for the Future : Writing a Literature Review. **MIS Quarterly**, v. 26, n. 2, 2002.

WU, J. et al. Hyperparameter optimization for machine learning models based on Bayesian optimization. **Journal of Electronic Science and Technology**, v. 17, n. 1, p. 26–40, 2019.

XING, H.; XU, L. D. Feature space theory Ð a mathematical foundation for data mining q. **Systems Research and Behavioral Science**, v. 14, p. 253–257, 2001.

YANG, B. et al. Development of a KBS for managing bank loan risk. **Knowledge-Based Systems**, v. 14, n. 5–6, p. 299–302, 2001.

YUDOVICH, A.; CHIN, L. Y.; MORGAN, D. R. Casing deformation in Ekofisk. **Proceedings of the Annual Offshore Technology Conference**, v. 1988-May, n. July, p. 63–72, 1988.

ZHANG, C.; LU, Y. Study on artificial intelligence: The state of the art and future prospects. **Journal of Industrial Information Integration**, v. 23, n. March, p. 100224, 2021.

ZHANG, S. et al. Application of computational intelligence method in petroleum geomechanics characterization. **International Journal of Computational Intelligence and Applications**, v. 13, n. 4, 2014.

ZHANG, S. et al. Estimation of earth stresses and fracture properties using

numerical method and soft computing. **International Journal of Computational Science and Engineering**, v. 13, n. 4, p. 390–399, 2016.

ZHANG, S. et al. An application of soft computing for the earth stress analysis in hydropower engineering. **Soft Computing**, v. 24, n. 7, p. 4739–4749, 2020a.

ZHANG, Y. et al. Displacement Back-Analysis of Rock Mass Parameters for Underground Caverns Using a Novel Intelligent Optimization Method. **International Journal of Geomechanics**, v. 20, n. 5, p. 04020035, 2020b.

ZHAO, H. A reduced order model based on machine learning for numerical analysis: An application to geomechanics. **Engineering Applications of Artificial Intelligence**, v. 100, n. February, p. 104194, 2021.

ZHOU, Y.; VOYIADJIS, G. Z. Finite element modeling of production-induced compaction and subsidence in a reservoir along Coastal Louisiana. **Journal of Coastal Research**, v. 35, n. 3, p. 600–614, 2019.

Appendix A
Melan fundamental solution

The Green Functions for elastic semi-infinite media $(\varepsilon_{mnp}(x_i, X_i))$ and $(u_{np}(x_i, X_i))$ can be decomposed into the sum of two parts, the first referring to the 2D Green Function for elastic infinite media, represented by $\varepsilon_{mnp}(x_i, X_i)^K$ and $u_{np}(x_i, X_i)^K$, and the second formed by complementary terms, represented by $\varepsilon_{mnp}(x_i, X_i)^C$ and $u_{np}(x_i, X_i)^C$, X_i denoting the position of the point load and x_i denoting the position where the strains are evaluated, defined in Figure A.1.

$$\varepsilon_{mnp}(x_i, X_i) = \varepsilon_{mnp}(x_i, X_i)^K + \varepsilon_{mnp}(x_i, X_i)^C \,, \tag{A.1}$$

$$u_{np}(x_i, X_i) = u_{np}(x_i, X_i)^K + u_{np}(x_i, X_i)^C \,, \tag{A.2}$$

A.1.
2D Kelvin's fundamental solution

Using the Cartesian coordinate system shown in Figure. A.1, the strains and displacements at position x_i generated by a horizontal unit point load applied at point X_i are given by:
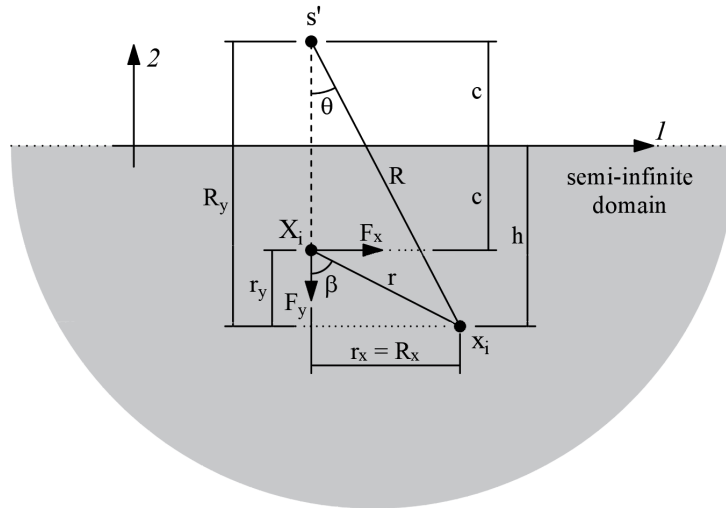

Figure. A.1. The 2D coordinate system for point load in semi-infinite media.

$$\varepsilon_{111}^K = \frac{A \sin \beta}{r} \{2(1 - \sin^2 \beta) + (4\nu - 3)\} \,, \tag{A.3}$$

$$\varepsilon_{221}^K = \frac{A \sin \beta}{r}(1 - 2\cos^2 \beta),$$ (A.4)

$$\varepsilon_{121}^K = \varepsilon_{211}^K = \frac{A \cos \beta}{r}\{2\nu - 1 - 2\sin^2 \beta\}.$$ (A.5)

$$u_{11}^K = A\left[\frac{r_x^2}{r^2} - (3 - 4\nu) \cdot \ln r\right],$$ (A.6)

$$u_{21}^K = A\frac{r_x \cdot r_y}{r^2}.$$ (A.7)

With:

$$A = \frac{1 + \nu}{4\pi E(1 - \nu)}.$$ (A.8)

Thus, the first part of the Green functions for horizontal direction is defined by:

$$\varepsilon_{mn1}(x_i, X_i)^K = \begin{bmatrix} \varepsilon_{111}^K & \varepsilon_{121}^K \\ \varepsilon_{211}^K & \varepsilon_{221}^K \end{bmatrix},$$ (A.9)

$$u_{n1}(x_i, X_i)^K = \begin{bmatrix} u_{11}^K \\ u_{21}^K \end{bmatrix},$$ (A.10)

The strains and displacements at position x_i generated by a vertical unit point load applied at point X_i are given by:

$$\varepsilon_{112}^K = \frac{A \cos \beta}{r}(1 - 2\sin^2 \beta),$$ (A.11)

$$\varepsilon_{222}^K = \frac{A \cos \beta}{r}\{2(1 - \cos^2 \beta) + (4\nu - 3)\},$$ (A.12)

$$\varepsilon_{122}^K = \varepsilon_{212}^K = \frac{A \sin \beta}{r}\{2\nu - 1 - 2\cos^2 \beta\}.$$ (A.13)

$$u_{12}^K = A\frac{r_x \cdot r_y}{r^2},$$ (A.14)

$$u_{22}^K = A\left[\frac{r_x^2}{r^2} - (3 - 4\nu) \cdot \ln r\right].$$ (A.15)

Thus, the first part of the Green function for vertical direction is defined by:

$$\varepsilon_{mn2}(x_i, X_i)^K = \begin{bmatrix} \varepsilon_{112}^K & \varepsilon_{122}^K \\ \varepsilon_{212}^K & \varepsilon_{222}^K \end{bmatrix},$$ (A.16)

$$u_{n2}(x_i, X_i)^K = \begin{bmatrix} u_{12}^K \\ u_{22}^K \end{bmatrix}. \tag{A.17}$$

A.1.
Complementary part

The complementary strains and displacements at position x_i generated by a horizontal unit point load applied at point X_i are given by:

$$\varepsilon_{111}^C = A\frac{\sin\theta}{R}\left\{-8(1-v)^2 + (3-4v)(3-2\sin^2\theta) - \frac{4ch}{R^2}(3-4\sin^2\theta)\right\}, \tag{A.18}$$

$$\varepsilon_{221}^C = A\frac{\sin\theta}{R}\left\{-4(1-2v)(1-v) - \frac{4c\cos\theta}{R} + (3-4v)\left(1-\frac{2r_y\cos\theta}{R}\right)\right. \tag{A.19}$$
$$\left. -\frac{4ch}{R^2}(1-4\cos^2\theta)\right\},$$

$$\varepsilon_{121}^C = \varepsilon_{211}^C = \frac{A\cos\theta}{2R}\left\{\left(\frac{2c+(3-4v)r_y}{R_y}\right)(1-2\sin^2\theta) + \frac{8ch}{R^2}(4\sin^2\theta - 1)\right. \tag{A.20}$$
$$\left. -2(3-4v)\sin^2\theta - 1\right\}.$$

$$u_{11}^C = A\left[-8\cdot(1-v)^2\cdot\ln r + (3-4v)\cdot\ln r + \frac{(3-4v)}{R^2}\cdot r_x{}^2 + \frac{2\cdot c\cdot h}{R^2}\right. \tag{A.21}$$
$$\left. -\frac{4\cdot c\cdot x\cdot r_x{}^2}{R^4}\right],$$

$$u_{21}^C = -A\left[(3-4v)\cdot\frac{r_x\cdot r_y}{R} - \frac{4\cdot c\cdot x\cdot R_y\cdot r_x}{R^4} + 4\cdot(1-v)\cdot(1-2v)\cdot\theta\right], \tag{A.22}$$

Thus, the second part of the Green function for horizontal direction is defined by:

$$\varepsilon_{mn1}(x_i, X_i)^C = \begin{bmatrix} \varepsilon_{111}^C & \varepsilon_{121}^C \\ \varepsilon_{211}^C & \varepsilon_{112}^C \end{bmatrix}, \tag{A.23}$$

$$u_{n1}(x_i, X_i)^C = \begin{bmatrix} u_{11}^C \\ u_{21}^C \end{bmatrix}, \tag{A.24}$$

The strains and displacements at position x_i generated by a vertical unit point load applied at point X_i are given by:

$$\varepsilon_{112}^C = \frac{A\cos\theta}{R}\left\{-4(1-v)(1-2v) - \frac{(3-4v)r_y}{R_y} + \frac{2(3-4v)r_y\cos\theta}{R}\right. \tag{A.25}$$
$$\left. + \frac{4ch}{R^2}(4\cos^2\theta - 3)\right\},$$

$$\varepsilon_{222}^{C} = \frac{A\cos\theta}{R}\left\{[3(3-4v)-8(1-v)^2]-\frac{2c}{R_y}+\frac{4c}{R}\left(\cos\theta+\frac{3h}{R}\right)\right.$$
$$\left.-\left[2(3-4v)+\frac{16ch}{R^2}\right]\cos^2\theta\right\},$$
(A.26)

$$\varepsilon_{122}^{C} = \varepsilon_{212}^{C} = \frac{A\sin(\theta)}{2R}\left\{2(1+2v)+\frac{\cos(\theta)}{R}\left(4c-2r_y(3-4v)\right)\right.$$
$$\left.+\frac{8ch}{R^2}(1-4\cos^2(\theta))-2(3-4v)\cos^2(\theta)\right\}.$$
(A.27)

$$u_{12}^{C} == -A\left[(3-4v)\cdot\frac{r_x\cdot r_y}{R}+\frac{4\cdot c\cdot x\cdot R_y\cdot r_x}{R^4}-4\cdot(1-v)\cdot(1-2v)\cdot\theta\right],$$
(A.28)

$$u_{21}^{C} = A\left[-8\cdot(1-v)^2\cdot\ln r+(3-4v)\cdot\ln r+\frac{(3-4v)}{R^2}\cdot R_y^2-\frac{2\cdot c\cdot h}{R^2}\right.$$
$$\left.+\frac{4\cdot c\cdot x\cdot R_y^2}{R^4}\right],$$
(A.29)

Thus, the second part of the Green function for vertical direction is defined by:

$$\varepsilon_{mn2}(x_i,X_i)^C = \begin{bmatrix} \varepsilon_{112}^{C} & \varepsilon_{122}^{C} \\ \varepsilon_{212}^{C} & \varepsilon_{222}^{C} \end{bmatrix},$$
(A.30)

$$u_{n2}(x_i,X_i)^C = \begin{bmatrix} u_{12}^{C} \\ u_{22}^{K} \end{bmatrix},$$
(A.31)

Appendix B
Numerical quadrature over the triangle

It is proposed to use the quadrature outlined in (BARTHOLOMEW, 1959) with the mapping from the physical domain Ω_t to the computational domain Ω_ξ presented in Figure B1.
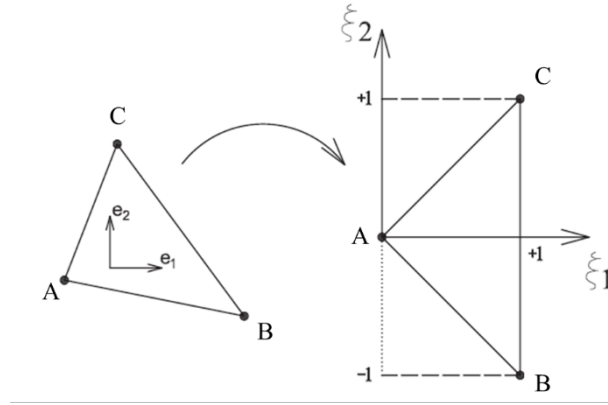
Figure. B2. Mapping from the physical to the computational domain for numerical quadrature over the triangle, if the point load is not at one of the three nodes

This mapping is expressed as

$$x_i = F_{ij}\xi_j + x_A, \tag{B.1}$$

with

$$F_{11} = \frac{(x_C + x_B - 2x_A)}{2}, \tag{B.2}$$

$$F_{21} = \frac{(x_C + x_B - 2x_A)}{2}, \tag{B.3}$$

$$F_{11} = \frac{(x_C - x_B)}{2}, \tag{B.4}$$

$$F_{11} = \frac{(x_C - x_B)}{2}, \tag{B.5}$$

The positions of the quadrature points are presented in Figure B2 for three levels of numerical integration.

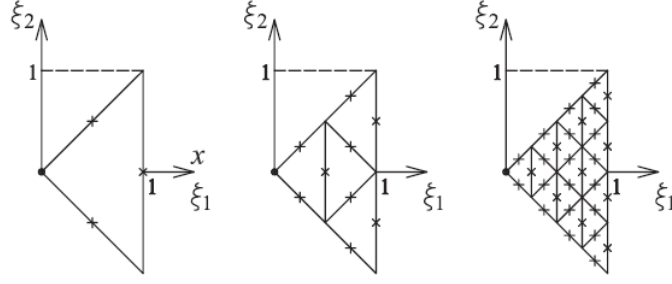Figure. B2. Position of the quadrature points (represented by the crosses) in the computational domain for levels 1, 2, and 3 (from left to right) defined as the number of divisions by 2 of the basic triangle of area 1

The level n corresponds to the division of the side of the basic triangle by $2n - 1$ resulting in $4n - 1$ sub-triangles of same area. In each triangle, the quadrature points are set at the mid sides. They are of equal weight corresponding to one third of the area of the sub-triangle. The weight is thus $\frac{1}{3} \times \frac{1}{4^{n-1}}$ or $\frac{2}{3} \times \frac{1}{4^{n-1}}$ if the quadrature point is shared by two sub-triangles. The position of the quadrature point in the physical domain is obtained by application of the mapping in (B1).

This mapping and quadrature should be sufficient for regular functions which is the case as long as the point load is not at one of the three nodes of the current triangle. If the point load is at one of the nodes, the function to integrate is singular there implying a risk of loss of accuracy. It is thus proposed to apply a Duffy's transformation. Consider the point load at node A as in Figure B3 and the first triangle defined with a level n Bartholomew refinement is now mapped to a square of side length of two. This mapping is expressed by the coordinate transformation

$$\eta_1 = 2^n \xi_1 - 1, \tag{B.6}$$

$$\xi_2 = \xi_1 \eta_2. \tag{B.7}$$

The Jacobian of the transformation is then $\frac{2^n}{\xi_1}$ so that the singular integrand in $\int r_\xi^{-1} d\xi_1 d\xi_2$ with $r_\xi^2 = \xi_1^2 + \xi_2^2$ is not singular after transformation in $\frac{1}{2^n} \int (1 + \eta_2^2)^{-1/2} d\eta_1 d\eta_2$, an integral over the square domain. A regular Gaussian quadrature is used in the two directions (3x3 Gauss points) to estimate such integrals.
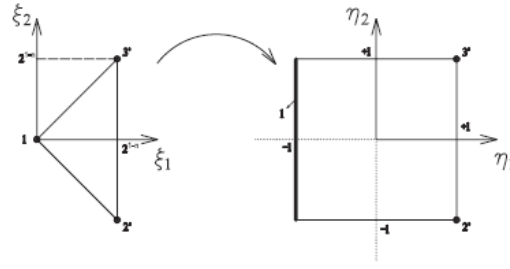
Figure. B3. The Duffy's transformation from the triangle touching the origin of the $(\xi 1, \xi 2)$ coordinates system (see Figure B2), where the point load is applied, to a square of side length two

To summarize: consider an integral over the triangle of area A over the physical domain of the type:

$$\int_{\Omega_t} \frac{f(\theta)}{r} dV, \tag{B.8}$$

using the polar coordinate around the point of application of the point load. This integral is transformed to the computational domain

$$\int_{\Omega_\xi} \frac{f(\theta)}{r} J dV_\xi, \tag{B.9}$$

defined by the transformation of Jacobian J and depicted in Figure B1. The numerical quadrature shown in Figure B2 applies for elements not connected to the application point of the point force. If the force is applied at node 1 of the triangle presented in this figure, the same quadrature is applied except for the first triangle (nodes 1, 2', and 3') presented in Figure B3. This triangle is transformed to a square Ω_η thanks to the Duffy's transformation (Figure B3) such that the contribution of the first triangle to the integral in equation (B.9) now reads

$$\int_{\Omega_\eta} \frac{f(\alpha)}{C_{\xi\xi}^{1/2}(1 + \eta_2^2)^{1/2}} \frac{J}{2^n} dV_\eta , \tag{B.10}$$

In which $C_{\xi\xi} = F_{ij}F_{ji}$.

Appendix C
Analytical solution for layered cylinder

The analytical solution for the layered cylinder problem proposed for validation of the numerical protocol in Section 4.3 is now presented. This solution is classically constructed via the displacement approach. The displacement is only radial because of the problem symmetry and corresponds to the unknown function $f(r)$. The volumetric strain is

$$\Theta = f'(r) + \frac{f(r)}{r},\tag{C.1}$$

The stress change components in the polar coordinates system are then in a generic form

$$\Delta\sigma_r(r) = \left(K(r) + \frac{4G(r)}{3}\right)f' + \left(K(r) - \frac{2G(r)}{3}\right)\frac{f}{r} - \alpha(r)\Delta p(r),\tag{C.2}$$

$$\Delta\sigma_\theta(r) = \left(K(r) + \frac{4G(r)}{3}\right)\frac{f}{r} + \left(K(r) - \frac{2G(r)}{3}\right)f' - \alpha(r)\Delta p(r),\tag{C.3}$$

the values of the material parameters and the fluid pressure change being constant over each subdomain:

$$r \le R: K(r) = K_{OR}\left(1 + \frac{3}{2}h_{KR}\Theta\right), G(r) = G_R, \alpha(r) = \alpha_R, \Delta p(r) = \Delta p_R ;\tag{C.4}$$

$$R \le r \le C: K(r) = K_C, G(r) = G_C, \alpha(r) = \alpha_C, \Delta p(r) = 0;\tag{C.5}$$

$$C \le r: K(r) = K_\infty, G(r) = G_\infty, \alpha(r) = \alpha_\infty, \Delta p(r) = 0.\tag{C.6}$$

The equilibrium equation reveals that the displacement field is of the type

$$f(r) = \frac{A_i}{2}r + \frac{B_i}{r},\tag{C.7}$$

with the subscript i standing either for the inner core (R) the cap rock (C) of the rest of the infinite space (∞). These six constants are found by ensuring displacement continuity and stress continuity at the contact between reservoir and caprock (r = R) and at the contact of the cap rock with the remaining space (r = C). Two additional conditions are that the displacement remains finite in the reservoir ($B_r = 0$) and decays in the outer region ($A_\infty = 0$). These six conditions are combined to obtain the following quadratic equation for A_R.

$$\frac{3}{2} K_{OR} \cdot h_{KR} \cdot A_R{}^2 + B \cdot A_R - \alpha_R \cdot \Delta p_R = 0, \tag{C.8}$$

with

$$B = K_{OR} + \frac{1}{3} G_R + G_C + a^2 \frac{\left(K_C + \frac{4}{3} G_C\right) \cdot (G_\infty - G_C)}{G_C \cdot \left(\frac{1}{3} + a^2\right) + K_C + G_\infty \cdot (1 - a^2)}, \text{ and } a = \frac{R}{C} \tag{C.9}$$

The remaining three unknown scalars are then found from

$$A_C = -a^2 \frac{(G_\infty - G_C)}{G_C \cdot \left(\frac{1}{3} + a^2\right) + K_C + G_\infty \cdot (1 - a^2)} A_R, \tag{C.10}$$

$$B_C = \frac{1}{2} (A_R - A_C) \cdot R^2, \tag{C.11}$$

$$B_C = \frac{1}{2} A_R \cdot R^2 + \frac{1}{2} A_C \cdot (C^2 - R^2) \tag{C.12}$$

A few remarks which will be helpful in the analysis of the application to 4D seismic in Section 4.4. The important variable is the volumetric strain introduced in equation (C.1) and which, for the general structure of the displacement function f in equation (C.7), is piecewise constant and equal to the scalar A_i. The volumetric strain in the reservoir is thus found from the solution of equation (C.8). It is partly driven by Biot coefficient and the fluid pressure change. More interesting is the volume change in the cap rock, A_C given by equations (C.10), (C.11) and (C.12). The volume change is zero if the cap rock and the infinite medium have the same shear modulus. If not, the volume change is proportional to the difference between these two moduli. This result points to the fact that a heterogeneous surrounding to the reservoir is conducive to volume change there. This is important since it is the volume change which is the selected parameter which controls the elasticity changes in this contribution.

Appendix D
Wave velocity changes for non-linear elasticity

The objective is to compute the changes in wave velocity for the non-linear material response introduced in Section 4.2.2.2 and used to study 4D effects during production in a reservoir found in a tilted block region, Section 4.4.

Consider a wave propagating in the direction n, of celerity c and with polarization vector p such that the displacement field is of the type $\underline{\tilde{u}} = \underline{p}\tilde{f}(\underline{x} \cdot \underline{n} - ct)$, for a generic function $\tilde{f}$. The superposed tilde is introduced to signal that the wave induces a small perturbation added to the displacement field generated during production. The linearized strain due to this perturbation is

$$\underline{\underline{\tilde{\epsilon}}} = \frac{1}{2} \cdot \left(\underline{p} \otimes \underline{n} + \underline{n} \otimes \underline{p} \right) \cdot \tilde{f}' \tag{D.1}$$

This perturbation in strain results in a perturbation in stress which is obtained as the second derivative of the energy defined in equation (4.7) and which reads

$$\underline{\underline{\tilde{\sigma}}} \equiv \frac{\partial^2 \varepsilon}{\partial \underline{\underline{\epsilon}} \partial \underline{\underline{\epsilon}}} : \underline{\underline{\tilde{\epsilon}}} = D^e : \underline{\underline{\tilde{\epsilon}}}, \tag{D.2}$$

with

$$D^e = 3 \cdot \left(K(\Theta) + 2 \cdot K_{,\Theta} \cdot \Theta \right) \cdot II + 2 \cdot G(\Theta) \cdot IK + 2 \cdot G_{,\Theta}$$
$$\cdot \left(\underline{\underline{\epsilon}}^{dev} \otimes \underline{\underline{\delta}} + \underline{\underline{\delta}} \otimes \underline{\underline{\epsilon}}^{dev} \right) \tag{D.3}$$

in which $\underline{\underline{\epsilon}}^{dev}$ is the deviatory strain (IK $:\epsilon$). The variation in fluid pressure has been ignored while taking that second derivative and it is assumed that the incompressibility in equation (D.2) is related to the undrained response without any change in the notation. This strong assumption will be discussed at the end of this section. Note also that second derivatives in the moduli $G(\Theta)$ and $K(\Theta)$ have been disregarded in equation (D.2).

The equation of motion for a homogeneous material of volumetric mass ρ with a linearized response described by equation (D.2) and a linearized strain as in equation (D.1) reads

$$\left[\underline{\underline{A}}(\underline{n}) - c^2 \cdot \rho \cdot \underline{\underline{\delta}} \right] \cdot \underline{p} = 0 \tag{D.4}$$

with

$$\underline{\underline{A}}(\underline{n}) \equiv \underline{n} \cdot D^e \cdot \underline{n} = \left(K(\Theta) + 2 \cdot K_{,\Theta} \cdot \Theta + \frac{G}{3}\right)\underline{n} \otimes \underline{n} + G(\Theta)\underline{\underline{\delta}} + 2 \cdot G_{,\Theta} \cdot (\underline{\Gamma} \otimes \underline{n} + \underline{n} \otimes \underline{\Gamma}),\quad \text{(D.5)}$$

and $\underline{\Gamma} = \underline{\underline{\epsilon}}^{dev} \cdot \underline{n}$,

in which $\underline{\underline{A}}(\underline{n})$ is the acoustic tensor. The eigenvalue of the acoustic tensor are the three possible values of $c^2 \cdot \rho$ and the associated eigenvector, the three polarization vectors.

This eigenvalue problem is conducted in the orthonormal basis $\{\underline{n}, \underline{n}_\perp, \underline{n}_\vdash\}$ so that the vector Γ in equation (D.5) has for decomposition

$$\underline{\Gamma} = \Gamma_n \cdot \underline{n} + \Gamma_\perp \cdot \underline{n}_\perp + \Gamma_\vdash \cdot \underline{n}_\vdash \tag{D.6}$$

The acoustic tensor has the following components in the same basis:

$$[A(\underline{n})] = \begin{bmatrix} \widetilde{K}_{oe} & 2 \cdot G_{,\Theta} \cdot \Gamma_\perp & 2 \cdot G_{,\Theta} \cdot \Gamma_\vdash \\ 2 \cdot G_{,\Theta} \cdot \Gamma_\perp & G & 0 \\ 2 \cdot G_{,\Theta} \cdot \Gamma_\vdash & 0 & G \end{bmatrix} \tag{D.7}$$

with

$$\widetilde{K}_{oe} = K(\Theta) + 2 \cdot K_{,\Theta} \cdot \Theta + \frac{4}{3} \cdot G(\Theta) + 4 \cdot G_{,\Theta} \cdot \Gamma_n, \tag{D.8}$$

in which $\widetilde{K}_{oe}$ is the oedometric incompressibility. The condition of a zero determinant for the eigenvalue problem in equation (D.5) has an obvious solution which is the eigenvalue $\lambda_{S1} = G(\Theta)$ which is linked to the first shear wave. The remaining condition is the following second-order equation

$$\lambda^2 - \lambda \cdot (\widetilde{K}_{oe} + G) + \left[\widetilde{K}_{oe} \cdot G - 4 \cdot G_{,\Theta}^2 \cdot \left(\Gamma_\perp{}^2 + \Gamma_\vdash{}^2\right)\right] = 0. \tag{D.9}$$

The discriminant with a first-order asymptotic development is

$$\Delta = (\widetilde{K}_{oe} - G)^2 \cdot (1 + 16 \cdot \varepsilon^2) \; with \; \varepsilon^2 = \frac{G_\Theta{}^2}{(\widetilde{K}_{oe} - G)^2} \cdot \left(\Gamma_\perp{}^2 + \Gamma_\vdash{}^2\right) \tag{D.10}$$

in which ε plays the role of the small parameter compared to one. The two roots of equation (D.9) are then readily computed, and the three eigenvalues are thus

$$\lambda_{S1} = G(\Theta), \qquad \lambda_{S2} = G(\Theta) \cdot \left(1 - 4 \cdot \frac{\widetilde{K}_{oe} - G}{G} \epsilon^2\right)$$

$$and \; \lambda_P = \widetilde{K}_{oe} \cdot \left(1 + 4 \cdot \frac{\widetilde{K}_{oe} - G}{\widetilde{K}_{oe}} \epsilon^2\right) \tag{D.11}$$

It is from these three values, disregarding the second-order terms, that the current wave velocities are now determined assuming the linear variations of the incompressibility and shear moduli defined in equation (4.10). The volumetric

strain also affects the material volumetric mass, and the conservation of mass provides the relation between the current ρ and the reference volumetric mass ρ_0.

$$\rho_0 = \rho \cdot (1 + \Theta) \tag{D.12}$$

consistent with our small perturbation assumption from the reference to the current configuration. The wave celerities are then deduced from equation (D.11) for the specific choices in equation (4.10) and with equation (D.12)

$$C_P = \sqrt{\frac{\widetilde{K}_{oe0}}{\rho_0}} \cdot \left[1 + \frac{1}{2} \cdot \left(1 + \frac{3 \cdot K_0 \cdot h_K + \frac{4}{3} \cdot G_0 \cdot h_G}{\widetilde{K}_{oe0}} \right) \Theta + \frac{2 \cdot G_0 \cdot h_G}{\widetilde{K}_{oe0}} \Gamma_n \right] \tag{D.13}$$

$$C_S = \sqrt{\frac{G_0}{\rho_0}} \cdot \left[1 + \frac{1}{2} \cdot (1 + h_G) \Theta \right] \tag{D.14}$$

keeping the first-order terms in either volumetric strain Θ or normal deviatory strain Γ_n and with $\widetilde{K}_{oe0}$ corresponding to the oedometric incompressibility in the reference configuration ($\Theta = 0$ in definition in equation D.7). The relative changes in wave celerities are then

$$\frac{\Delta C_P}{C_{P_0}} = \left(\frac{1}{2} + \frac{3 \cdot K_0 \cdot h_K}{\widetilde{K}_{oe0}} \right) \Theta + \frac{2 \cdot G_0}{\widetilde{K}_{oe0}} \underline{n} \cdot \underline{\underline{\epsilon}} \cdot \underline{n}, \tag{D.15}$$

$$\frac{\Delta C_P}{C_{P_0}} = \frac{1}{2} \cdot (1 + h_G) \cdot \Theta, \tag{D.16}$$

in which the modifications from equations (D.13) and (D.14) to equations (D.15) and (D.16) where done to replace the deviatory strain by the strain.

Four remarks to conclude. First, the structure of the acoustic tensor in equation (D.7) indicates that the P wave polarization vector has a small component normal to the propagation direction $\underline{n}$. Similarly, the two S waves which have a slight difference in celerity (second-order effects) propagate with a polarization vector having a small component in the propagation direction. Second, keeping the first-order effects only, the relative change in P wave celerity is anisotropic due to the term $\underline{n} \cdot \underline{\epsilon} \cdot \underline{n}$ in equations (D.15) and (D.16). The S-waves celerities are isotropic to first order. The third remark concerns the link between the relative velocity change and the strain obtained in equations (D.15) and (D.16). This relation is not linear between the relative velocity change and the strain component in the direction of propagation, as proposed with the R factor by (HATCHELL; BOURNE, 2005), but includes a contribution of the volumetric strain with the introduction of a R_Θ factor presented in equation (4.11) in the main text. Fourthly

and more importantly for the present study is the interpretation to be provided to the definition of the incompressibility and shear moduli considered in equation (D.11) and what follows. The non-linear elasticity response proposed in this contribution is meant for quasi-static processes whereas the propagating waves are probing the dynamic elasticity moduli of the rocks. The difference between static and dynamic elastic properties is not discussed here and the strong assumption is made that the ratio between static and dynamic elasticity moduli are the same under initial stress condition and at the current state of production. Consequently, the results based on equations (D.13) and (D.14) can indeed be used to infer the relative change in velocity found in equations (D.15) and (D.16).